

# International Journal of Manufacturing, Materials, and Mechanical Engineering

Volume 11 • Issue 3 • July-September 2021 • ISSN: 2156-1680 • eISSN: 2156-1672



**IGI PUBLISHING**  
AN IMPRINT OF IGI GLOBAL  
[WWW.IGI-GLOBAL.COM](http://WWW.IGI-GLOBAL.COM)

## EDITOR-IN-CHIEF

J. Paulo Davim, University of Aveiro, Portugal

## ASSOCIATE EDITORS

Dimitrios E. Manolakos, National Technical University of Athens, Greece  
Han Huang, The University of Queensland, Australia  
L. Norberto López de Lacalle, University of the Basque Country, Spain  
Leonid Burstein, ORT Braude Engineering college (retired), Israel  
Liangchi Zhang, University of New South Wales, Australia  
Mark J. Jackson, Purdue University, USA  
Patricio Franco, Technical University of Cartagena, Spain  
Uday Shanker Dixit, Indian Institute of Technology Guwahati, India  
Viktor P. Astakhov, Michigan State University, USA

## EDITORIAL REVIEW BOARD

Aitzol Lamikiz, University of the Basque Country, Spain  
Alfonso H.W. Ngan, University of Hong Kong, Hong Kong  
Altino Loureiro, University of Coimbra, Portugal  
Ana-Eva Jiménez-Ballesta, Technical University of Cartagena, Spain  
Angelos P. Markopoulos, National Technical University of Athens, Greece  
António Completo, University of Aveiro, Portugal  
Bekir S. Yilbas, King Fahd University of Petroleum and Minerals, Saudi Arabia  
Fabrizio Quadrini, University of Rome Tor Vergata, Italy  
Filipe Teixeira-Dias, University of Aveiro, Portugal  
Fusaomi Nagata, Tokyo University of Science, Japan  
Inderdeep Singh, Indian Institute of Technology Roorke, India  
Jack G. Zhou, Drexel University, USA  
Jamal Ahmad, Khalifa University of Science and Technology, UAE  
Jing Shi, University of Cincinnati, USA  
Jingwei Zhao, University of Wollongong, Australia  
Jiwang Yan, Keio University, Japan  
Jorge Ferreira, University of Aveiro, Portugal  
José Maria Cirne, University of Coimbra, Portugal  
Juan C. Campos Rubio, Federal University of Minas Gerais, Brazil  
Kapil Gupta, University of Johannesburg, South Africa  
Kayaroganam Palanikumar, Sri Sairam Institute of Technology, India  
Kevin Chou, University of Alabama, USA  
Leonardo R. da Silva, Federal Center for Technological Education, Brazil  
Lidia Gurau, Transilvania University of Brasov, Romania  
Loredana Santo, University of Rome Tor Vergata, Italy  
Maki K. Habib, The American University in Cairo, Egypt  
Manish Roy, Defence Metallurgical Research Laboratory, India  
Meng Ni, The Hong Kong Polytechnic University, China  
Murali M. Sundaram, University of Cincinnati, USA  
Nikolaos M. Vaxevanidis, School of Pedagogical and Technological Education (ASPETE), Greece  
Nourredine Boubekry, University of North Texas, USA  
Paulo A.F. Martins, University of Lisbon, Portugal  
Prasanta Sahoo, Jadavpur University, India  
R. Venkata Rao, Sardar Vallabhbhai National Institute of Technology (SV NIT), India  
Ramon Quiza, University of Matanzas, Cuba  
Robert A. Fontes Valente, University of Aveiro, Portugal  
Rui A.S. Moreira, University of Aveiro, Portugal  
S. Basavarajappa, University B.D.T. College of Engineering, India

**EDITORIAL REVIEW BOARD***CONTINUED*

S.K. Shukla, Banaras Hindu University, India  
S.R. Karnik, B.V. Bhoomaraddi College of Engineering and Technology, India  
Sergiu-Dan Stan, Technical University of Cluj-Napoca, Romania  
Shuting Lei, Kansas State University, USA  
Teresa M.G.P. Duarte, University of Porto, Portugal  
Vinayak Neelakanth Gaitonde, B.V. Bhoomaraddi College of Engineering and Technology, India  
Vishal S. Sharma, Dr. B.R. Ambedkar National Institute of Technology, India  
Xiaohong Tina Zhang, Seagate Technology LLC, USA  
Xipeng Xu, Huaqiao University, China  
Yajie Lei, George Washington University, USA  
Zhengyi Jiang, University of Wollongong, Australia

# Call for Articles

## International Journal of Manufacturing, Materials, and Mechanical Engineering

Volume 11 • Issue 3 • July-September 2021 • ISSN: 2156-1680 • eISSN: 2156-1672

### MISSION

The mission of the **International Journal of Manufacturing, Materials, and Mechanical Engineering (IJMMME)** is to provide a channel of communication to disseminate knowledge between academics/researchers and industry practitioners. This journal can serve as a useful reference for academics, manufacturing, materials, mechanical, industrial, systems, environmental and physics engineers, materials and manufacturing researches, professionals in mechanical engineering and related industries.

### COVERAGE AND MAJOR TOPICS

**The topics of interest in this journal include, but are not limited to:**

Aerodynamics and fluid mechanics • Artificial intelligence applied, optimization methods • Automation and control • Bioengineering materials, biomechanics and biotribology • Bulk deformation processes and sheet metal forming • Composites, ceramics, polymers / processing • Computational mechanics / FEM modelling and simulation • Computer-based manufacturing technologies: CNC, CAD, CAM, FMS, CIM • Design and manufacture, medical device manufacturing • Friction and wear of materials, corrosion resistance • Functionality graded materials, cellular materials • Heat treatments, microstructure and materials properties • Hydrostatic transmissions and pneumatic • Instrumentation and measurement • Joining and fracture mechanics • Kinematics and dynamics of rigid bodies • Lubricants and lubrication • Machinability and formability of materials • Machining (traditional and non-traditional processes) • Manufacturing design for 3r “reduce, reuse, recycling” • Mechanisms and machines • Mechatronics and robotics • Metallic alloys and metal casting • Micro and nanomechanics • Multifunctional and smart materials • Nanomaterials and nanomanufacturing • Rapid manufacturing technologies and prototyping, remanufacturing • Recycling, materials and industrial wastes, products and recycling systems • Renewable energies technology • Solid mechanics and structural mechanics • Sustainable and green manufacturing • Thermodynamics and heat transfer • Tribology and surface engineering • Vibration and acoustics • Wood and wood products

**ALL INQUIRIES REGARDING IJMMME SHOULD BE DIRECTED TO THE ATTENTION OF:**

J. Paulo Davim, Editor-in-Chief • [IJMMME@igi-global.com](mailto:IJMMME@igi-global.com)

**ALL MANUSCRIPT SUBMISSIONS TO IJMMME SHOULD BE SENT THROUGH THE ONLINE SUBMISSION SYSTEM:**

<http://www.igi-global.com/authors/editors/titlesubmission/newproject.aspx>

**IDEAS FOR SPECIAL THEME ISSUES MAY BE SUBMITTED TO THE EDITOR(S)-IN-CHIEF**

**PLEASE RECOMMEND THIS PUBLICATION TO YOUR LIBRARIAN**

For a convenient easy-to-use library recommendation form, please visit:

<http://www.igi-global.com/IJMMME>

# Table of Contents

## International Journal of Manufacturing, Materials, and Mechanical Engineering

Volume 11 • Issue 3 • July-September-2021 • ISSN: 2156-1680 • eISSN: 2156-1672

### Research Articles

- 1 **Strength Optimization of Infant Pop-Up Seat Frame Using Discrete Material and Thickness Optimization**  
YeongJo Ju, Kongju National University, South Korea  
Euyseok Jeon, Kongju National University, South Korea
- 21 **Battery Management for Small Hydroponic Systems and Cultivation Experiments**  
Satoru Yamaguchi, Kanagawa Institute of Technology, Japan  
Takuya Motosugi, Kanagawa Institute of Technology, Japan  
Yoshihiko Takahashi, Kanagawa Institute of Technology, Japan
- 37 **Dynamic Analysis and Simulation of the Hydraulic Control System on the Remote-Controlled Explosive Ordnance Disposal Machine**  
Dat Duy Nguyen, Le Quy Don Technical University, Vietnam  
Dat Van Chu, Le Quy Don Technical University, Vietnam  
Le Van Sy, Petrovietnam University, Vietnam
- 55 **Classification and Automatic Feature-Based Extraction Approach for Cylindrical and Milling Parts**  
Sathish Kumar Adapa, Aditya Institute of Technology and Management, India  
Dowluru Sreeramulu, Aditya Institute of Technology and Management, India  
Jagadish, National Institute of Technology, Raipur, India
- 74 **Turning SKD 11 Steel Using Silver Nanofluids With Minimum Quantity Lubrication**  
M. Naresh Babu, Easwari Engineering College, Chennai, India  
V. Anandan, Saveetha Engineering College, Chennai, India  
M. Dinesh Babu, Panimalar Engineering College, Chennai, India  
N. Muthukrishnan, Sri Venkateswara College of Engineering, India

### COPYRIGHT

The International Journal of Manufacturing, Materials, and Mechanical Engineering (IJMMME) (ISSN 2156-1680; eISSN 2156-1672). Copyright © 2021 IGI Global. All rights, including translation into other languages reserved by the publisher. No part of this journal may be reproduced or used in any form or by any means without written permission from the publisher, except for noncommercial, educational use including classroom teaching purposes. Product or company names used in this journal are for identification purposes only. Inclusion of the names of the products or companies does not indicate a claim of ownership by IGI Global of the trademark or registered trademark. The views expressed in this journal are those of the authors but not necessarily of IGI Global.

The *International Journal of Manufacturing, Materials, and Mechanical Engineering* is indexed or listed in the following: ACM Digital Library; Bacon's Media Directory; Cabell's Directories; DBLP; Google Scholar; INSPEC; JournalTOCs; MediaFinder; ProQuest Engineering Journals; ProQuest Illustrata: Technology; ProQuest Materials Science Journals; ProQuest SciTech Journals; ProQuest Technology Journals; SCOPUS; The Standard Periodical Directory; UGC-CARE List (India); Ulrich's Periodicals Directory; Web of Science; Web of Science Emerging Sources Citation Index (ESCI)

# Strength Optimization of Infant Pop-Up Seat Frame Using Discrete Material and Thickness Optimization

YeongJo Ju, Kongju National University, South Korea

 <https://orcid.org/0000-0002-6606-4889>

Euysik Jeon, Kongju National University, South Korea

## ABSTRACT

In this paper, the authors proposed an optimal design method for the strength design of infant pop-up seat frame combined with rear seats for infants, children, and adults, not removable booster seats or car seats. Frame strength design was performed using discrete material and thickness optimization (DMTO) method considering high strength steel (HSS) and advanced high strength steel (AHSS). Structural design using the Section 4 link mechanism was performed, and the weakness of the seat frame due to static load was confirmed through finite element analysis. An optimal design criterion was established by carrying out a case study to derive the limiting conditions according to static and dynamic loads. In consideration of these criteria, the optimal design according to d-optimal and discrete Latin-hypercube (DLH) was performed among the design of experiments (DOE). And the strength of the pop-up seat frame for infants according to each DOE was checked, and the strength optimization method was suggested by comparing the lightweight ratio.

## KEYWORDS

Discrete Material and Thickness Optimization, Finite Element Analysis (FEA), Infant, Pop-Up Seat, Strength Optimization

## 1. INTRODUCTION

Technologies applied to automobiles have grown proportionally to the advances in the automobile industry, and they have become universal and popular with the development of the industry. Accordingly, the consumption of vehicles has steadily increased, and various vehicle models have been developed to meet the demands of various consumers. The variety of vehicle models has developed into multi-purpose recreation vehicles that have the benefits of each vehicle model as related studies have actively been conducted. Multi-purpose recreation vehicles put emphasis on convenience and safety, and include various types of seats that can variably change the interior space. Most of the people who purchased mention the availability of the large interior space as a selection criterion, and there are containment seats among foldable rear seats for space utilization (Baltas, & Saridakis, 2013).

Among the containment seats, there is an infant pop-up seat, which is applied to the rear seats in the 2nd and 3rd rows, and it has the same function as the booster seat. The booster seat was applied in accordance with the regulations related to child boarding. According to the regulations of the National Highway Traffic Safety Administration (NHTSA) in the United States, children aged between 2 and

DOI: 10.4018/IJMMME.2021070101

Copyright © 2021, IGI Global. Copying or distributing in print or electronic forms without written permission of IGI Global is prohibited.

12 years are required to be seated on booster seats when they get on vehicles. Therefore, booster seats are essential elements in the rear seats of vehicles (Lee et al., 2019). Booster seats, which are seats for children, serve to correct the seating positions of children aboard in rear seats.

Thus, booster seats must be used. Infant pop-up seats combined with rear seats, which have the same function as booster seats that can prevent the injuries of infants or children, have already been applied to some vehicles (Asbridge et al., 2018). Unlike booster seats, infant pop-up seats can be used by both children and adults when their shapes are changed, but a design method that can satisfy the seat frame evaluation strength is required. In addition, there is a need for a way to reduce the weight of the seat frame while satisfying the strength of the seat frame.

In a study on optimizing the seat frame or seat component to which the optimization method was applied, Kim et al. (2014) and Kim et al. (2016) applied high-strength steel (HSS), which has higher strength than general steel, to compare the stiffness according to the thickness of the seat frame. Jeon et al. (2017) and Ju et al. (2017) proposed an optimization method by performing optimization according to the shape, material, and thickness of the seat frame and headrest module using design of experiments (D.O.E). Song et al. (2017) and Shin et al. (2018) proposed a method for the optimization of the structure combined with the seat cushion and cushion frame using an optimization technique for strength improvement and weight reduction. In addition to the seat frame, studies have been conducted to optimize the structure of the structure. Yang et al. (2016) and Oh et al. (2017) and Na et al. (2017) proposed a design method by performing topology optimization or size optimization to reduce the weight of the parts associated with the vehicle. In addition, Ju et al. (2019), in order to suggest a design method that can improve the strength of the vehicle seat frame, it has been confirmed that the strength is improved and the weight reduction is possible by using the structural analysis and optimization method applying dissimilar materials.

Studies on booster seats, car seat design guidelines, and rear seat belt wearing were conducted to secure the safety of infants by analyzing the injuries of infants according to the seat belt (Jingwen, 2016). Studies on the strength and optimal design of seats, however, are not sufficient. A study was conducted to quantify the difference in posture and belt wearing across a range of booster designs that provide different boosting levels (Jones, 2020), using booster seats when infants are seated in a rear row seat. Although seated, infants may be injured due to slip by external shock (Oana et al., 2017). There is a pop-up type infant pop-up seat in the rear row seat by replacing the booster seat, but only research on the mechanism of the pop-up seat frame was conducted (Jakobsson et al., 2007). Therefore, studies to confirm or improve the strength of the leg portion of the frame due to external impact are insufficient, and further studies on strength design according to the structure of the infant pop-up seat are required.

In this paper, we propose an optimization method through finite element analysis for the strength optimization of infant pop-up seat frame. By performing finite element analysis according to the evaluation method for checking the strength of the seat frame, the weakness of the seat frame was derived when applying the static and quasi-static loads of the infant pop-up seat frame. And a case study and two experimental design methods were presented to optimize the strength of the infant pop-up seat frame.

## **2. CONFIGURATION OF INFANT PUP-UP SEAT**

### **2.1 Infant Pop-Up Seat Frame**

Infant pop-up seats serve to correct the seating positions of children aboard in the rear seats of a vehicle. When children get on vehicles, adults hold them or they are seated in regular seats in many cases. If accidents occur in such cases, children are subjected to a higher impact than adults (Bohman et al., 2011).

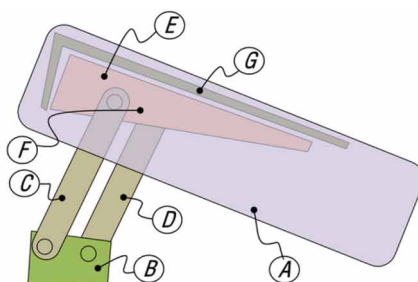
In this paper, an attempt was made to strength design of the infant pop-up seat frame, which can reduce injuries by firmly supporting the body of children even if they wear adult seat belts by adjusting their seating positions. The infant pop-up seat frame can be mainly divided into the leg part combined with the rear seat frame and the cushion part. The mechanism of the pop-up seat includes a mechanism that allows children to be seated at a higher position than the seating position of adults and allows adults to be seated at the conventional seating position. The leg part of the pop-up seat is combined with the seat frame and located in front of the cushion. The containment and withdrawal of the cushion part is possible using the link mechanism. As for the link mechanism applied to the infant pop-up seat, a 4-link mechanism was applied so that the behavior of the cushion part could be predicted in a stable manner. The combination of the 4-bar linkage and the cushion part allows children to be stably seated. Figure 1 and Table 1 show the components of the infant pop-up seat, which are located in front of the seat cushion.

## 2.2 Pop-Up Seat Geometry and Infant Dummy

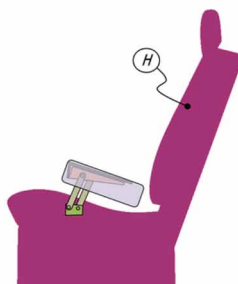
As the first step for the structural stability and optimal design of the infant pop-up seat, it is necessary to set the geometry of the pop-up seat module and seat belt. Based on the height of booster seats and the position of the seat belt mounting part in previous studies (Reed et al., 2009, 2005), the geometry of the infant pop-up seat and seat belt was set as shown in Figure 2 and Table 2.

According to the geometry setting of the infant pop-up seat, the top of the cushion of the infant pop-up seat is 85mm higher than that of the seat cushion of the rear seat. As for the structure of the pop-up seat module, the pop-up seat cushion part is contained when an infant is not seated and withdrawn when an infant is seated. An infant can be seated after the withdrawal of the pop-up seat, and an adult can be seated after its containment. The containment and withdrawal of the pop-up seat are based on the structure that includes a 4-bar linkage, and the structure is operated by the rotation of the link around the lower drive part.

Figure 1. Infant pop-up seat concept



(a) Concept of infant pop-up seat module



(b) Concept of infant pop-up seat module and rear seat

**Table 1. The folding seat part**

Symbol	Part name
A	Cushion
B	Leg hinge
C	Leg main link
D	Leg sub link
E	Cushion base frame
F	Cushion upper frame hinge
G	Cushion upper frame
H	Rear seat

To perform the dynamic optimization of the infant pop-up seat by applying its dynamic environment, the geometry of the seat belt was set according to the geometry setting of the pop-up seat. As for the position of the seat belt, the positions of the upper belt point and lower belt points were set in accordance with the three-point seat belt anchor regulations of ECE R14 and FMVSS 210 (Youn et al., 2015). The position of the three-point seat belt based on the regulations considered children aged 12 years or above, adults, and elderly people. It may be necessary to analyze the injuries of infants according to the seat belt position, the seat belt position based on the typical regulations was utilized in this study because examining the injuries of infants according to the seat belt position is not the purpose of this study (Youn et al., 2015).

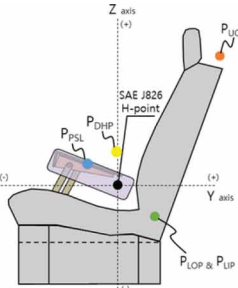
After setting the geometry of the seat belt, Hybrid III 6 Year Old Child, a 6-year-old dummy mainly researched as a sitting target, was applied based on the previous studies on the injuries of infants seated on rear seats. In this paper, Hybrid III 6 Year Old Child, a 6-year-old dummy finite element model, was applied. Considering the sitting posture of adults, the posture of the infant was set as shown in Table 3 (Wu et al., 2012). The geometry of the infant pop-up seat was considered so that the raised hip point (H-point) could be in contact with the top of the cushion part.

After modeling the pop-up seat module structure, rear seat modeling was performed to apply the pop-up seat. For rear seat modeling, FEA was conducted considering static and dynamic environments. As FEA was applied as a means to combine the pop-up seat module in the two environments, the rear seat was modeled with simplified geometry. For seat modeling, the seatback and the cushion part were combined, and modeling was performed so that the infant pop-up seat module could be mounted on the front part of the seat cushion. In addition, a sled jig model that can move the rear seat model was combined with the seat model to conduct the frontal-impact sled test required for FEA in dynamic environment.

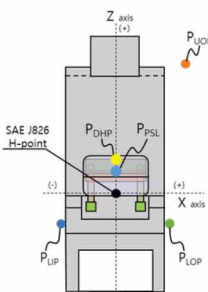
### **3. STRUCTURAL ANALYSIS OF INFANT POP-UP SEAT**

#### **3.1 Finite Element Analysis of Infant Pop-Up Seat Frame**

The components of the seat including the infant pop-up seat module, and the simplified modeling. In the pop-up seat module, the leg hinge is combined with the front part of the rear seat cushion, and an infant is seated on the cushion upper frame. The cushion upper frame was assumed to be a simplified plate-type model rather than a pad type. As for the modeling of the rear seat for the application of the pop-up seat module, FEA that considered static and dynamic environments was applied. As FEA was applied as a means to combine the pop-up seat module in the two environments, the rear seat

**Figure 2. Geometry of seat belt position**

(a) Side view



(b) Iso view

**Table 2. Position dimensions of Infant pop-up seat and seat belt points**

Symbol	Part name	Dimension		
		X position [mm]	Y position [mm]	Z position [mm]
$P_{PSL}$	Pop-up Seat cushion Location	0	-120	85
$P_{UOP}$	Upper seat belt Outboard point	254	411	581
$P_{LOP}$	Lower seat belt Outboard point	191	120	-140
$P_{LIP}$	Lower seat belt Inboard point	-191	120	-140

was modeled with simplified geometry. In the seat model, the seatback and the cushion part were combined, and the infant pop-up seat module could be mounted on the front part of the seat cushion.

For the structural and optimal design of the infant pop-up seat module, the model excluding the pop-up seat module was constructed using 2D elements larger than 10 mm in seat modeling. In addition, no deformation was assumed by applying the rigid body condition. The infant pop-up seat was constructed with 5mm 2D elements as it was necessary to set and change its design variables, and the thicknesses and material properties of the leg hinge and main parts were applied. Table 4 shows the components of the pop-up seat and rear seat finite element model.

As for the thickness applied to the pop-up seat module, a 1.5mm thickness was applied to the leg hinge, leg main link, and cushion hinge considering the thickness that can be achieved during the

**Table 3. Hybrid III 6 Year Old Child Dummy Positioning**

<b>Symbol</b>	<b>Part name</b>	<b>Dimension</b>			
		<b>X position [mm]</b>	<b>Y position [mm]</b>	<b>Z position [mm]</b>	<b>Angle (X axis) [°]</b>
$P_{DHP}$	Dummy h-point	0	0	125	-
$\theta_{Thor}$	Angle of thorax	-	-	-	23
$\theta_{Thi}$	Angle of thigh	-	-	-	19
$\theta_{Arms}$	Angle of arms	-	-	-	35

**Table 4. Finite elements model of infant pop-up seat module**

<b>Part name</b>	<b>Dimension</b>	<b>Type</b>	<b>Size [mm]</b>	<b>Elements numbers [ea]</b>
Infant pop-up seat module	2D shell	Triangle	5	1,562

manufacture of parts. In the case of the cushion upper frame, a plate type was applied rather than a solid type and a 1.5mm thickness was applied. The material properties of steel, which was applied to seat frames, were applied. An attempt was made to identify the weakness of the pop-up seat module through the analysis that applied the material properties.

Basic structural analysis was conducted using the seat model that included the infant pop-up seat module. In the structural analysis, static analysis according to the static load was conducted using LS-DYNA under the assumption that a vertical load and a torsional load were applied to an infant seated.

A load higher than the vertical weight of the infant and a torsional load higher than the reference load were applied to identify the weakness of the infant pop-up seat module (Ju, & Jeon, 2019). To identify the weakness of the infant pop-up seat module to the vertical load (bending load), the pelvis of Hybrid III 6 Year Old Child was extracted and assumed as a rigid body without deformation, and it was assumed that the pelvis was seated on the cushion upper frame of the pop-up seat module. The application of the entire model of an infant may involve errors, and the pelvis was assumed as a rigid body to shorten the time. The contact condition was applied to the pelvis defined as a rigid body and the cushion upper frame of the pop-up seat so that the load of the pop-up seat module could be transmitted. Setting for static analysis was performed by applying the material properties and boundary conditions shown in Table 5 and Table 6.

To identify the weakness of the infant pop-up seat module to the bending load, the rear seat was fixed and the bending load was applied as shown in Figure 3 (a). In addition, the rear seat was fixed and the torsional load was applied to the upper side of the cushion upper frame of the pop-up seat as shown in Figure 3 (b) to identify the weakness of the pop-up seat module to torsion. Although there are no determined standards for bending and torsional load conditions, the load conditions were applied by referring to the cases of previous studies (Ju et al., 2019). The contact condition was applied to the pelvis defined as a rigid body and the cushion upper frame of the pop-up seat so that the load of the pop-up seat module could be transmitted according to the application of the bending and torsional loads.

In the results of the analysis that applied bending and torsional load conditions to the infant pop-up seat module. As shown in Figure 4 and Figure 5, Parts vulnerable to the loads were derived by examining the deformation of the leg hinge and cushion frame, except for the cushion upper frame

**Table 5. Material properties of steel**

Category	Unit	Description
Materials	-	Steel
Young's Modulus	GPa	210
Poisson's Ratio	-	0.3
Density	kg/mm <sup>3</sup>	7.85×10 <sup>6</sup>
Yield Strength	MPa	208

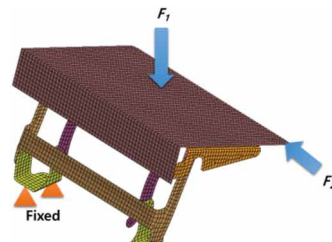
**Table 6. Material properties and boundary conditions applied for static analysis**

Symbol	Description	Properties	
		Thicknesses [mm]	Materials [-]
B	Leg hinge	1.5	Steel
C	Leg main link	1.5	Steel
D	Leg sub link	1.5	Steel
E	Cushion base frame	1.5	Steel
F	Cushion hinge	1.5	Steel
G	Cushion upper frame	1.5	Steel
H	Rear seat	-	-
I	Pelvis	-	-

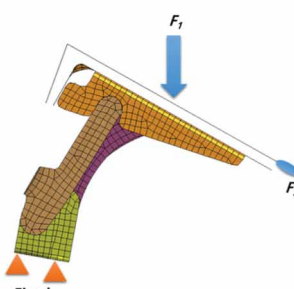
on which a 6-year-old infant was seated. As shown in Table 7, the cushion base frame of the pop-up seat exhibited the displacement of 6.102 mm due to the bending load. The analysis results according to the torsional load showed that the displacement of 26.75 mm occurred in the cushion upper frame hinge as shown in Table 7.

Under the bending load, the cushion base frame of the pop-up seat exhibited the largest deformation. When the cushion upper frame and cushion base frame were excluded, however, the leg sub link exhibited the deformation of 3.512 mm, confirming that the left leg sub link is a vulnerable part. Under the torsional load, the cushion base frame showed the largest deformation. When the cushion upper frame and cushion base frame were excluded, however, the cushion upper frame hinge exhibited the displacement of 2.011 mm, confirming that it is a vulnerable part. In the case of the torsional load, it was inevitable that the hinges were subjected to the largest deformation due to the torsional load, but the leg main link exhibited small deformation.

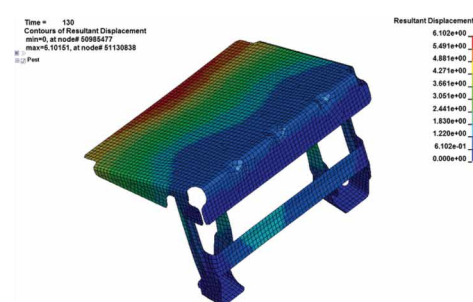
As the purpose of this paper is the optimal design of the infant pop-up seat module, the model excluding the pop-up seat module was constructed using 2D elements larger than 10 mm in seat modeling. In addition, no deformation was assumed by applying the rigid body condition. The infant pop-up seat was constructed with 5mm 2D elements as it was necessary to set and modify its design variables, and the thicknesses and material properties of the leg hinge and main parts were applied. Table 8 shows the configuration of the pop-up seat and rear seat finite element model. The modeling of infant sitting for testing in dynamic environment. The boundary conditions of FEA in dynamic environment were applied as shown in Figure 6.

**International Journal of Manufacturing, Materials, and Mechanical Engineering**  
Volume 11 • Issue 3 • July-September 2021**Figure 3. Boundary conditions applied with bending and torsional loads**

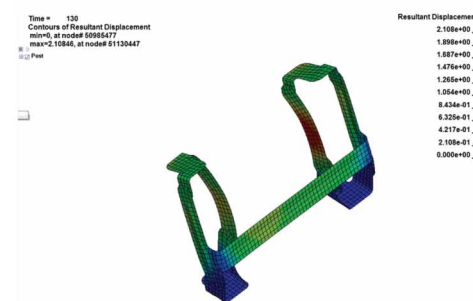
(a) Side view



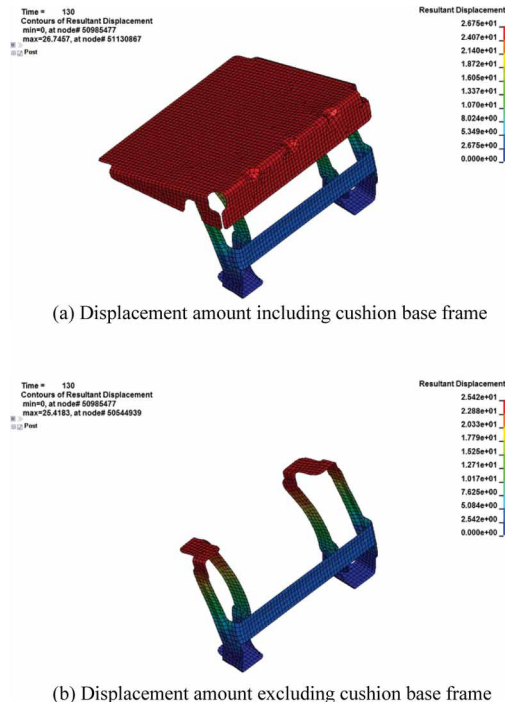
(b) Iso view

**Figure 4. Analysis results of bending load**

(a) Displacement amount including cushion base frame



(b) Displacement amount excluding cushion base frame

**Figure 5. Analysis results of torsional load****Table 7. Results of structural analysis**

Description	Maximum displacement according to bending load [mm]	Maximum displacement according to torsional load [mm]	Weight [kg]
Values	6.102	26.75	1.875

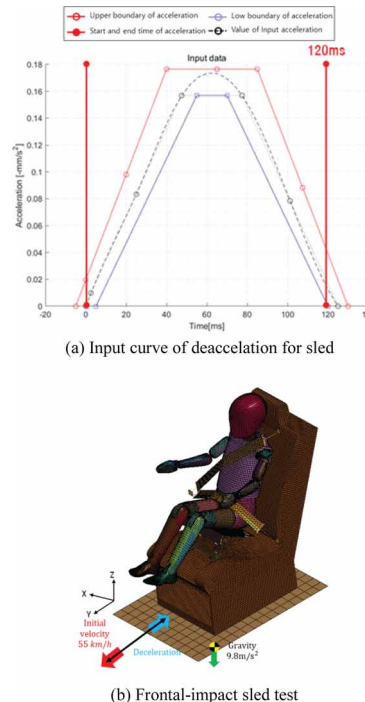
**Table 8. Modeling of Infant pop-up seat module and seat**

Part name	Dimension	Type	Size [mm]	Number [ea]
Pop-up seat model	2D shell	Triangle	5	25,161
Rear seat	2D shell	Square	10	5,260
Sled test plate	2D shell	Square	10	238

### 3.2 Setting the Ranges of Design Parameters Using Case Study

Based on the basic static analysis of the infant pop-up seat module, a case study was conducted to set optimization design parameters. The items to be applied to the case study are the material and thickness applied to the pop-up seat module. The applied material and thickness were changed to select the parts of the pop-up seat module that requires optimization according to the material and thickness. The materials to be applied are HSS and AHSS, which have higher strength than steel and enable weight reduction through the reduced thickness. HSS with higher strength than steel has been applied to some lightweight seat frames. The application of HSS can reduce the weight of the

**Figure 6. Boundary conditions of dynamic analysis**



module while satisfying the typical seat frame strength standards. AHSS has higher strength than HSS and can further reduce the weight of structures. Due to its high cost compared to HSS, it has been applied only to some parts for ensuring safety. For example, it has been applied to impact bars or side members that prevent the side impact inside a car door, but this is also not easy due to problems with processing. An attempt was made in this study to find methods to apply HSS or AHSS, which have higher strength than conventional steel, to secure the safety of the infant pop-up seat and to reduce its weight.

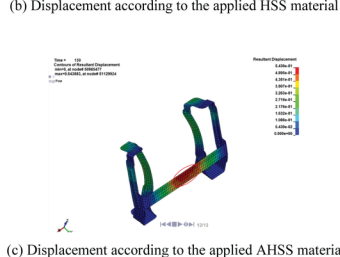
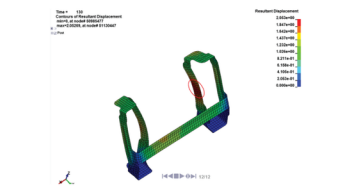
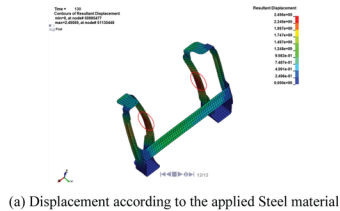
Table 9 shows the parts of the infant pop-up seat and their applied thicknesses. The thicknesses applied to the parts were 1.0, 1.5, and 2.0 mm, which were defined as levels 1, 2, and 3. The materials applied were steel, HSS, and AHSS, which were defined as levels 1, 2, and 3.

A total of nine cases to conduct analysis were designed through a combination of the thickness and material properties to be applied to each part of the infant pop-up seat module. Nine case studies were conducted to examine the deformation of the pop-up seat module and its weight reduction tendency according to the material and thickness.

Figures 7, 8, and 9 show the results of static and dynamic analyzes performed using infant pop-up seat. Figure 7 shows the deformation with bending load when steel, HSS and AHSS are applied. Figure 8 shows the deformation under torsional load when steel, HSS and AHSS are applied. Figure 9 shows the deformation under dynamic load, which is a sled test when steel, HSS and AHSS are applied. According to a case study, the displacement of the infant pop-up seat module is as follows, rather than applying the typical steel material and thickness to the infant pop-up seat module. Through the application of HSS and AHSS and thickness change, it was confirmed that the strength was improved up to 59% at the bending load, and it was confirmed that the strength was improved up to 39.8% at the torsional load. In addition, it was confirmed that the strength was improved up to 13.7% in dynamic load.

**Table 9. Part thickness for case study**

Symbol	Range of thickness [mm]			Explanation
	Low	Mean	High	
$t_B$	1.0	1.5	2.0	Leg hinge thickness
$t_C$				Leg main link thickness
$t_D$				Leg sub link thickness
$t_E$				Cushion base frame thickness
$t_F$				Cushion hinge thickness
$t_G$				Cushion upper frame thickness

**Figure 7. Analysis result according to bending load in case study**

### 3.3 Setting the Ranges of Design Parameters

Based on the maximum result derived through the case studies under bending load, the result of the analysis conducted by applying steel (level 1 for the material) and 1.5 mm (level 2 for the thickness) was selected as the strength criterion for bending load. In this case, the maximum displacement was 6.16 mm. As for the torsional load analysis, the result of the analysis conducted by applying steel (level 1 for the material) and 1.5 mm (level 2 for the thickness), which led to the average result, was selected as the strength criterion for torsional load. In this case, the maximum displacement was 72.95 mm. In the analysis that applied the sled test, the result of the analysis conducted by applying steel (level 1 for the material) and 1.5 mm (level 2 for the thickness), which derived the average result, was selected as the strength criterion for torsional load. In this case, the maximum displacement was 120

**International Journal of Manufacturing, Materials, and Mechanical Engineering**  
 Volume 11 • Issue 3 • July-September 2021

**Figure 8. Analysis results according to torsional load in case study**

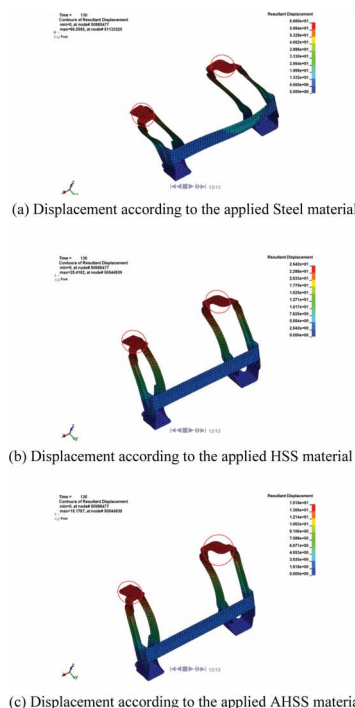
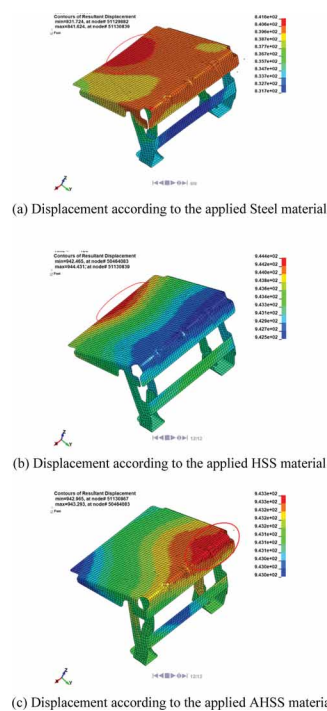


**Figure 9. Analysis result according to sled test in case study**



mm. The maximum displacements under bending, torsional, and dynamic loads derived according to the strength criteria were set as constraints.

## 4. STATIC AND DYNAMIC OPTIMIZATION OF INFANT POP-UP SEAT FRAME

### 4.1 Optimization Problem Using D-Optimal

The formulation of the optimal design problem using D-Optimal is performed as follows. Table 10 shows the levels according to the applied material and thickness for optimization. Equation (1) represents the thickness parameter for each part of the infant pop-up seat module, and equation (2) the material parameter for each part. In the D-Optimal optimization process, steel, HSS, and AHSS were applied to the parts. As shown in equation (3), the mass ( $m$ ), the maximum displacement under bending load ( $\delta_B$ ), the maximum displacement under torsional load ( $\delta_T$ ), and the maximum displacement in the sled test ( $\delta_S$ ) were derived through the static and dynamic analysis results.

**Table 10. Level of design variable**

Symbol	Level 1	Level 2	Level 3
Thickness	1.0 [mm]	1.5 [mm]	2.0 [mm]
Materials	Steel	HSS	AHSS

Minimizing the mass ( $\min(m)$ ), the sum of the thickness levels ( $\min\left(\sum_{i=1}^i X\right)$ ), and the sum of the material levels ( $\min\left(\sum_{j=1}^j Y\right)$ ) was set as the object function as shown in equation (4). The constraints for the bending load, torsional load, and sled test were 11.57, 41.82, and 100 mm, respectively, as shown in equations (5), (6), and (7).

Parameters:

$$X = \{x_i\} \quad (i = 1, 2, \dots, 6) \quad (1)$$

$$Y = \{y_j\} \quad (j = 1, 2, \dots, 6) \quad (2)$$

Response:

$$f(X, Y) = [m, \delta_B, \delta_T, \delta_S] \quad (3)$$

Minimize object function:

$$\min \left( m, \sum_{i=1}^i X, \sum_{j=1}^j Y \right) \quad (4)$$

Constraints:

$$\delta_B < \delta_{B,C} \quad (5)$$

$$\delta_T < \delta_{T,C} \quad (6)$$

$$\delta_s < \delta_{s,C} \quad (7)$$

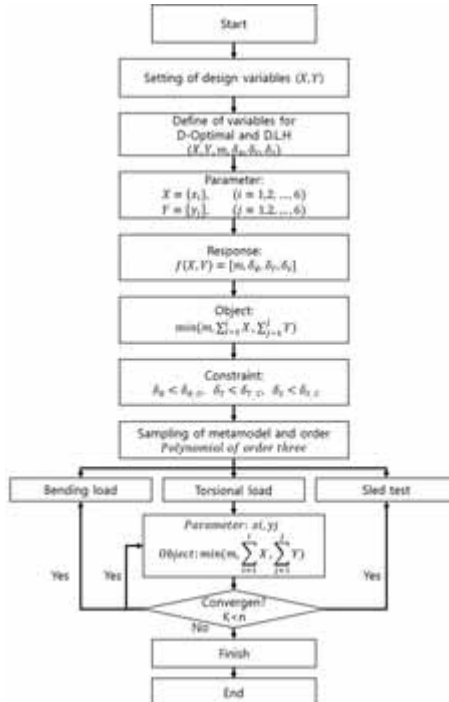
where:

- $X$  : Set of the thickness parameters of each part
- $Y$  : Set of the material parameters of each part
- $\sum_{i=1}^i X$  : Sum of the thickness levels of each part
- $\sum_{j=1}^j Y$  : Sum of the material levels of each part
- $m$  : Mass of the infant seat frame [kg]
- $\delta_B$  : Maximum displacement under bending load [mm]
- $\delta_{B,C}$  : Constraint of the maximum displacement under bending load [mm]
- $\delta_T$  : Maximum displacement under torsional load [mm]
- $\delta_{T,C}$  : Constraint of the maximum displacement under torsional load [mm]
- $\delta_s$  : Maximum displacement in the sled test [mm]
- $\delta_{s,C}$  : Constraint of the maximum displacement in the sled test [mm]

The optimization process is shown in Figure 10. Bending, torsional, and dynamic loads were applied. As for the design parameters, both the thickness and material were set to level 3.

The discretization variables and  $x_i$  of  $y_i$  of each part were determined by D-Optimal DOE. For each result, the reaction surface (meta-model) was generated using a polynomial, and optimization according to the parameter change was performed using a GA. The values predicted through the response surface were compared with the analysis results.

The results of the static and dynamic optimization of the seat model, including the infant pop-up seat module, using D-Optimal. Relative deformation and weight according to the bending load, torsional load, and sled test were examined. The relative deformation under each load was obtained by converting the difference in deformation between the rigid body and the infant pop-up seat module. Through the relative deformation, the influence of the thickness and material applied to the parts of the pop-up seat subjected to optimization can be examined. The strength compare ratio according to each load can be examined using the strength compared to the infant pop-up seat module that

**Figure 10.** Optimization process using D-Optimal and DLH

used conventional steel as shown in Table 11. The optimization results confirmed that the relative deformation has a larger influence on the applied material than on the thickness for the parts of the pop-up seat module. It was confirmed that the deformation deviation was in the range of 3.3% to 40.7% at the bending load and 1% to 28.4% at the torsional load. In addition, it was confirmed that it was in the range of 8% ~ 13.7% in sled load.

Based on the results of the static and dynamic optimization of the infant pop-up seat module using D-Optimal, the interaction and correlation between the thickness and material were analyzed. It was confirmed that the thickness and material applied to the infant pop-up seat module were different according to the bending load, torsional load and sled test (dynamic load). Table 11 shows the minimum and maximum optimization results considering the results according to three loads among the results of creating 20 models using the D-Optimal design method. From the optimization results, the displacement decreased according to the three loads, and at the same time, the common thickness and material level that the weight can bear was derived for each part. As a result, it was confirmed that the thickness and material of the part can be improved by 3.3% to 33.1% in strength compared to the infant pop-up seat module applying the typical thickness and material while satisfying -6% light weight than the typical weight.

#### 4.2 Optimization Problem Using DLH

Among DOEs, the formulation of the optimal design problem using DLH is the same as D-Optimal. The process of optimization using DLH is shown in Figure 10. Bending, torsional, and dynamic loads were applied. As for the design parameters, both the thickness and material were set to level 3. The discretization variables  $x_i$  of  $y_i$  of each part were determined by the Latin-Hypercube DOE. For each result, the reaction surface (meta-model) was generated using a polynomial, and optimization

**Table 11. Results of analysis table to D-Optimal**

Descriptions		B	C	D	E	F	G	Strength compare ratio [%]	Weight [kg]
Init.	$x_i$ [Level]	2	2	2	2	2	2	-	1.875
	$y_i$ [Level]	1	1	1	1	1	1		
Optimal min	$x_i$ [Level]	3	3	3	1	1	2	-3.3	1.699
	$y_i$ [Level]	3	3	1	3	1	3		
Optimal max	$x_i$ [Level]	1	1	3	3	1	1	-33.1	1.766
	$y_i$ [Level]	1	3	2	1	1	3		

according to the parameter change was performed using a GA. The values predicted through the response surface were compared with the analysis results.

The results of the static and dynamic optimization using DLH, among DOEs. Relative deformation and weight according to the bending load, torsional load, and sled test were examined. The relative deformation under each load was obtained by converting the difference in deformation between the rigid body and the infant pop-up seat module. The strength compare ratio according to each load can be examined using the strength compared to the infant pop-up seat module that used conventional steel as shown in Table 12. The optimization results confirmed that the relative deformation has a larger influence on the applied material than on the thickness for the parts of the pop-up seat module. It was confirmed that the deformation deviation was in the range of 3.3% to 45.9% at the bending load and 1% to 34.0% at the torsional load. In addition, it was confirmed that it was in the range of 8% ~ 13.8% in sled load.

Based on the results of the static and dynamic optimization of the infant pop-up seat module using DLH, the interaction and correlation between the thickness and material were analyzed. It was confirmed that the thickness and material applied to the infant pop-up seat module were different according to the bending load, torsional load and sled test (dynamic load). Table 12 shows the minimum and maximum optimization results considering the results according to three loads among the results of creating 20 models using the D-Optimal design method. From the optimization results, the displacement decreased according to the three loads, and at the same time, the common thickness and material level that the weight can bear was derived for each part. As a result, it was confirmed that the thickness and material of the part can be improved by 3.3% to 36.6% in strength compared to the infant pop-up seat module applying the typical thickness and material while satisfying -15% light weight than the typical weight.

#### 4.3 Results of D-Optimal and DLH

Table 13 shows the results of optimization using D-Optimal and DLH, respectively. In both optimization methods, displacement was reduced by up to 33% or more and showed similar strength performance. The optimization result of applying D-optimal confirmed that the thickness and material value applied for each part can improve the strength at level 1 and level 3. From the optimization result applying DLH, it was confirmed that the value of the applied thickness for each part can be

**Table 12. Results of analysis table to DLH**

Descriptions		B	C	D	E	F	G	Strength compare ratio [%]	Weight [kg]
Init.	$x_i$ [Level]	2	2	2	2	2	2	-	1.875
	$y_i$ [Level]	1	1	1	1	1	1		
Optimal min	$x_i$ [Level]	3	3	3	1	1	2	-3.3	1.699
	$y_i$ [Level]	3	3	1	3	1	3		
Optimal max	$x_i$ [Level]	2	1	1	1	3	1	-36.6	1.586
	$y_i$ [Level]	3	3	3	3	1	1		

applied to level 1 and level 2. And it was confirmed that the value of the material can improve the strength at level 1 and level 3. When comparing the optimization methods, it was confirmed that less deformation occurs even when the DLH is thinner than D-Optimal, even when a low-level thickness is applied. So the application of DLH is expected to be more advantageous in terms of strength. On the contrary, it was confirmed that the material applied under the same setting conditions showed less deformation even when a material with a lower strength level than that of DLH in D-optimal was applied. Therefore, the application of D-optimal is expected to be more advantageous in terms of material application.

**Table 13. Comparison of the D-Optimal and DLH results**

Descriptions		B	C	D	E	F	G	Strength compare ratio [%]	Weight [kg]
Init.	$x_i$ [Level]	2	2	2	2	2	2	-	1.875
	$y_i$ [Level]	1	1	1	1	1	1		
D-Optimal	$x_i$ [Level]	1	1	3	3	1	1	-33.1	1.766
	$y_i$ [Level]	1	3	2	1	1	3		
DLH	$x_i$ [Level]	2	1	1	1	3	1	-36.6	1.586
	$y_i$ [Level]	3	3	3	3	1	1		

## 5. CONCLUSION

This paper attempted to propose an infant pop-up seat frame strength design method according to the optimization method. Among the optimization methods, finite elements analysis using D-Optimal and DLH was performed to present and compare the strength design method according to the thickness and material to be applied. First, the concept design of the infant pop-up seat module and the geometry were constructed using the seat belt and child dummy. In order to create a finite element model of the pop-up seat module and identify weaknesses, performed a finite element analysis that applied the static evaluation method of the seat frame. As a result, it was confirmed that the legs combined with the seat frame were weak, and displacement according to bending and torsional load was confirmed. And for the optimization criteria and parameter setting, the parameter range was set by performing a case study according to the thickness and material set at three levels. Optimal design for strength design of static and dynamic analysis was performed using the optimal design method of D-Optimal and DLH. Through formulating the problem of optimal design, the applied thickness and material were set as parameters at 3 levels, and the strength was checked by checking the displacement of the pop-up seat according to the object function and constraint. As a result of optimization using D-Optimal, it was confirmed that the strength improved from 13.7% to 40.7% depending on bending, torsional, and sled load. In the optimization result using DLH, it was confirmed that the strength can be improved from 13.8% to 45.9% depending on bending, torsional, and sled load. In addition, it was confirmed that the strength can be improved by more than 33% by determining the common thickness and material level that can be applied when considering the three loads. In conclusion, using the optimization method applying D-Optimal and DLH, we confirmed the design method that can light weight together with the strength design of the infant pop-up seat. It is expected that this design method can be applied to the optimal design of the rear seat frame.

## ACKNOWLEDGMENT

This paper was supported by the Human Resource Training Program(S2755803) for business-related research and development of Ministry of SMEs and Startups in 2019.

## REFERENCES

- Asbridge, M., Ogilvie, R., Wilson, M., & Hayden, J. (2018). The impact of booster seat use on child injury and mortality: Systematic review and meta-analysis of observational studies of booster seat effectiveness. *Accident; Analysis and Prevention*, 119, 50–57. doi:10.1016/j.aap.2018.07.004 PMID:29990613
- Baltas, G., & Saridakis, C. (2013). An empirical investigation of the impact of behavioural and psychographic consumer characteristics on car preferences: An integrated model of car type choice. *Transportation Research Part A, Policy and Practice*, 54, 92–110. doi:10.1016/j.tra.2013.07.007
- Bohman, K., Stockman, I., Jakobsson, L., Osvalder, A. L., Bostrom, O., & Arbogast, K. B. (2011, October). Kinematics and shoulder belt position of child rear seat passengers during vehicle maneuvers. In *Annals of Advances in Automotive Medicine/Annual Scientific Conference* (Vol. 55, p. 15). Association for the Advancement of Automotive Medicine.
- Jakobsson, L., Wiberg, H., Isaksson-Hellman, I., & Gustafsson, J. (2007, June). Rear seat safety for the Growing Child—a new 2-stage integrated booster cushion. *Proc of 20th Int. ESV Conf.*
- Jeon, D., & Jeon, E. S. (2017). Lightweight Optimization of Headrest Modules Including Flat-Plate Sliding Brackets. *International Journal of Applied Engineering Research: IJAER*, 12(8), 1719–1724.
- Jingwen, H. U. (2016). Rear Seat Occupant Protection: What Do We Know and What is the Future? *Journal of Automotive Safety and Energy*, 7(04), 339.
- Jones, M. L., Ebert, S., Manary, M. A., Reed, M. P., & Klinich, K. D. (2020). Child posture and belt fit in a range of booster configurations. *International Journal of Environmental Research and Public Health*, 17(3), 810. doi:10.3390/ijerph17030810 PMID:32012975
- Ju, Y. J., & Jeon, E. S. (2017). Lightweight Optimization of Joint Type Seatback including Plastic Materials. *International Journal of Applied Engineering Research: IJAER*, 12(15), 5173–5180.
- Ju, Y. J., & Jeon, E. S. (2019). Topology Optimization of Seat Cushion Frame With Dissimilar Materials for Lightweight Strength Optimization. *International Journal of Manufacturing, Materials, and Mechanical Engineering*, 9(1), 1–12. doi:10.4018/IJMME.2019010101
- Kim, H. S., Lee, Y. S., Yang, S. M., & Kang, H. Y. (2016). Structural analysis on variable characteristics of automotive seat frame by FEA. *International Journal of Precision Engineering and Manufacturing-Green Technology*, 3(1), 75–79. doi:10.1007/s40684-016-0010-x
- Kim, K. S., Cho, H. S., Kim, Y. C., & Cho, J. U. (2014). Structural Study of Automotive Seat Frame with High Tension Steel Plate Using Analysis and Experiment. *Journal of the Korea Academia-Industrial Cooperation Society*, 15(1), 27–31.
- Lee, G., Pope, C. N., Nwosu, A., McKenzie, L. B., & Zhu, M. (2019). Child passenger fatality: Child restraint system usage and contributing factors among the youngest passengers from 2011 to 2015. *Journal of Safety Research*, 70, 33–38. doi:10.1016/j.jsr.2019.04.001 PMID:31848007
- Na, S. J., & Jeon, E. S. (2017). Lightweight Corrugated Plate for Cargo box by using DOE and Topology Optimization. *International Journal of Applied Engineering Research: IJAER*, 12(22), 12564–12569.
- Oana, O., Nicolae, D., & Ilie, D. (2017, October). Dynamic models to analyse the influence of the seat belt in a frontal collision. *IOP Conference Series. Materials Science and Engineering*, 252(1), 012017. doi:10.1088/1757-899X/252/1/012017
- Oh, H. T., & Jeon, E. S. (2017). Lightweight Optimal Design of Tailgate Lift Link under Eccentric Loading. *International Journal of Applied Engineering Research: IJAER*, 12(17), 6627–6632.
- Reed, M. P., Ebert, S. M., Sherwood, C. P., Klinich, K. D., & Manary, M. A. (2009). Evaluation of the static belt fit provided by belt-positioning booster seats. *Accident; Analysis and Prevention*, 41(3), 598–607. doi:10.1016/j.aap.2009.02.009 PMID:19393812
- Reed, M. P., Ebert-Hamilton, S. M., Manary, M. A., Klinich, K. D., & Schneider, L. W. (2005). A new database of child anthropometry and seated posture for automotive safety applications. *SAE Transactions*, 2222–2235. doi:10.4271/2005-01-1837

**International Journal of Manufacturing, Materials, and Mechanical Engineering**

Volume 11 • Issue 3 • July-September 2021

Shin, D. S., Song, Y. J., & Jeon, E. S. (2018). Lightweight design of seat cushion extension modules using the properties of plastic and HCA-SIMP. *International Journal of Mechanical Engineering and Technology*, 9(5), 624–632.

Song, Y. J., & Jeon, E. S. (2017). Optimal Design of Lightweight Seat Extension Equipment Using Topology Optimization and Design of Experiment. *International Journal of Applied Engineering Research: IJAER*, 12(9), 1855–1859.

Wu, J., Hu, J., Reed, M. P., Klinich, K. D., & Cao, L. (2012). Development and validation of a parametric child anthropomorphic test device model representing 6–12-year-old children. *International Journal of Crashworthiness*, 17(6), 606–620.

Yang, Y. S., & Jeon, E. S. (2016). Tailgate Hinge Stiffness Design using Topology Optimization. *International Journal of Applied Engineering Research: IJAER*, 11(19), 9776–9781.

Youn, Y., Kim, H., Park, J., Lee, J., & Kim, S. (2015). Investigation of rear seat occupant potential injury risk base on seat belt configurations. In *24th International Technical Conference on the Enhanced Safety of Vehicles (ESV) National Highway Traffic Safety Administration* (No. 15-0443). Academic Press.

Youn, Y., Park, J., Lee, S., & Kim, M. (2015). A study of rear seat belts geometric characteristics for rear seated occupants protections. *Journal of Auto-vehicle Safety Association*, 7(1), 45–50.

*Yeongjo Ju received his MS from the Graduate School of Mechanical Engineering of Kongju National University, in 2017. His research interests include process structural design and engineering.*

*Euysik Jeon received his MS and PhD from the School of Precision Mechanical Engineering of Hanyang University, in 1987 and 1995, respectively. He is currently a professor in the Department of Future Convergence Engineering, Kongju National University. His research interests include process optimization techniques, structural design, and engineering.*

# Battery Management for Small Hydroponic Systems and Cultivation Experiments

Satoru Yamaguchi, Kanagawa Institute of Technology, Japan

Takuya Motosugi, Kanagawa Institute of Technology, Japan

Yoshihiko Takahashi, Kanagawa Institute of Technology, Japan

## ABSTRACT

A small hydroponic system that can use sustainable energy such as solar power has been developed. However, the amount of power generated is not constant, and in the case of unstable weather, enough power cannot be obtained. Therefore, it is necessary to store the generated energy in a battery. In order to design low-cost charging equipment, it is necessary to use a smaller battery and to estimate the remaining charge capacity (state of charge: SOC) accurately. To provide an accurate SOC estimation for such systems, a fusion of CI (current integral) and OCV (open circuit voltage) methods is proposed. When using this method, it is necessary to frequently disconnect the electronic load. In these experiments, the optimum disconnection duration, the effects on plants of frequent battery disconnection, and cutting off of the lighting were investigated.

## KEYWORDS

Battery Capacity Management, Cultivation Experiments, Current Integral Method, Frequent Battery Disconnection, Hydroponic Cultivation, Open Circuit Voltage Method, Remaining Capacity Estimation, SOC

## 1. INTRODUCTION

### 1.1 Research Background and Examples of Plant Cultivation Systems Using Sustainable Energy

Shortly, the food crisis due to worldwide population growth and rising food prices is anticipated, and people will have to become more self-sufficient. Besides, the agricultural working population in Japan is dropping sharply and mostly consists of elderly people. Climate change also poses a threat to the cultivation of crops. A hydroponic system allows the effective use of sustainable energy, making it possible to grow plants without being significantly affected by the natural environment. Large hydroponic systems called plant factories have been developed in the past (Holz, et. al., 2015; Zhang, et. al., 2018; Kozai, 2013). Relatively small hydroponic systems for farmers have also been developed (George, et. al., 2017; Yoshiga, et. al., 2016; Palande, et. al., 2018). In any case, hydroponic systems are likely to be operated using sustainable energy in the future (Fathabadi, et. al., 2017; Rekioua, et. al., 2014; Yunez-Cano, et. al., 2016). Compact, low-cost, tabletop hydroponic systems have been developed to grow vegetables inside or outside homes (Yamaguchi, et. al., 2018). Self-sufficient energy systems that use sustainable energy sources such as solar power have also been designed.

In recent years, solar sharing, where plants are grown under solar panels, has also attracted attention (Sekiyama, et. al., 2019). Agrivoltaics (the combination of using land for agricultural and electric energy production via photovoltaics) is attracting worldwide interest as a solution to the recent

DOI: 10.4018/IJMMME.2021070102

Copyright © 2021, IGI Global. Copying or distributing in print or electronic forms without written permission of IGI Global is prohibited.

increase in energy and food demand (Sekiyama, et. al., 2019; Nozu, 2018; Kamada, 2019). The first solar sharing system was proposed (Goetzberger, et. al., 1982), and various types of Agrivoltaic systems have been studied (Prannay, et. al., 2017; Othman, et. al., 2018). Photovoltaic power generation is also attracting attention as alternative energy that replaces fossil fuels (Scognamiglio, 2016; Dupraz, et. al., 2011; Dinesh, et. al., 2016).

From these studies, it is expected that the demand for plant cultivation systems that can utilize sustainable energy will increase regardless of scale. Systems that combine sustainable energy sources such as wind and solar power are expected.

## **1.2 Need for Battery Management in Small Plant Cultivation Systems**

When using sustainable energy, it is necessary to store energy because the amount of generated power is not constant and the energy is needed even at night or in bad weather. To keep costs low, the storage battery must be compact. For this reason, hydroponic systems, incorporate weather prediction, are being studied (Uchiyama, et. al., 2019). Research is also being conducted into battery management to improve the use and effectiveness of batteries in hydroponic systems (Motosugi, et. al., 2019). Research into leaf lettuce cultivation using hydroponics, and the effects of factors such as irradiation intensity from, and duration of exposure to LED lighting, is being conducted (Yamaguchi, et al., 2019).

When managing a secondary battery such as a lead-acid battery, accurate measurement of the charge/discharge and the remaining capacity (state of charge: SOC) is crucial. If the remaining capacity is accurately estimated, a cost-effective battery system can be designed. There are several techniques for estimating the SOC of a battery: the current integration (CI) method, the open-circuit voltage (OCV) method, and the close circuit voltage (CCV) method (Xing, et al., 2014). There are also methods which utilize statistical information and Kalman filters (Snihir, et al., 2006). Since plant cultivation can be lengthy, there have been problems with the conventional estimation methods.

## **2. THE PROPOSED METHOD FOR ESTIMATING REMAINING BATTERY CAPACITY FOR PLANT CULTIVATION SYSTEMS**

A new estimating method named the CI-OCV method, a combination of CI and OCV methods, was designed to be the optimal system for plant cultivation systems (Motosugi, et. al., 2019). The CI-OCV method uses the following procedure to estimate the remaining capacity:

1. The remaining capacity is estimated by the CI method for a certain period (approximately one hour) during which there is almost no accumulative measurement error in the current sensor.
2. After that, the circuit is cut off (that is, the LED illumination is turned off). The remaining capacity is estimated by the OCV method after a certain period. In these experiments, the period was about 5 minutes.
3. Repeat this process.

The proposed CI-OCV method can be used without problems during a long-term plant cultivation period (in these tests one month).

## **3. CONTENTS OF THIS PAPER**

However, in the proposed CI-OCV method, the LED lighting circuit has to be cut off when estimating the remaining capacity, as in the OCV method. The cut-off time of the circuit should be long enough to achieve accurate voltage readings, but not so long as to negatively affect plant growth. Therefore, the relationship between circuit break time and SOC measurement accuracy must be investigated, as well as the effect on plant growth. These are considered in this paper.

## 4. ESTIMATION METHODS OF REMAINING CHARGE CAPACITY FOR HYDROPONIC SYSTEMS

In battery management, estimating the remaining capacity is of major importance. Therefore, in this chapter, a proposed battery management system for hydroponics is investigated. First, the battery parameters of the secondary battery while discharging is explained. Also, the remaining capacity estimation methods that have been used so far are explained, and then an improved method is proposed.

### 4.1 Discharge Characteristics and Parameters Used in Secondary Batteries

Fig. 1 shows the discharge characteristics of a nickel-metal hydride secondary battery: the horizontal axis is time, the vertical axis is voltage, the left side of the graph is the discharge state where the electric load is connected, and the right side is the open-circuit state where the electric load is cut off. From the figure, it can be seen that the voltage phenomenon is different when the load is connected and when it is cut off.

When an electrical load is connected to the battery, the voltage drops rapidly, and this voltage is called the close circuit voltage (CCV). On the other hand, when the electrical load is interrupted, the voltage increases until it reaches a constant value, and this voltage is called the open-circuit voltage (OCV).

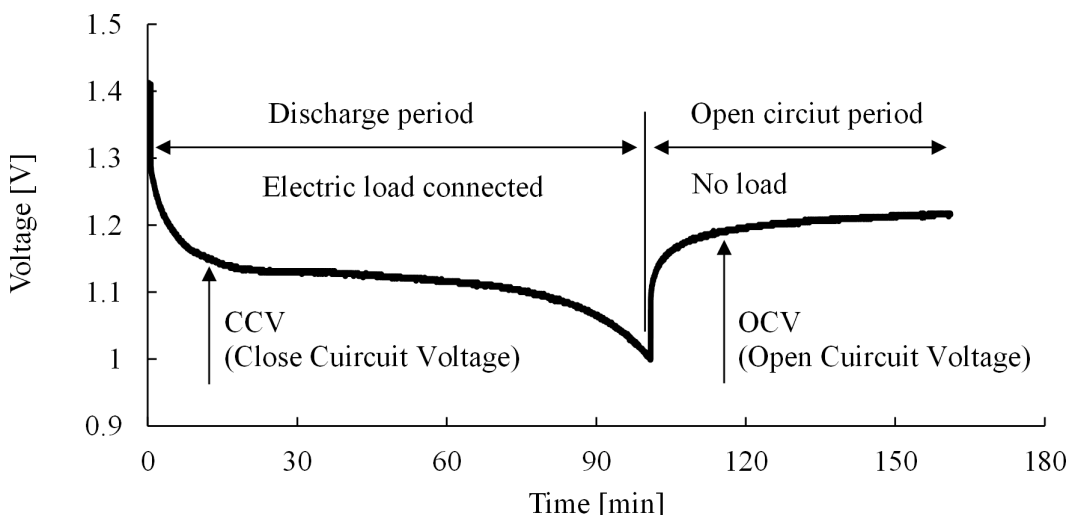
The state of charge (SOC) indicates the remaining capacity of the battery. For example, SOC 100% indicates that the battery is fully charged.

## 5. ESTIMATION METHODS OF REMAINING CHARGE CAPACITY (SOC)

To gauge SOC, the open-circuit voltage (OCV) method, the close circuit voltage (CCV) method, and the current integration (CI) method are generally used. We are proposing a new CI-OCV method which combines the CI and OCV methods. The following is an explanation of these conventional methods and an explanation of a newly proposed method:

- OCV method:** The OCV method estimates the SOC from the relationship between SOC and OCV readings. The SOC-OCV relationship is fairly clear, and involves easy measurements, and

Figure 1. Explanation of battery characteristics



provides accurate results. However, the electric load must be cut off, and a certain time interval is required for the measured voltage to reach a stable state.

- **CCV method:** The CCV method estimates the SOC from the relationship between SOC and CCV readings as in the case of the OCV method. Compared with the OCV method, the terminal voltage of the battery can be measured immediately without disconnection from an electric load. However, this estimation method has the disadvantage that the terminal voltage changes depending on the magnitude of the electric load, and certain conditions are required for accurate voltage measurements. The history of the discharge current and the history of the environment temperature are the two main variables that affect voltage readings. It is a great merit that the remaining capacity can be estimated immediately without disconnecting the electronic load. However, since the measured value changes intricately depending on the battery usage status, the estimation method is complicated.
- **CI method:** The CI method estimates the SOC by integrating the discharge and charge current. Since the CI method measures the current at a chosen time-frequency, the SOC estimation can be instantly calculated. However, since the error of the current sensor is also integrated, there is the drawback that an error occurs in the estimation of the SOC when the experiments are performed over a long period without allowing for the error. This is a very accurate estimation method when the accumulated error can be canceled in a relatively short time, such as in automobile battery management (because most car journeys are short). On the other hand, plant cultivation takes a long time, for example, about one month, so the accumulation of sensor errors is a big problem.
- **CI-OCV method:** This is a proposed collaboration method for plant cultivation systems that successfully combines the advantages of the CI and OCV methods. The outline of the algorithm is as follows. SOC values are obtained by following the sequence, one-hour of lighting/5 minutes cut off/one-hour of lighting/5 minutes cut off, and so on. The correct SOC value is obtained and error calibration is performed. This operation is repeated. Accurate SOC values can be obtained even after one month of use. However, similar to the OCV method, the battery will be disconnected (for example, once every hour during cultivation). Therefore, it is necessary to investigate the effects of the cut off on plant cultivation.

## **6. EXPERIMENTS INTO THE RELATIONSHIP BETWEEN SOC AND TIME INTERVAL REQUIRED FOR SOC ESTIMATION**

First, the full charge capacity (FCC) value of the battery, which is the reference value when calculating the SOC value, was measured. In the OCV method, the voltage does not stabilize at a constant value until some time has elapsed after the electronic load is disconnected. Since our method also combines the OCV method, it is necessary to investigate how long it takes for the voltage to stabilize. In this chapter, the time interval until a stable and constant OCV value is obtained will be investigated. After that, the relationship between OCV and SOC values was investigated using the measured FCC value.

### **6.1 Experiments on FCC Measurements**

Figure 2 shows the experimental setup and flow for the measurement of the FCC value. In the experiments, a lead-acid battery was used and connected to a stabilized DC power supply when charging, and to an electronic load device when discharging. The current sensor was connected in series between the lead-acid battery and the stabilized DC power supply (or electronic load). Battery terminal voltage was measured directly from the battery terminals. Temperature sensors were installed on the side of the battery case and inside the thermostat chamber. The current sensor and the temperature sensor were supplied with power from an external power source. The data logger measured the battery terminal voltage, the battery current, the temperature in the thermostat chamber, and the temperature of the side of the battery case.

The following equipment and parts were used:

- >Lead-acid batteries (5AH, 20h): WP5-12, LONG
- >Data logger: GL240, GRAPHTEC
- >Temperature sensor: LM35DZ, Texas Instruments
- >DC current sensor: HPS-05-AS, UR-D
- >Power supply for current sensor: LX035-1A, Takasago
- >Stabilized DC power supply: PWR800L, Kikusui
- >Electric load: FK-2, Takasago
- >Thermostat chamber: SIB-35, Mitsusho

The following experimental conditions were used:

- >Temperature inside thermostat chamber: 25°C
- >Number of trials: 3
- >Sampling time: one second

The experimental procedure is shown below (see also Fig.2 (b)). Repeat the following four steps (1 to 4) three times:

1. Charge with terminal voltage 14.50V, current limit 1A, Constant Current (CC) charge using the DC stabilized power supply.
2. When the display of the stabilized power supply changes to Constant Voltage (CV), charge for 1 hour at a terminal voltage of 13.50V and 0.5A. This is called float charging.
3. Leave for 1 hour after float charging.
4. Discharge to CCV: 10.50V at 0.250Ah (1/20C) using an electronic load device.

Figure 3 shows the results. Here, Figure 3(a) is the discharge phenomenon (CCV). At the start of the measurements, it showed around 12.5V, and after about 900 minutes, showed 10.50V which is the final voltage after discharge. Fig. 3(b) shows the integrated value of discharge current, and the final value is the FCC value. As for the FCC value, the first reading was 3.75Ah, the second 3.68Ah, the third 3.75Ah, and the average value was 3.73Ah. Based on these experiments, the FCC value was set to 3.73Ah (20hour rate) and this setting was defined as SOC100%. Figure 3(c) shows the temperatures inside the thermostat chamber and on the side of the battery case. The temperature in the thermostat chamber was kept between 26-27 °C. The temperature of the side of the battery case did not increase during battery discharge.

## 6.2 Experiments on OCV Measurements

The OCV values of the lead-acid battery were measured, and the SOC-OCV characteristics were investigated. The setup configuration was the same as the FCC measurement experiments.

The following conditions were used:

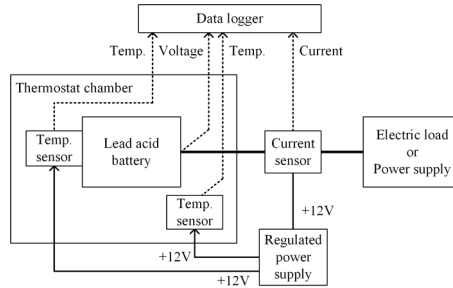
- >Temperature inside the thermostat chamber: 25°C
- >Number of trials: 1
- >Sampling period: 1 second

The procedure is shown below (see also Fig. 4). The following steps (1 to 3) were repeated:

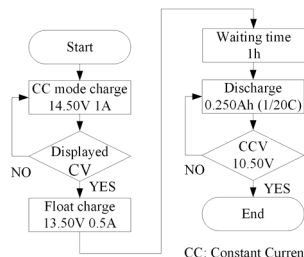
1. The battery was discharged at 0.250A (1/20C) using the Constant Current (CC) mode of the electronic load.

**International Journal of Manufacturing, Materials, and Mechanical Engineering**  
 Volume 11 • Issue 3 • July-September 2021

**Figure 2. Experimental set up and flow of FCC measurements**

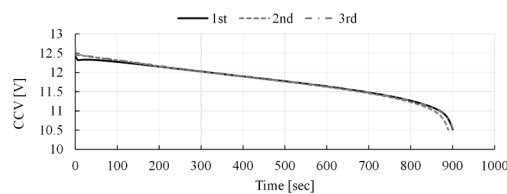


(a) Block diagram of experimental set up

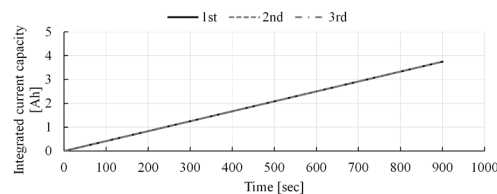


(b) Flow diagram

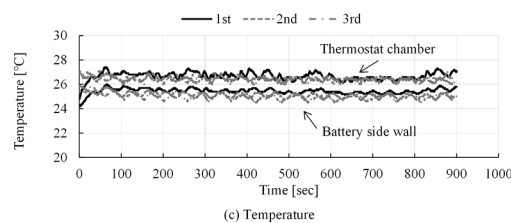
**Figure 3. Experimental results of FCC measurements**



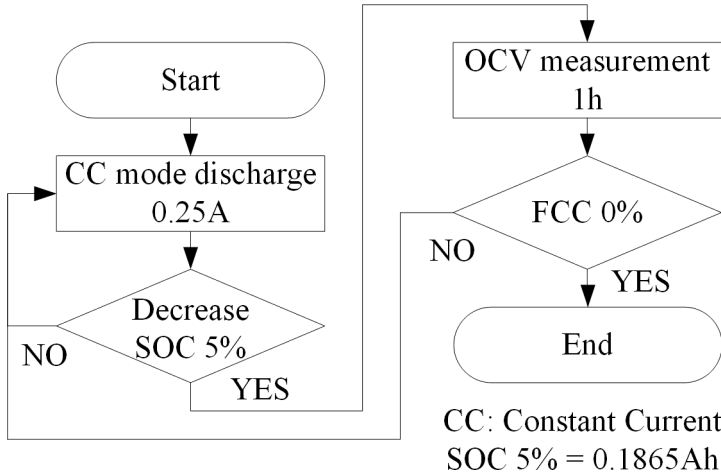
(a) Discharge phenomena



(b) Integrated current capacity



(c) Temperature

**Figure 4.** Flow diagram of OCV measurements

2. Based on the measured FCC value of 3.73Ah, the OCV values were measured for each SOC 5% (0.1865Ah) drop. The OCV measurements were conducted for one hour each time.
3. Steps 1 and 2 were repeated until the SOC value was 0%.

Figure 5 shows the results of the OCV experiments. Figure 5(a) shows the time history. The OCV value at SOC 100% was 12.65V, and the OCV value at SOC 0% was 11.18V. The experiment time was approximately 2100 minutes. Figure 5(b) shows the expanded figure of SOC 100%-95%, and it was observed that the OCV value became almost constant 5 minutes after the start of OCV measurements. Figure 5(c) shows the SOC-OCV characteristics based on the respective OCV values at 3, 5, and 10 minutes. It was found that the stable OCV value could be measured after about 5 minutes. It was realized that the SOC value could be estimated from the OCV value using Figure 5(c).

In the next chapter, the effects of disconnecting the lighting on plant development are investigated.

## 7. THE EFFECTS OF OCCASIONAL LIGHT INTERRUPTION ON PLANT CULTIVATION

The effect on cultivation when the LED lighting was turned off occasionally was investigated. A normal 100V AC power supply was used so that the tests could focus on the effect of lighting. Three systems for leaf lettuces were set up based on the results of the SOC-OCV estimation experiments in Chapter 3. The three conditions were:

**System 1** (continuous LED running)

**System 2** (10 minutes of darkness per hour)

**System 3** (5 minutes of darkness per hour)

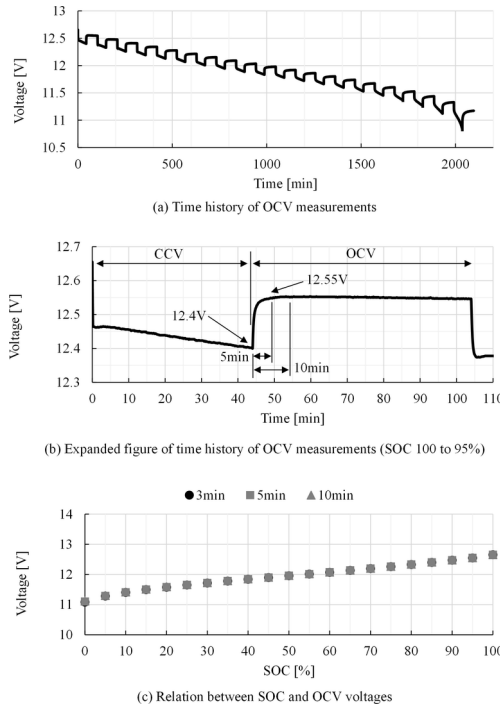
Continuous lighting is the condition of normal cultivation and served as a standard to compare with the other two systems.

### 7.1 System Design

Figure 6 shows the equipment setup used in all three systems. Where (a) is the system diagram, (b) the block diagram of the control system, and (c) the layout.

**International Journal of Manufacturing, Materials, and Mechanical Engineering**  
 Volume 11 • Issue 3 • July-September 2021

**Figure 5. Experimental results of OCV measurements**

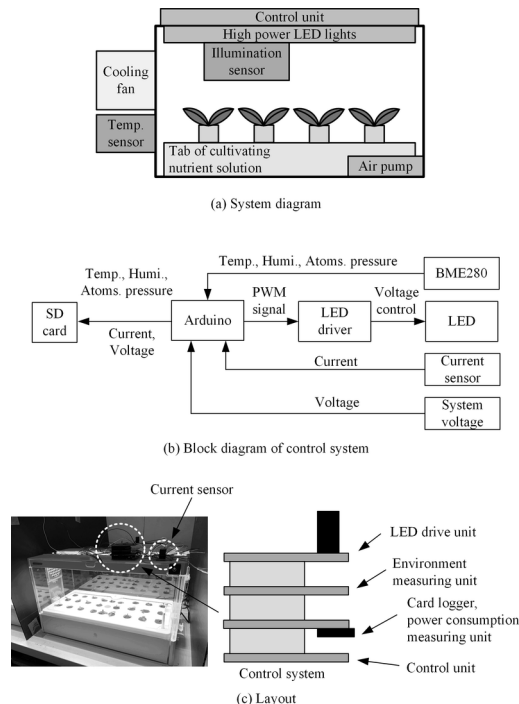


In the experiments, a commercially-available hydroponic system, Green Farm (UH-A01E1, U-ing Corporation), was used. The system dimensions are 544mm long, 262mm wide, and 305mm high. Each system was given 4 liters of cultivation solution. A normal 100V AC power supply was used, which operates at 12V DC using an AC adapter. The maximum power consumption is about 30W. It is possible to grow a maximum of 10 lettuces or 20 baby-leaf vegetables or herbs at a time.

The hydroponic device consists of a cultivation tray, white LED lighting, ventilation fan, temperature sensor, operation panel, and an air pump that supplies air to the cultivation solution. There is an openable door panel on the front of the system. LED lighting time and cultivation mode can be changed via the operation panel. The lighting time can be set arbitrarily between 10 to 24 hours in units of one hour. Cultivation modes include (1) normal mode (used during normal cultivation) and (2) germination mode (used during seed planting). When germination mode is selected, the LEDs will not light for the first 72 hours. The air pump runs for 5 minutes every hour, even when the germination mode is selected. The rotation speed of the ventilation fan is controlled using the temperature sensor.

Figure 7 shows the spectrum measurement results of the white LED used in this system. A spectrum sensor (ezSpectra OTS-815V, Nara Nogi Giken) was used to measure the spectrum. There was a sharp peak around 450 nm, and a second longer, flatter peak between 550-600 nm. Judging from the characteristics of the spectrum, it was similar to the performance of a common white LED. The control system regulated only the lighting time.

We have developed a control system, shown in Fig. 6(b), for LED lighting control and measurement of environmental data. The developed system can control more precisely the lighting intensity and lighting time of the LEDs. The control system consists of an LED drive circuit and a control circuit to control the lighting intensity and lighting time of the LED. The lighting intensity can be adjusted in 255 steps by PWM. The PWM frequency of 490Hz was used. The lighting can be set to any time from 0 to 24 hours in units of 1 second.

**Figure 6. Experimental set up of small hydroponic plant cultivation system**

The measuring unit consists of an environment measuring unit and a power consumption measuring unit. The environment measuring unit can measure temperature, humidity, and atmospheric pressure around the cultivation system. The power consumption measuring unit can measure the system voltage and LED current. The measured data is recorded on the SD card at a sampling frequency of 1 minute. The sensors used in our system are a current sensor (HPS-05-AS, UR-D), and an environmental measurement sensor (BME280, Bosch).

Figure 6(c) shows a photograph of the layout of the LED control and environment measurement devices. The system has a 4-stage module structure: the lowest stage is the control unit (Arduino UNO), the second stage from the bottom is the recording unit (SD card logger), and the power consumption measuring unit (system voltage and LED current). The third stage from the bottom is the environment measurement unit (environment sensor), and the top is the LED drive unit. The control system is powered by the main power supply and operates at 12V DC.

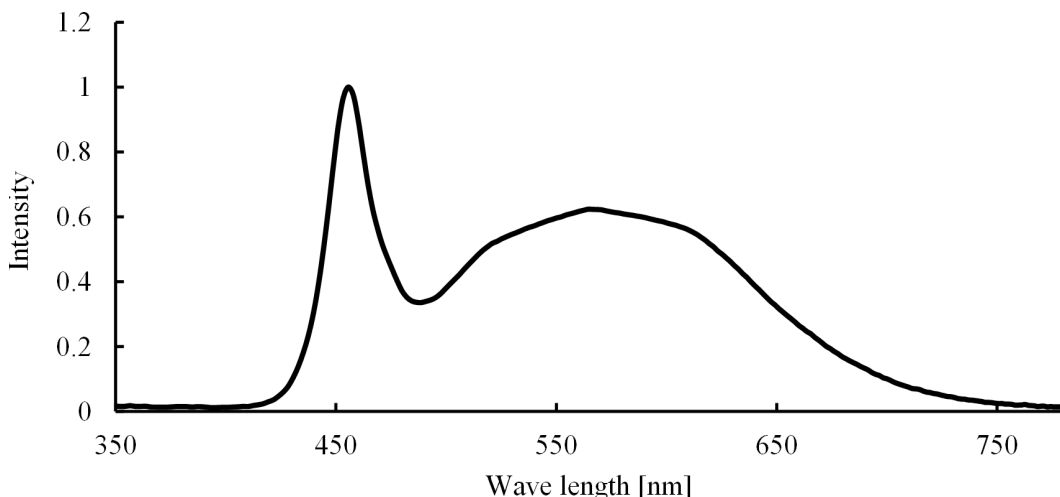
## 7.2 Conditions of Plant Cultivation Experiments

The plant cultivation experiments were conducted in a laboratory in Kanagawa Institute of Technology, Japan. The three plant cultivation systems were placed on shelves which were at the same height to avoid differences in temperature in the laboratory. Partitions of black plastic were installed between the systems to avoid lighting interference between them.

The following solution was used:

>Cultivating nutrient solution: HYPONIKA, KYOWA

The following experimental conditions were used:

**Figure 7. Spectrum of white LED used in our system**

>Room temperature: 24°C  
>Air conditioning: constant  
>Humidity: No control  
>Cultivation period: 28 days (Nov. 23 to Dec. 20, 2019)  
>Number of seed strains: 8 (for each system)  
>Seeds: Green leaf lettuce seeds from Sakata Seeds Company  
>Ventilation fan: constant  
>Air pump: 5 minutes every hour  
>LED lighting intensity: PWM 100%  
>LED lighting time:

**System 1:** 16 hours continuous LED running (5:00 to 21:00).

**System 2:** 16 hours with 10 minutes of darkness per hour (5:00-21:00), then continuous LED running (21:00-23:40).

**System 3:** 16 hours with 5 minutes of darkness per hour (5:00-21:00), then continuous LED running (21:00-22:20).

The total LED lighting times of 16 hours are the same for the three systems. Systems 2 and 3 were given 2 hours 40 minutes and 1 hour 20 minutes respectively of additional lighting to compensate for the periods of darkness:

>Data sampling frequency: once a minute

## **8. EXPERIMENTAL PROCEDURE**

The experimental procedure is shown below:

1. The germination operation is performed. Soak the seeds overnight in water, then store them overnight in a wet cloth.
2. The seeds that have germinated are planted three to one sponge.
3. After one week, leave the largest seedling on each sponge and remove the other two.
4. Change all the nutrient solution on the 7th, 14th, and 21st days after the start of cultivation.
5. Harvesting is performed on the 28th day; leaves are cut off from each plant, and their fresh weight is measured.
6. The leaves are dried at 80°C for 72 hours in a thermostat chamber.
7. The dry weight of each leaf is determined.

## 9. WEIGHT MEASUREMENTS OF LEAVES

Plants contain a large amount of water. When evaluating the weight of leafy vegetables, there are two methods for measuring fresh weight and dry weight. The fresh weight is the weight containing a large amount of water immediately after harvesting. On the other hand, the dry weight is the weight after the drying process.

According to the Japanese Food Standards Table, leaf lettuce has a water content of about 94.0%. However, since the amount of water varies from plant to plant, the dry weight is used as a more accurate measurement. There are several types of drying methods such as atmospheric pressure drying, reduced pressure drying, and Karl Fischer Titration (Suzanne, 2017). Although reduced pressure drying is recommended for vegetables, the direct method is common because the former requires large and costly equipment. In this paper, drying was carried out by the direct method of atmospheric pressure drying. After testing some leaves, the drying time was set to 72 hours because this was determined to be the time after which the mass does not change. Water content is calculated from the following formula:

$$WC = \frac{W1 - W2}{W1} \times 100$$

WC: Water content

W1: Fresh weight [g]

W2: Dry weight [g]

## 10. EXPERIMENTAL RESULTS

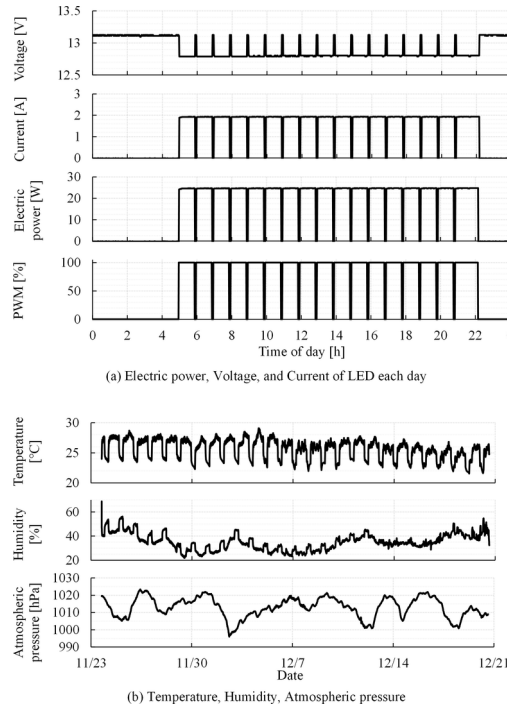
Figure 8(a) shows the electric power, voltage, and current for one day. This data is almost the same for all three systems. The electric power when the LED was on was about 24W, and the average daily electric power was 16.3W. The system voltage was about 13V, the current when the LED was on was about 1.9A, and the average current per day was about 1.3A. Over the 28 days, the total electric power consumption was 10,953Wh.

Figure 8(b) shows ambient temperature, humidity, and atmospheric pressure in System 3. In all systems, when the LED is lit, the temperature rose by about 3 or 4°C. As the amount of saturated water vapor changes, the humidity also changes accordingly. The humidity averaged 35% because of dry winter conditions. Temperatures averaged 25.6 °C and atmospheric pressure averaged 1013hPa.

Table 1 shows the fresh weight and dry weight in each system. Figure 9(a) shows the average value of the dry weight in each system. System 3 had the highest average fresh weight of 26.83 g. The second was System 1 with 22.89 g. System 2 had the smallest average weight of 19.8 g. System

**International Journal of Manufacturing, Materials, and Mechanical Engineering**  
 Volume 11 • Issue 3 • July-September 2021

**Figure 8. Results of system and environment**



3 produced the plant with the largest fresh weight of 46.8 g. The average dry weight was 1.1g for System 1, 1.0g for System 2, and 1.3g for System 3. As shown in Table 1, one plant in each system did not develop. Also, there was one extremely small plant in each system.

A large variation in fresh weight was observed in each system. The following are thought to be factors: variations in lighting intensity of individual LEDs, variations due to LED placement, and unknown factors such as the health of each seed. Generally, in the case of leaf lettuce, it is recommended that the distance between plants be around 150-200 mm. However, in this cultivation system, the distance between plants is shorter than recommended; about half. When some plants grew more rapidly due to variations in lighting intensity or other reasons, plants adjacent to these received less LED light, resulting in plants with a significantly smaller weight.

The water content was calculated by comparing the fresh weight and the dry weight was examined. The average water content of each system was:

**System 1:** 95.0%

**System 2:** 95.1%

**System 3:** 95.5%

The plant with the highest water content of 96.0% was from System 3; the plant with the lowest water content of 94.5% was from System 2. Generally, the variation band across the three systems was very narrow (as can be seen in Figure 9(b)).

Figure 10(a) shows a photograph of one whole system. The size of the harvested leaves was almost the same in all three systems. The three largest leaves are shown in Fig. 10(b). The largest leaf had a total length of 180 mm and measured about 150 mm at its widest point.

Judging from the results of weight measurements and leaf size, cutting the LED lights in Systems 2 and 3 for 5 or 10 minutes per hour seems to have little effect on the growth of leaf lettuces.

This time, the experiment was conducted with 1 hour as the time unit. This time unit was considered suitable for the calculation of the CI method (being not too short or too long for accurate measurements). Longer lighting duration may be possible and needs to be considered.

## 11. CONCLUSION

A method for estimating the remaining battery capacity (SOC) for a small hydroponic system using sustainable energy was investigated, and the effect of the method on plant cultivation was examined. In the proposed CI-OCV method, the CI method is used for a certain time (for example, one hour), then the OCV method is used during a cut off period (for example, 5 minutes). This process is then repeated. In the CI-OCV method, as in the OCV method, it is necessary to wait for a certain time interval to obtain a stable constant SOC value.

In this paper, the time interval required for SOC estimation was investigated. Moreover, the effect of the SOC estimation time interval on plant cultivation was examined. Previous experiments using lead-acid batteries had revealed that the time interval required for SOC estimation is about 5 minutes. The experiment was repeated by turning on the LED light for 1 hour and turning off the LED light for 5 or 10 minutes, and it was revealed that there was almost no effect on the growth of plants when compared with continuous LED lighting.

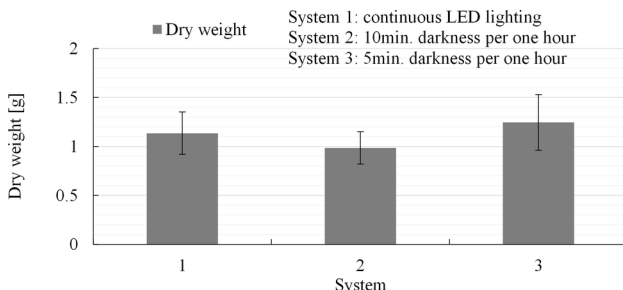
This time, the experiments were conducted with small tabletop cultivation systems that can grow about 10 lettuces. In the future, it is expected that a system that can grow a larger number of plants at a time will be developed and its practicality improved.

**Table 1. Weight of produced plants**

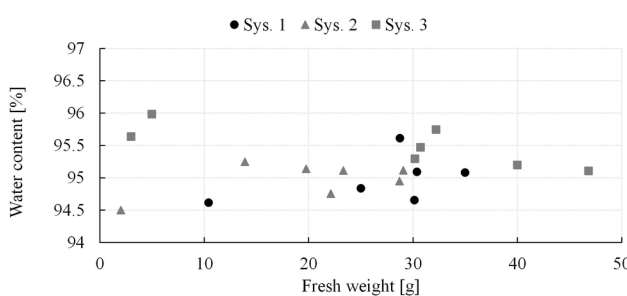
Place	Fresh weight [g]			Dry weight [g]			Water content [%]		
	Sys. 1	Sys. 2	Sys. 3	Sys. 1	Sys. 2	Sys. 3	Sys. 1	Sys. 2	Sys. 3
1	35.0	28.7	30.7	1.7	1.5	1.4	95.1	94.9	95.5
2	0.6	13.9	3.0	-	0.7	0.1	-	95.2	95.6
3	30.4	-	32.2	1.5	-	1.4	95.1	-	95.7
4	-	22.1	40.0	-	1.2	1.9	-	94.8	95.2
5	10.4	19.8	30.2	0.6	1.0	1.4	94.6	95.1	95.3
6	28.7	29.1	5.0	1.3	1.4	0.2	95.6	95.1	96.0
7	30.1	23.3	46.8	1.6	1.1	2.3	94.7	95.1	95.1
8	25.0	2.0	-	1.3	0.1	-	94.8	94.5	-
Max.	35.0	29.1	46.8	1.7	1.5	2.3	95.6	95.2	96.0
Min.	0.6	2.0	3.0	0.6	0.1	0.1	94.6	94.5	95.1
Average	22.9	19.8	26.8	1.3	1.0	1.2	95.0	95.0	95.5
Median	28.7	22.1	30.7	1.4	1.1	1.4	95.0	95.1	95.5
Stand. error	4.4	3.3	5.8	0.2	0.2	0.3	0.1	0.1	0.1

**International Journal of Manufacturing, Materials, and Mechanical Engineering**  
Volume 11 • Issue 3 • July-September 2021

**Figure 9. Results of produced plants (weight and water content)**



(a) Weight of produced plants

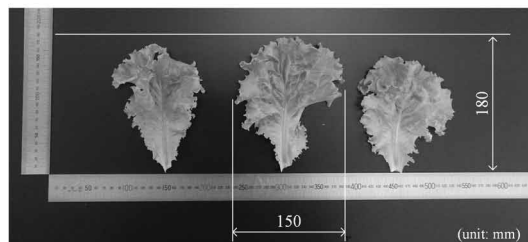


(b) Relationship between fresh weight and water content

**Figure 10. Photographs of produced pants**



(a) One whole system



(b) Three best leaves

## REFERENCES

- Dinesh, H., & Pearce, J. M. (2016). The potential of agrivoltaic systems. *Renewable & Sustainable Energy Reviews*, 54, 299–308. doi:10.1016/j.rser.2015.10.024
- Dupraz, C., Marrou, H., Talbot, G., Dufour, L., Nogier, A., & Ferard, Y. (2011). Combining solar photovoltaic panels and food crops for optimizing land use: Towards new agrivoltaic schemes. *Renewable Energy*, 36(10), 2725–2732. doi:10.1016/j.renene.2011.03.005
- Fathabadi, H. (2017). Novel standalone hybrid solar/wind/fuel cell/battery power generation system. *Energy*, 140(Part 1), 454–465. doi:10.1016/j.energy.2017.08.098
- George, A. X., Stelios, L., & Konstantinos, B. (2017). Energy demand analysis via small scale hydroponic systems in suburban areas - An integrated energy-food nexus solution. *The Science of the Total Environment*, 610–617. PMID:28363175
- Goetzberger, A., & Zastrow, A. (1982). On the Coexistence of Solar-Energy Conversion and Plant Cultivation. *International Journal of Solar Energy*, 1(1), 55–69. doi:10.1080/01425918208909875
- Holtz, B. R., Berquist, B. R., Bennett, L. D., Kommineni, V. J., Munigunti, R. K., White, E. L., Wilkerson, D. C., Wong, K. Y., Ly, H. L., & Marcel, S. (2015). Commercial-scale biotherapeutics manufacturing facility for plant-made pharmaceuticals. *Plant Biotechnology Journal*, 13(8), 1180–1190. doi:10.1111/pbi.12469 PMID:26387511
- Kamada, T. (2019). Waga Kuni ni okeru Einogata Taiyoko Hatsuden no Genjou. *Sabaku Kenkyu*, 29(2), 75–80.
- Kozai, T. (2013). Plant Factory in Japan - Current situation and perspectives. *Chronica Horticulturae*, 53(2), 8–11.
- Motosugi, T., Yamaguchi, S., & Takahashi, Y. (2019). Battery Remaining Charge Estimation for Small Hydroponic Plant Cultivation System. *IEEE Int. Conf. on Control, Automation and Systems*, 821–826. doi:10.23919/ICCAS47443.2019.8971556
- Nozu, T. (2018). Analysis on Farmers' Willingness of Implement to Combinations of Solar Photovoltaic and Food Crops. *Noson Keikaku Gakkaishi*, 37(3), 304–311. doi:10.2750/arp.37.304
- Othman, N. F., Mat Su, A. S., & Ya'acob, M. E. (2018). Promising Potentials of Agrivoltaic Systems for the Development of Malaysia Green Economy. *IOP Conference Series. Earth and Environmental Science*, 146(1), 012002. doi:10.1088/1755-1315/146/1/012002
- Palande, V., Azheer, A., & George, K. (2018). Fully Automated Hydroponic System for Indoor Plant Growth. *Procedia Computer Science*, 129, 482–488. doi:10.1016/j.procs.2018.03.028
- Prannay, R. M., Utkarsh, S. S., & Joshua, M. P. (2017). Agrivoltaic potential on grape farms in India. *Sustainable Energy Technologies and Assessments*, 23, 104–110. doi:10.1016/j.seta.2017.08.004
- Rekioua, D., Bensmail, S., & Bettar, N. (2014). Nabila Bettar, Development of hybrid photovoltaic-fuel cell system for stand-alone application. *International Journal of Hydrogen Energy*, 39(3), 1604–1611. doi:10.1016/j.ijhydene.2013.03.040
- Scognamiglio, A. (2016). 'Photovoltaic landscapes': Design and assessment. A critical review for a new transdisciplinary design vision. *Renewable & Sustainable Energy Reviews*, 55, 629–661. doi:10.1016/j.rser.2015.10.072
- Sekiyama, T., & Nagashima, A. (2019). Solar Sharing for Both Food and Clean Energy Production: Performance of Agrivoltaic Systems for Corn, A Typical Shade-Intolerant Crop. *Environments*, 2019(6), 65. doi:10.3390/environments6060065
- Snihir, I., Rey, W., Verbiskiy, E., Belfadhel-Ayeb, A., & Notten, P. H. L. (2006). Battery open circuit voltage estimation by a method of statistical analysis. *Journal of Power Sources*, 159(2), 1484–1487. doi:10.1016/j.jpowsour.2005.11.090
- Suzanne, N. (2017). Food Analysis. Springer International Publishing.
- Uchiyama, R., Yamaguchi, S., & Takahashi, Y. (2019). Solar Power Generation for Compact Hydroponic Plant Cultivation System. *Int. Conf. on Control, Automation and Systems*, 827–832. doi:10.23919/ICCAS47443.2019.8971554

**International Journal of Manufacturing, Materials, and Mechanical Engineering**

Volume 11 • Issue 3 • July-September 2021

Xing, Y., He, W., Pecht, M., & Tsui, K. L. (2014). State of charge estimation of lithium-ion batteries using the circuit voltage at various ambient temperatures. *Applied Energy*, 113, 106–115. doi:10.1016/j.apenergy.2013.07.008

Yamaguchi, S., Motosugi, T., & Takahashi, Y. (2019). Relationship between LED Energy Consumption and Plant Growth in Small Hydroponic Cultivation System. *Int. Conf. on Control, Automation and Systems*, 451–455. doi:10.23919/ICCAS47443.2019.8971624

Yamaguchi, S., Takahashi, Y., & Hayashi, T. (2018). Small Indoor Hydroponic System with Renewable Energy. *Int. Conf. on Control, Automation and Systems*, 313–318.

Yoshiga, T., & Umezaki, Y. (2016). A simple and small-scale hydroponic culture system for obtaining second-stage juveniles of the root-knot nematode. *Applied Entomology and Zoology*, 51(1), 151–154. doi:10.1007/s13355-015-0365-4

Yunez-Cano, A., González-Huerta, R. de G., Tufiño-Velázquez, M., Barbosa, R., & Escobar, B. (2016). Solar-hydrogen hybrid system integrated to a sustainable house in Mexico. *International Journal of Hydrogen Energy*, 41(43), 19539–19545. doi:10.1016/j.ijhydene.2016.06.203

Zhang, X., He, D., Niu, G., Yan, Z., & Song, J. (2018). Effects of environment lighting on the growth, photosynthesis, and quality of hydroponic lettuce in a plant factory. *International Journal of Agricultural and Biological Engineering*, 11(2), 33–40. doi:10.25165/j.ijabe.20181102.3240

Satoru Yamaguchi received his M.Sc. from the Graduate School of Engineering, Kanagawa Institute of Technology, Japan, in 2013. After completing his master's degree program, he joined Honda Elesys Corp. Ltd. (Now, Nidec Elesys Corp.), and then joined Robit Inc. in 2017. He returned to Kanagawa Institute of Technology where he is currently studying a doctoral program, in addition to working as an engineer for Robit Inc. His main area of research focuses on robotic applications in sustainable energy and agriculture.

Takuya Motosugi received his M.Sc. in 2020 from the Graduate School of Engineering, Kanagawa Institute of Technology, Japan, and joined Isuzu Motors Limited. His main area of research focuses on the application of battery management technology for automobiles and agriculture systems.

Yoshihiko Takahashi is currently Professor at Kanagawa Institute of Technology, Japan. He received both his M.Sc. and PhD from the Graduate School of Engineering, Tokyo University of Agriculture and Technology, Japan, in 1980 and 1995 respectively. After completing his M.Sc. course, he worked for Toshiba Corporation, Japan, as a researcher in mechatronics engineering and control engineering. He joined Kanagawa Institute of Technology, Japan, as an Associate Professor in 1996. He is interested in robotic engineering in agriculture and for service robots, human interfaces, electric vehicles, mechatronics education, etc.

# Dynamic Analysis and Simulation of the Hydraulic Control System on the Remote-Controlled Explosive Ordnance Disposal Machine

Dat Duy Nguyen, Le Quy Don Technical University, Vietnam

Dat Van Chu, Le Quy Don Technical University, Vietnam

Le Van Sy, Petrovietnam University, Vietnam

 <https://orcid.org/0000-0003-1590-0039>

## ABSTRACT

The remote-controlled explosive ordnance disposal machine, an important device used in the military, has been developed in many countries. It has become more intelligent and multi-functional due to being integrated with many functional components. New generations have been equipped with a completely remote-controlled system and high-resolution cameras. In bomb disposal work, this integrated machine can be used to replace other single-operating machines which allow to reduce greatly consuming time and labor effort as well as safety for operators. There are significant distinctions in design among well-known manufacturers. One of important components of this machine is hydraulic system that drives operating equipment of the machine. This paper focuses on analyzing and simulating dynamic model of the hydraulic system during the bomb laying process. The main target of this study is to meet the requirements for controlling a remote-controlled explosive ordnance disposal machine with high specific power, low hysteresis, high precision control, which ensures precision operation and safety.

## KEYWORDS

Bomb/Mine Clearance, Dynamic Analysis, EODM, Excavator, Hydraulic System, LS-PC Control

## 1. INTRODUCTION

Bomb/mine clearance and explosive ordnance disposal are urgent tasks of war-damaged countries worldwide. Many technologies have been developed for both semi-automation and full automation systems for decades. The first designing concept of a remote-controlled explosive ordnance disposal machine (EODM) was presented in the 1990s (Burks, 1992; Terwelp, 2003). Based on the draft concepts, many commercial products of EODMs have been introduced by manufacturers such as UBIM (Russia), Wisent (Germany), Kodiak (UK), etc. (Terwelp, 2003). In recent years, due to the high demand for cleaning bombs/mines after the Vietnam war, preliminary studies of EODMs have been investigated and applied to manufacture. EODMs have been equipped with integrated operational devices such as radar detectors, digging devices, bomb pickers, high-pressure water jets and hydraulic hammers. These machines can replace single functional machines which are currently used for clearing bombs and explosive ordnance disposals such as single-bucket excavators, high-pressure water jetting devices and bomb picking devices. Moreover, EODMs have been developed

DOI: 10.4018/IJMMME.2021070103

Copyright © 2021, IGI Global. Copying or distributing in print or electronic forms without written permission of IGI Global is prohibited.

with more intelligent, multi-functional and multi-purpose operations, with fully controlled systems, high-resolution cameras and smart sensors. Not only is this application user-friendly, highly accurate and time-and-effort saving, but it also ensures almost perfect safety for operators following EODM standards (Manz, 2001; Fleming, 2004; Lee, 2019). These standards are also the current trend in applying autonomous systems to both civil and military industries when considering human factors and political risks in the near future of the automation technology (Pratt Rogers, 2019).

Through the continuous development and maturation of the current technology, numerous challenges have been faced by researchers in the practical use of EODMs and autonomous vehicles. These challenges have motivated business models, national ethics, legality, etc. to improve (Chai, 2020). Despite certain similarities in the use and functions of EODMs across manufacturers worldwide, significant differences in the control system design can be found. Especially, the design of hydraulic systems that drive working equipment (1. Base machine; 2. Boom; 3. Arm; 4. Excavation – gripper bomb mechanism in Fig. 1a) to carry out soil excavation (David, 1998; Chang 2002; Casoli, 2013; Wang, 2014; Ge, 2017), bomb picking and transportation (Sulaiman, 2016; Manz, 2001; Terwelp, 2003; Wang, 2014; Fleming, 2004) onto specialized vehicles and other tasks is unique to individual manufacturers. Comparing to electric and pneumatic drive systems, the hydraulic drive system has higher specific power, lower hysteresis and higher precision control (Casoli, 2013; He, 2018).

For remote control system, Burks (1994) and Fleming (2004) designed a hydraulic system using the proportional pressure reducing valve associated with the joystick. The control system equipped with hydraulic equipment having the present tele-operated system is suitable for a wide range of devices operating in dangerous working environments. The authors demonstrated that the teleoperated excavator has operated effectively, robustly and durably. Zhang (2005) established the full kinematic and dynamic models to control the excavator arm with three degrees. The excavator was controlled by the electrohydraulic proportional valves associated with sensors and a computer control system which allows high control performance with the full nonlinear math model of the electrohydraulic proportional system. Yosof (2015) and Sulaiman (2016) designed a master-slave system using a tele-operated electro-hydraulic actuator (T-EHA) to control a mini excavator. This system is useful for tele-operation support of heavy construction and road restoration. The authors presented a position control mathematical model and operational evaluation. The result shows the control system has good response to the tele-operated electro-hydraulic actuator. However, these studies have not evaluated the dynamics of the system in both theoretical and practical aspects. Yoshinada (2019) solved these problems by developing a construction robot for disaster relief tasks with a new mechanism and new control methods. The authors combined the basic configuration of the robot and the teleoperation system which can quickly improve motion control characteristics and remote controllability. The system redesigned the current hydraulic excavator mechanism and the hydraulic control and operation system from their very origins, which allows quick increase of construction equipment's capacity to deal with large-scale disasters and problems.

The system served for multi-functions required to save the hydraulic energy (Congmei, 2011; Yang, 2013; Casoli, 2016; Ge, 2017; Sprengel, 2017; He, 2018; Bedotti, 2018). The previous studies did not focus on the pump equipped for the hydraulic system. Thus, the pump for the hydraulic system required a load sensing (LS) control system. The speed and displacement variable pump with load sensing-pressure compensator (LS-PC) control system should be equipped in the hydraulic system of EODMs. In addition, the researchers used Lagrange equations in dynamic analysis of the hydraulic actuator which are improper for the exact control process for EODM operating components (Zhang, 2005; Dragoljub, 2017).

This paper presents the dynamics model of working equipment and the hydraulic drive system during the bomb laying process in order to meet the requirements set out when the bomb is placed on a specialized vehicle. Accordingly, the hydraulic system used in the remote-controlled explosive disposal machine is analysed and modelled. In addition, it was modeled fully upon the LS-PC control pump using mechanical feedback to the control system which consists of a proportional pressure

reducing valve and a main valve integrated with a pressure compensation valve. The model of working equipment during bomb-laying process was fully assembled based on Newton-Euler approach by analyzing forces and masses assigned to the considered components. All hydraulic components, lifting equipment as well as input control signals are simulated with LMS Amesim software to make dynamic assessments for the system (Wei, 2011; Yang, 2013; Gimadiev, 2014; Man, 2015; Vaseliu, 2018).

## 2. GENERAL STRUCTURES AND COMPONENTS OF AN EODM

The remote-controlled explosive ordnance disposal machine is developed and manufactured widely in the world. The machine is designed to provide enhanced bomb disposal capabilities to explosive ordnance disposal teams. It is required to operate with high reliability and excellent manoeuvrability which help identify and disarm booby traps, fireworks, improvised explosive devices and other dangerous objects in both military and civil purposes. General structures are shown in Figure 1, including main components such as base machine, boom, arm, excavation and gripper bomb mechanism.

The kinematic and structural parameters are shown in Figure 1a). The required displacement, the velocity graph of center gravity of excavation/gripper bomb mechanism during the bomb laying process in working plane ( $x_1O_1y_1$ ) are shown in Figure 1b). In this figure,  $O_4^0$  - Point  $O_4$  is the original position;  $O_4^1$  - Point  $O_4$  is the end position;  $v_{x_1} = 0 \text{ m / s}$ .  $G_{1-3}$  are the weight of the parts in the machine when being placed at their centroids.

The hydraulic system needs to ensure the movement of the cylinder - boom, arm and bucket with the given movement, velocity and good energy characteristics. The previous studies showed that the throttle-controlled hydraulic drive system is eliminated due to its low efficiency. The hydraulic system with volumetric control has high efficiency but it has some disadvantages such as complicated structure, large volume and being bulky (Chang, 2002; Yamamoto, 2010; Gu, 2012; Yang, 2013; Vaha, 2013; Wang, 2014; Man, 2015; Vaseliu, 2018; Liang, 2018, Ha, 2019). In recent years, hydraulic drive systems combined with pump - valve control have been commonly used for designing the EODM including LS (Load sensing), FS (Flow sharing) and FM (Flow matching) hydraulic drive systems and FS hydraulic systems.

In this study, a flow sharing (FS) hydraulic drive system of the machine was carried out which has high efficiency, no saturation of the pump flow and low hysteresis. The pump of the hydraulic drive system FS provides a fluid flow for the operating units with pressure equal to the load pressure plus the pressure drop in the control devices (from 0.8 to 1.5 Mpa). To control the operating equipment, the remote-controlled explosive ordnance disposal machine uses electric-proportional pressure reducing valves to control the main valves.

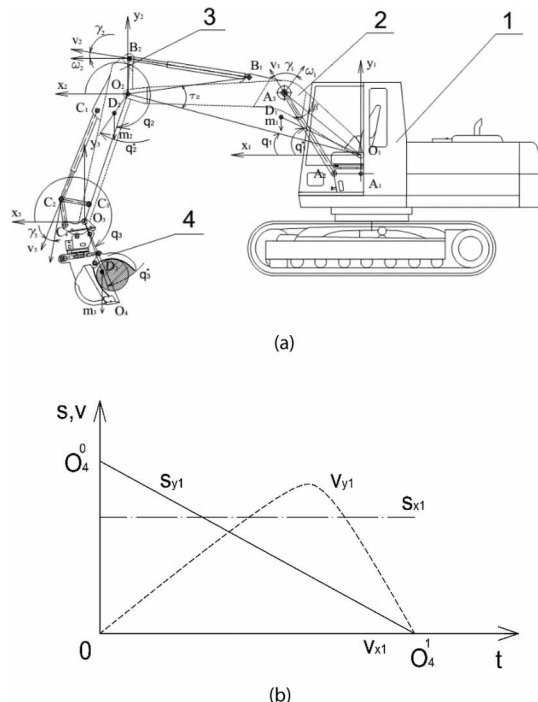
## 3. MATHEMATICAL MODEL OF WORKING EQUIPMENT AND HYDRAULIC DRIVE SYSTEM

### 3.1 The Assumptions Used in Mathematical Model

In this study, dynamic analysis and simulation for the operating units and hydraulic drive system are based on the following assumptions:

- The flow coefficient on the throttle and working windows of the control valve is constant;
- The leakage of the working fluid through the radial clearance of the control valve and the working cylinder is neglected;
- The torque on the inclined disk of the pump, created by the mass of moving components to the servo piston, is considered small as compared to the components of the driving force;

**Figure 1.** (a) General form of an EODM and construction and kinematics of working equipment; (b) Graph of required displacement and speed of an EODM working equipment



- The oil pressure on the drain is constant and equal to zero;
- Friction force in the movement of spools in pressure compensating valves is neglected;
- When lifting the working equipment, the gripper mechanism is fully fixed and considered as a link with a mass of  $m_3$ ;
- The weight of the boom, arm and gripper mechanism ( $m_1, m_2, m_3$ ) is in the center gravity of the link;
- The stiffness of the boom, arm and other components of the gripper mechanism is large enough for their deformation to be neglected. The deformation in the hinge position is simultaneously neglected.

The detailed analysis and calculation of an EODM are presented in [1], the block diagram of the hydraulic drive system is shown in Figure 2a. Based on these assumptions, mathematic models for each component in the hydraulic system are established in the next section. This paper summarizes the main formula of transfer function and presents full structure diagram of the hydraulic system controlling working equipment in Figure 4. This diagram is used as input for the simulating software called LMS Amesim.

### 3.2 Mathematical Model of Pump With LS-PC Control

The connecting pipes in the system are short, which can bypass the hydraulic resistance in the pipes, as well as the distribution of the working fluid parameters along the length of the pipe. Given the continuous state of the fluid flow, the flow equation in the high pressure pipeline is expressed as:

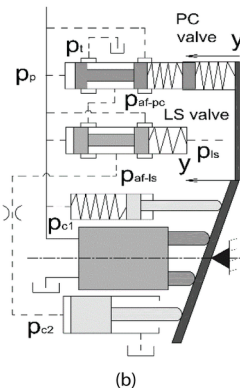
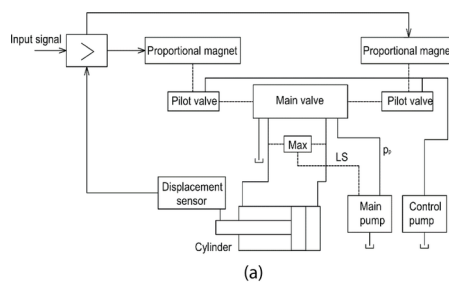
$$k_{com} \frac{dp_p}{dt} = Q_p - Q_s - Q_c \quad (1)$$

- $k_{com}$  - Fluid compression rate;
- $p_p$  - Pump pressure;
- $Q_p$  - Flow of the pump;
- $Q_s$  - Required flow of the system;
- $Q_c$  - Flow rate to the control line.

LS valve is used to transmit the pressure difference between pump pressure and load pressure. The position of the LS valve spool is determined by the balance of forces between the force created by the pressure difference and the compression force of the LS valve spring (Figure 2b). PC valves are installed to ensure the safety of the system, maintaining a power balance between the pump and the motor. The transfer function of the PC valve represents the relationship between the movement of the PC valve spool and the pump pressure, the displacement of the servo piston:

$$W_{pc}(s) = \frac{k_{pc}}{T_{pc} \cdot s + 1} \quad (2)$$

Figure 2. (a) Block diagram of the hydraulic drive (for one cylinder); (b) Schematic diagram of hydraulic pump with LS-PC control



**International Journal of Manufacturing, Materials, and Mechanical Engineering**  
 Volume 11 • Issue 3 • July-September 2021

where:

- $k_{pc} = \frac{1}{c_{sp-pc}}$  - Transfer function gain;
- $T_{pc} = \frac{k_{fr-pc}}{c_{sp-pc}}$  - Transfer function time constant
- $k_{fr-pc}$  - Coefficient of friction in the radial clearance of the PC valve;
- $c_{sp-pc}$  - Stiffness of the PC valve spring.

The transfer function of the LS valve represents the relationship between the displacement of the LS valve and the control pressure and is expressed as follows:

$$W_{ls}(s) = \frac{k_{ls}}{T_{ls} \cdot s + 1} \quad (3)$$

where:

- $k_{ls} = \frac{1}{c_{sp-ls}}$  - Transfer function gain;
- $T_{ls} = \frac{k_{fr-ls}}{c_{sp-ls}}$  - Transfer function time constant;
- $k_{fr-ls}$  - Coefficient of friction in the radial clearance of the LS valve;
- $c_{sp-ls}$  - Stiffness of the LS valve spring.

In the normal operating state, the  $p_{af-pc}$  pressure value receives two values,  $p_p$  or  $p_t$ , depending on the displacement value. As the flow through the LS valve is equal to the flow going into the servo piston, we have the following equation:

$$(k_{Qcls} + k'_{Qcls}) \cdot x_{ls} - k'_{Qcls} \cdot x_{cl} + k_{Qpls} \cdot p_p = F_{c2} \frac{dy}{dt} + \frac{V_{c2}}{B_{com}} \cdot \frac{dp_{c2}}{dt} + (k_{Qpls} + k'_{Qpls}) \cdot p_{c2} \quad (4)$$

where:

- $F_{c2}$  - End section of servo pistons;
- $V_{c2}$  - Servo cylinder volume;
- $B_{com}$  - Modulus of elasticity of hydraulic oil;
- $p_{c2}$  - Oil pressure in servo cylinder.

The transmission function of the servo piston shows the relationship between the displacement of the servo piston and the control pressures as follows:

$$W(s) = \frac{k_{c2}}{T_{c2}^2 \cdot s^2 + 2 \cdot \varepsilon \cdot T_{c2} \cdot s + 1} \quad (5)$$

where:

- $k_{c2} = \frac{1}{c_{sp-cl}}$  - Servo piston transfer function gain;
- $T_{c2} = \sqrt{\frac{m_c}{c_{sp-cl}}}$  - The time constant of the servo piston transfer function;
- $m_c$  - Mass of servo piston;
- $c_{sp-cl}$  - Stiffness of the spring in control cylinder 1.

### 3.3 Mathematical Model of Pressure Reducing Valve

The transfer function between the main valve spool movement and the electric current is as follows:

$$W_r(s) = \frac{k_r}{T_r \cdot s + 1} \quad (6)$$

where:

- $k_r = \frac{k_i \cdot F_r^*}{k_{Qp} \cdot k_{pr} \cdot k_{sp-r}^* \cdot F_{r3}}$  - Gain of the transfer function of the pressure reducing valve;
- $T_r = \frac{k_{pr3} \cdot (F_r^*)^2}{k_{Qp} \cdot k_{pr} \cdot k_{sp-r}^*}$  - Time constant of the pressure reducing valve transfer function;
- $k_i$  - coefficient of electric force;
- $F_{r3}$  - Section of auxiliary valve;
- $F_r^*$  - Effective section of the main valve;
- $k_{sp-r}^*$  - Stiffness of main valve spring.

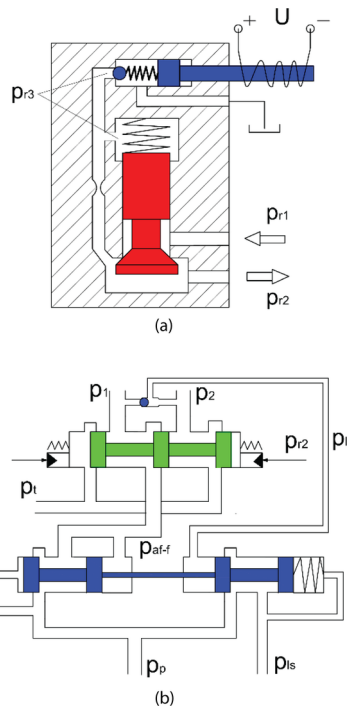
The flow through the main valve may be expressed as:

$$Q_r^* = k_{Qx_r} \cdot x_r^* + k_{Qp_r} \cdot (p_{r1} - p_{r2}) \quad (7)$$

where:

- $p_{r1}$  - Pressure supplied by the control pump;
- $k_{Qx_r}$ ,  $k_{Qp_r}$  - The linear coefficients.

**Figure 3. (a) Mathematical model of proportional pressure reducing valve; (b) Mathematical model of the main valve**



### 3.4 Mathematical Model of the Main Valve

The transfer function represents the relationship between the displacement of the main valve spool and the proportional valve's parameters as illustrated in the following formula:

$$W_v(s) = \frac{k_v}{T_v \cdot s + 1} \quad (8)$$

where:

- $k_v = \frac{F_v \cdot k_{Qx_r}}{k_{Qp_r} \cdot c_{sp}}$  - Gain of the main valve transfer function;
- $T_v = \frac{F_v^2 + k_{fr} \cdot k_{Qp_r}}{k_{Qp_r} \cdot c_{sp}}$  - Time constant of the main valve transfer function;
- $k_{fr}$  - Coefficient of friction in the gap between the spool and valve cover.

In the direction of flow into the working cylinder, we have the following equation:

$$\frac{V_{cy}}{B_{com} \cdot k_{Qp_v}} \cdot \frac{dp_{cy}}{dt} + p_{cy} = \frac{k_{Qx_v}}{k_{Qp_v}} \cdot x_{sp} - \frac{F_{cy}}{k_{Qp_v}} \cdot \frac{ds_{pi}}{dt} + p_{af-f} \quad (9)$$

where:

- $p_{af-f}$  - Pressure after flow control valve;
- $k_{Qx_v}, k_{Qp_v}$  - The linear coefficients;
- $p_{cy}$  - Pressure in the cylinder chamber of the hydraulic cylinder;
- $s_{pi}$  - Movement of the working cylinder piston;
- $F_{cy}$  - Section of the cylinder chamber.

The mathematical model for integrated pressure compensation valves (comprising two pressure control valves, flow control valves and pressure reducing valves) are analyzed separately according to the working characteristics of each valve. The dynamic equation of the pressure compensating valve spool is as follows:

$$F_f \cdot (p_p - p_{af-f} + p_{lo} - p_{ls}) = k_{sp-r} \cdot x_{com} \quad (10)$$

where:

- $F_f$  - Section of the flow control valve spool;
- $p_{af-f}$  - Pressure after flow control valve;
- $x_{com}$  - Movement the pressure compensating valve spool;
- $p_{lo}$  - The pressure generated by the load which is equal to the pressure in the working chamber of the working cylinder;
- $p_{ls}$  - The pressure LS.

Because the flow through the flow control valve is equal to the flow passing through the main valve, we have the following equation:

$$k_{Qx_f} \cdot x_{com} + k_{Qp_f} \cdot p_p - k_{Qx_v} \cdot x_{sp} - (k_{Qp_f} + k_{Qp_v}) \cdot p_{af-f} + k_{Qp_v} \cdot p_{lo} = 0 \quad (11)$$

where:

- $k_{Qx_f}, k_{Qp_f}$  - The linear coefficients.

Because the cross section of the LS valve is small, it is possible to ignore the compressive strength of the oil, then the above equation can be rewritten as follows:

$$k_{Qx_r} \cdot x_{com} + k_{Qp_r} \cdot p_p - k_{Qp_r} \cdot p_{ls} - F_{ls} \cdot \frac{dx_{ls}}{dt} = 0 \quad (12)$$

### 3.5 Mathematical Model of Force Cylinder

Figure 1a shows a diagram of calculating the boom, arm and excavation - gripper bomb mechanism and gives the symbols:  $l_1$  - Length from center of rotation  $O_1$  to center gravity  $G_1$ ;  $l_2$  - The length from the center of rotation  $O_2$  of arm to centroid  $G_2$ ;  $l_3$  - The length from the center of rotation  $O_3$  of excavation - gripper bomb mechanism to the centroid  $G_3$ ;  $P_{cy1}$ ,  $P_{cy2}$ ,  $P_{cy3}$  which are the forces generated by hydraulic cylinders of the driving boom, arm and excavation - gripper bomb mechanism. The forces of the weight of the working device and the bomb are acted on the end of the rod. Ignoring the deformation of the structure at the bonding positions and only considering a force cylinder, the equation for the dynamics of the working cylinder is as follows:

$$F_{cy-i} \cdot p_{cy-i} - k_{fri-cy} \cdot \frac{ds_i}{dt} - P_{Li} = (m_{mod-i} + m_{pi-i}) \cdot \frac{d^2 s_i}{dt^2} \quad (13)$$

where:

- $P_{Li}$  - External forces exerted on the working mechanisms are transformed to the rod head; and
- $m_{mod-i}$  - Modified masses are assigned to the working cylinder.

From the analysis of the above mathematical models, we can build a complete mathematical model for a hydraulic system driving a force cylinder (for example, the cylinder of the boom) as shown in Figure 4 with static load acting on the head of the rod; masses are transformed to the head of the rod according to the generalized coordinates  $q_1$ ,  $q_2$ ,  $q_3$ .

## 4. THE RESULTS OF CALCULATION AND SIMULATION

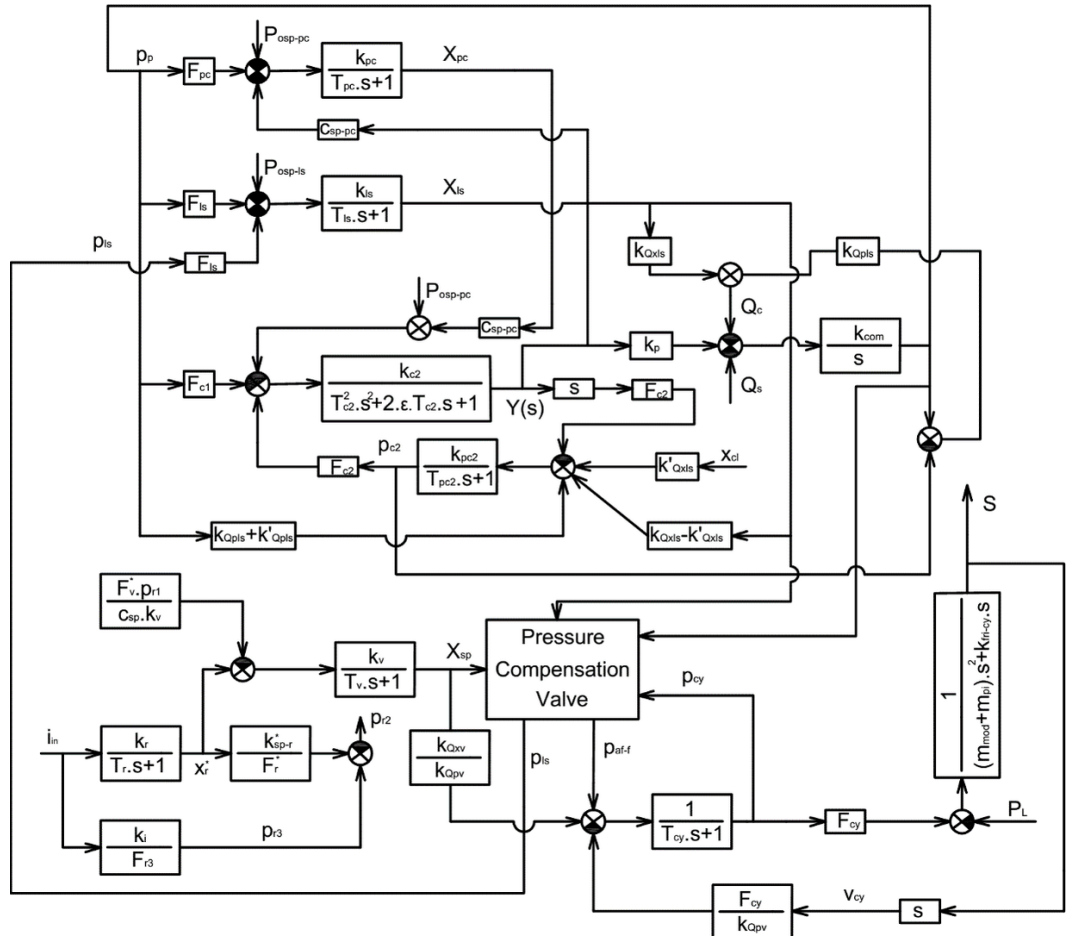
The process of calculating a very large volume to simplify the process of studying the dynamics properties when laying bomb is carried out by the laying method of the boom without moving the arm of the robot. Therefore, this method will ensure the accuracy of the bomb placement when the distance from the starting position to the laying surface of the bomb is small (for example, lowering the lifting cylinder 0.1 m). To study the dynamics characteristics during bomb laying using LMS Amesim software, components like pump control valves are designed from elements in the Hydraulic Component Design and Mechanical library. The remaining basic components are taken from the Hydraulic and Signal Control library. Some main parameters of the system are HPV 95 hydraulic pump: Specific flow 95 cc/rev, maximum working pressure  $p_{max} = 350$  bar; diameter of the PC, LS valves 10 mm, normally open mode; The pump uses mechanical feedback control.

Control pump: Gear pump, specific flow 36 cc / rev; Maximum working pressure is 30 bar. Main valve: 25 mm diameter of the spool. Proportional pressure reducing valve: diameter of main spool 10 mm, electrical control signal  $i_{max} = 800$  mA, maximum working pressure 50 bar.

Parameters of working cylinder: Diameter of cylinders  $D_1 = 105$  mm,  $D_2 = 115$  mm,  $D_3 = 95$  mm, diameter of rods  $d_1 = 70$  mm,  $d_2 = 75$  mm,  $d_3 = 65$  mm, stroke of cylinders  $l_1 = 990$  mm,  $l_2 = 1175$  mm,  $l_3 = 885$  mm. The initial displacements of the three cylinders – the boom, arm and excavation – gripper bomb mechanism were 0.818 m, 0.84 m, 0.71 m, respectively. Masses of working equipment:  $m_1 = 936$  kg,  $m_2 = 410$  kg,  $m_3 = 955$  kg.

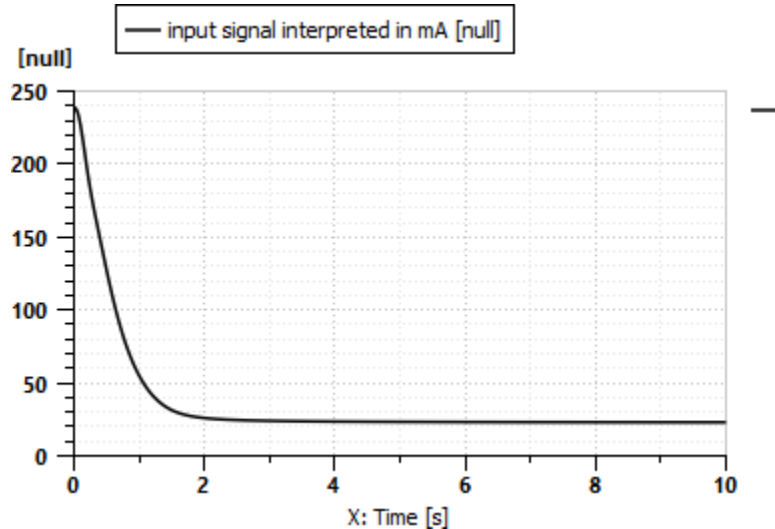
The change of force acting on the end of the rod in two directions x, y during the process of laying the bomb, with the largest bomb MK-84 having a weight of 907 kg is shown in Figure 6; and proportional pressure reducing valve control signal is shown in Figure 5. As shown in Figure 6, when the bomb is laid, the force acting on the rod of the lifting cylinder is constantly changed and only stabilized when the piston stops moving. According to Figure 8, the displacement of the piston has

Figure 4. Structure diagram of hydraulic system controlling working equipment



not reached the required value (from 0.818 to 0.718 m), this can be explained in Figure 7. Specifically, when the value of the pressure to control the main valve reaches the value of 1.5 bar at 3 s, with this pressure value, the opening of the main valve is close to zero and the piston of the boom does not move further. Therefore, the proportional pressure reducing valve control signal also stops at 20 mA.

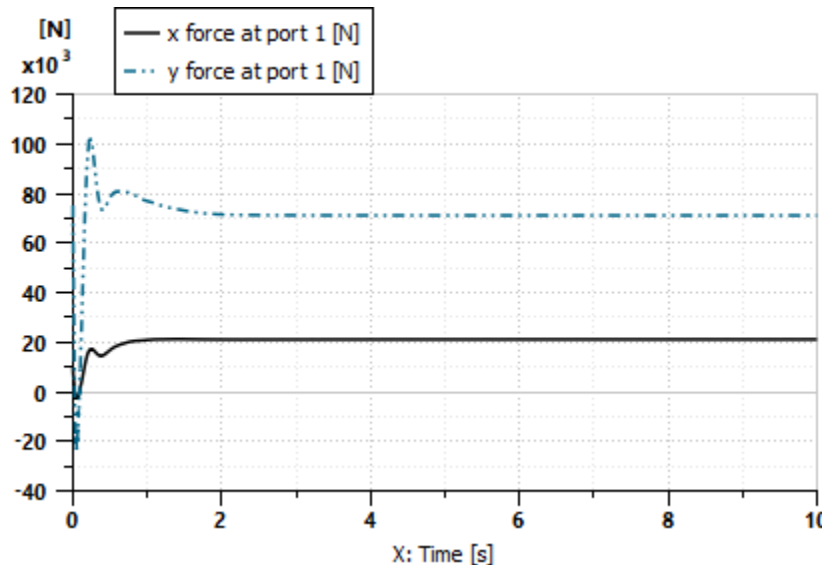
In order to achieve the displacement value, the laying velocity of the lifting cylinder needs a suitable proportional pressure relief valve control signal so that the valve control pressure is decreased to 4 bar to maintain the small opening of the main valve. When the necessary displacement is reached, this value immediately lowers to 1.5 bar (or control signal to 0 mA). According to Figure 9, with the displacement of 0.09 m in the direction of laying the boom piston, the displacement of the center gravity of the excavation – gripper bomb mechanism (together with the bomb) in the y direction is 0.85 m (from 0.15 m to -0.7 m). Meanwhile, the movement in the x direction is only 0.053 m (from 4.716 m to 4.663 m). As Figure 10 shows, when extending arm of 0.16 m, the displacement in the y direction of the center gravity decreases to 0.98 m (from 0.7 m to -0.28 m), while the movement in the x direction of the center gravity increases by 0.039 m (from 5.315 m to 5.354 m). Thus, the position deviation in the x direction has decreased to less than 0.05 m. Therefore, to properly place the bomb into the desired position, the remote operator needs to extend the arm as far as possible

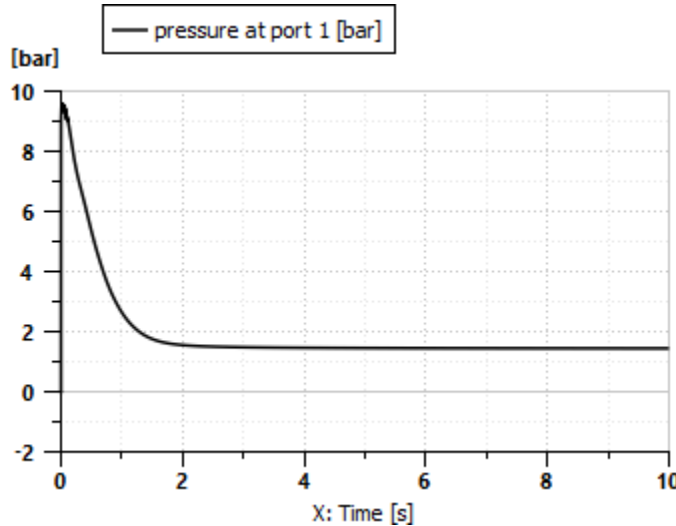
**Figure 5. Proportional pressure reducing valve control signal**

or if it is imperative to place the bomb near the base machine, coordination of the boom and arm is needed. However, the control of coordination of the boom and arm must be automated to ensure that the laying velocity value is set to 0 as shown in Figure 11.

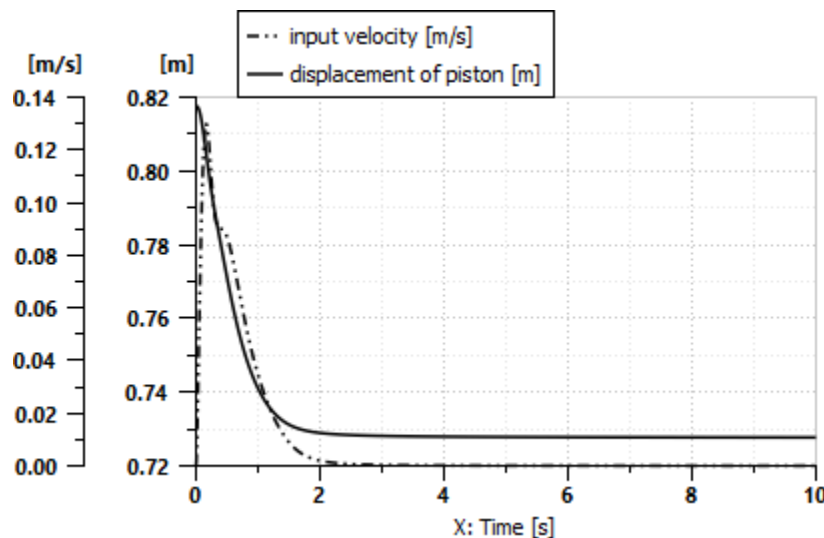
## 5. CONCLUSION

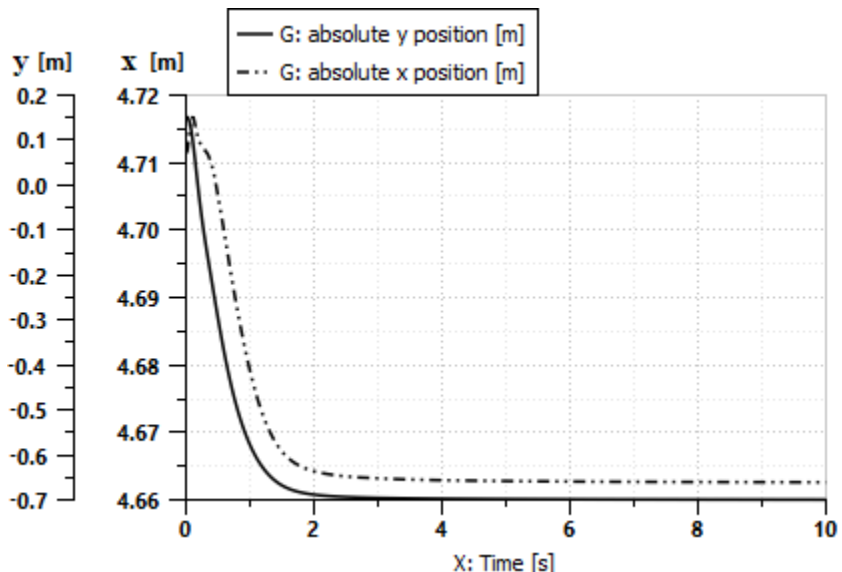
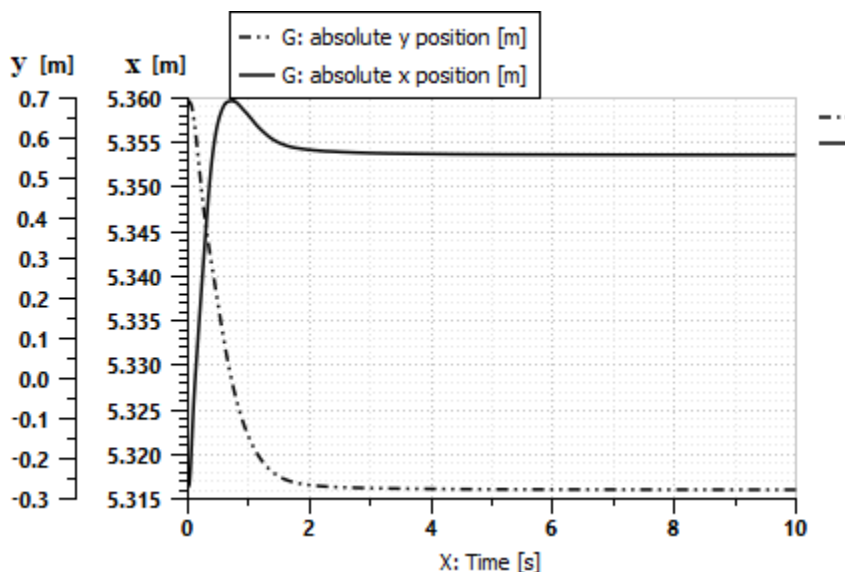
The paper has modeled the dynamics of working equipment with the hydraulic system on the remote-controlled explosive disposal machine from the LS-PC control pump using mechanical feedback to the control system which consists of a proportional pressure reducing valve and a main valve

**Figure 6. The change of force acting on the end of the rod – boom cylinder**

**Figure 7. Pressure to control the main valve**

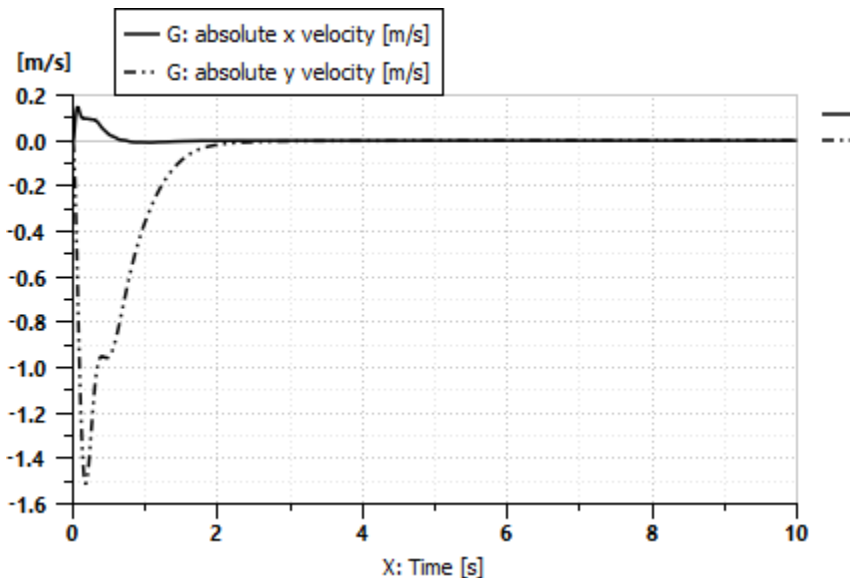
integrated with a pressure compensation valve. The model of operating working equipment during the bomb-laying process was fully built. LMS Amesim software is employed to simulate all hydraulic components, lifting equipment as well as input control signals to make dynamic assessments for the system. The bomb-laying process with high accuracy and safety shows important notes. Firstly, when laying the bomb near the base vehicle, just combine the lowering boom and the extending arm. When laying the bomb far away from the base vehicle (arm is extended), the method of boom laying (due to cameras for observation support) is adopted. Therefore, in practice, the application of the boom laying method will be simple and accurate. Secondly, it is necessary to ensure the proper bomb laying procedure satisfies the distance and velocity conditions and the control signal of the pressure reducing valve meets the requirements mentioned earlier to overcome the delay of the main

**Figure 8. Movement and speed of the bomb piston**

**Figure 9. Movement of center gravity of excavation – gripper bomb mechanism****Figure 10. Movement of the center gravity of the gripper bomb mechanism (when extending arm)**

valve and the pressure reducing valve. Based on the achieved results, the dynamic model of operating components and driving hydraulic system can be used for a future study which focuses on controlling exactly the depth of excavating operation which is an important task for the bomb laying process.

Figure 11. Speed of bomb laying



## REFERENCES

- Bedotti, A., Pastori, M., & Casoli, P. (2018). Modelling and energy comparison of system layouts for a hydraulic excavator. *Energy Procedia*, 148, 26–33. doi:10.1016/j.egypro.2018.08.015
- Bender, F. A., Göltz, S., Bräunl, T., & Sawodny, O. (2017). Modeling and Offset-Free Model Predictive Control of a Hydraulic Mini Excavator. *IEEE Transactions on Automation Science and Engineering*, 14(4), 1682–1694. doi:10.1109/TASE.2017.2700407
- Bender, F. A., Mitschke, M., Bräunl, T., & Sawodny, O. (2017). Predictive operator modeling for virtual prototyping of hydraulic excavators. *Automation in Construction*, 84, 133–145. doi:10.1016/j.autcon.2017.08.008
- Bradley, D. A., & Seward, D. W. (1998). The Development, Control and Operation of an Autonomous Robotic Excavator. *Journal of Intelligent & Robotic Systems*, 21(1), 73–97. doi:10.1023/A:1007932011161
- Burks, B. L., Killough, S. M., Thompson, D. H., & Dinkins, M. A. (1994). Explosive Ordnance Disposal Technology Demonstration Using the Telerobotic Small Emplacement Excavator. Oak Ridge National Laboratory.
- Casoli, P. & Riccò, L. (2013). Modeling and verification of an excavator system – Axial Piston Pump, Kinematics and Load Sensing Flow Sharing Valve Block. *Linköping Electronic Conference Proceedings*, 92(6), 53-63. doi:10.3384/ecp1392a6
- Casoli, P., Gambarotta, A., Pompini, N., & Riccò, L. (2016). Hybridization methodology based on DP algorithm for hydraulic mobile machinery—Application to a middle size excavator. *Automation in Construction*, 61, 42–57. doi:10.1016/j.autcon.2015.09.012
- Casoli, P., Riccò, L., Campanini, F., & Bedotti, A. (2016). Hydraulic Hybrid Excavator—Mathematical Model Validation and Energy Analysis. *Energies*, 9(12), 1002. doi:10.3390/en9121002
- Chai, Z., Nie, T., & Becker, J. (2020). *Top Ten Challenges Facing Autonomous Driving. In Autonomous Driving Changes the Future*. Springer.
- Chang, P. H., & Lee, S. J. (2002). A straight-line motion tracking control of hydraulic excavator system. *Mechatronics*, 12(1), 119–138. doi:10.1016/S0957-4158(01)00014-9
- Dat, N. D. (2017). Design and Manufacturing OEMD. Internal report, Institute of Military Engineering, Hanoi.
- Fleming, M. R. (2004). *Teleoperated Control of Hydraulic Equipment for Hazardous Material Handling* (Master thesis). Virginia Polytechnic Institute, Blacksburg, VA.
- Ge, L., Quan, L., Zhang, X., Zhao, B., & Yang, J. (2017). Efficiency improvement and evaluation of electric hydraulic excavator with speed and displacement variable pump. *Energy Conversion and Management*, 150, 62–71. doi:10.1016/j.enconman.2017.08.010
- Gimadiev, A.G. (2014). *LMS Imagine.lab Amesim as an effective tool for modeling dynamic processes in mechatronic systems*. Samara: Publishing House of Samts RAS.
- Gu, J., Ma, X., Ni, J., & Sun, L. (2012). Linear and nonlinear control of a robotic excavator. *Journal of Central South University*, 19(7), 1823–1831. doi:10.1007/s11771-012-1215-y
- Gurko, A. G. (2004). *Mathematical model of the excavator manipulator with a backhoe*. KHHADU.
- Ha, Q. P., Yen, L., & Balaguer, C. (2019). Robotic autonomous systems for earthmoving in military applications. *Automation in Construction*, 107, 102934. doi:10.1016/j.autcon.2019.102934
- He, Q., Zhang, D., Hao, P., & Zhang, H. (2006). Modeling and control of hydraulic excavator's arm. *Journal of Central South University*, 13(4), 422–427. doi:10.1007/s11771-006-0061-1
- He, X., & Jiang, Y. (2018). Review of hybrid electric systems for construction machinery. *Automation in Construction*, 92, 286–296. doi:10.1016/j.autcon.2018.04.005
- Lee, J., Kim, B., Sun, D., Han, C., & Dongik Ahn, J. (2019). Development of Unmanned Excavator Vehicle System for Performing Dangerous Construction Work. *Sensors Journal*, 19(22), 4853.

Liang, X., Wan, Y., Zhang, C., & Kou, Y. (2018). *Design of Position Feedback System with Data Fusion Technology for Large Hydraulic Manipulator*. In *Advances in Mechanical Design ICMD 2017, Mechanisms and Machine Science*, 55. Springer.

Man, Z., Ding, F., Ding, C., & Liu, S. (2015). Hydraulic Impulse-Testing System with Pressure Difference Feedback from a Second-Stage Valve. *Journal of Aerospace Engineering*, 28(6), 04015004. doi:10.1061/(ASCE)AS.1943-5525.0000492

Manz, D. (2001). *Remotely controlled ordnance clearing operation ordnance remediation report*. AFRL. doi:10.21236/ADA526561

Park, S. H., Alam, K., Jeong, Y. M., Lee, C. D., & Yang, S. Y. (2009). Modeling and Simulation of Hydraulic System for a Wheel Loader using AMESim. *ICROS-SICE International Joint Conference 2009*, 2991-2997.

Rogers, W. P., Kahraman, M. M., Drews, F. A., Powell, K., Haight, J. M., Wang, Y., Baxla, K., & Sobalkar, M. (2019). Automation in the Mining Industry: Review of Technology, Systems, Human Factors, and Political Risk. *Mining, Metallurgy & Exploration*, 36(4), 607–631. doi:10.1007/s42461-019-0094-2

Saputra, H. M., & Mirdanies, M. (2015). Controlling unmanned ground vehicle via 4 channel remote control. *Energy Procedia*, 68, 381–388. doi:10.1016/j.egypro.2015.03.269

Sprengel, M. M., & Ivantysynova, M. (2013). Investigation and energetic analysis of a novel hydraulic hybrid architecture for on-road vehicles. *The 13th Scandinavian International Conference on Fluid Power, SICFP2013*, 3-5.

Terwelp, C. R. (2003) *Remote Control of Hydraulic Equipment for Unexploded Ordnance Remediation* (Master Thesis). Virginia Polytechnic Institute, Blacksburg, VA.

Vähä, P., Heikkilä, T., Kilpeläinen, P., Järvi vuoma, M., & Gambao, E. (2013). Extending automation of building construction—Survey on potential sensor technologies and robotic applications. *Automation in Construction*, 36, 168–178. doi:10.1016/j.autcon.2013.08.002

Vaseliu, N. (2018). Simulation of fluid power systems with Simcenter Amesim. Siemens.

Vujic, D., Lazarevic, O., & Batinic, V. (2017). Development of dynamic-mathematical model of hydraulic excavator. *Journal of Central South University*, 24(9), 2010–2018. doi:10.1007/s11771-017-3610-x

Wang, H. B., Zou, H. L., & Zhang, R. Z. (2014). A novel approach to detect the posture of excavator's manipulator. *Appl Mech Mat. Trans Tech Publications*, 668, 891–8.

Wei, C. M., Lian, J. Y., & Li, J. J. (2011). The Modeling Analysis and Dynamics Simulation of Load-Sensing Hydraulic Systems. *Advanced Materials Research*, 317–319, 307–313. doi:10.4028/www.scientific.net/AMR.317-319.307

Yamamoto, H., Moteki, M., & Shao, H. (2010). Development of the autonomous hydraulic excavator prototype using 3-D information for motion planning and control. System integration (SII), IEEE/SICE international symposium on IEEE, 49–54.

Yang, Y., & Chen, Q. L. (2013). Modeling and Analysis of Full Hydraulic Pressure Drive System of the Wheel Loader Based on AMEsim. *Applied Mechanics and Materials*, 397–400, 261–265. doi:10.4028/www.scientific.net/AMM.397-400.261

Yoshinada, H. (2019). Dual-Arm Construction Robot with Remote-Control Function. *Disaster Robotics. Springer Tracts in Advanced Robotics*, 128, 195-264. doi:10.1007/978-3-030-05321-5\_5

Yuki S. & Yoshiaki K. & Kenichirou S. (2014). *Development of PC210LCi-10/PC200i-10 Machine Control Hydraulic Excavator*. Komatsu Technical Report.

Yusof, A. A., Saadun, M. N. A., Mohamed Nor, M. K., Ibrahim, M. Q., & Abdul Manaf, M. Z. (2015). Position Control Mathematical Modelling and Operational Evaluation of Tele-Operated Electro-Hydraulic Actuator (T-EHA). *Applied Mechanics and Materials*, 773–774, 163–167. doi:10.4028/www.scientific.net/AMM.773-774.163

**International Journal of Manufacturing, Materials, and Mechanical Engineering**  
Volume 11 • Issue 3 • July-September 2021

Yusof, A. A., Saadun, M. N. A., Sulaiman, H., & Sabaruddin, S. A. (2016). The development of tele-operated electro-hydraulic actuator (T-EHA) for mini excavator tele-operation. *2nd IEEE International Symposium on Robotics and Manufacturing Automation (ROMA)*, 1-6. doi:10.1109/ROMA.2016.7847800

*Nguyen Duy Dat was born in Vietnam in January 1987. He graduated from Le Quy Don University of Technology, Vietnam in 2008. He received M.S. degree in hydraulic machinery, hydraulic transmission, and pneumatic hydraulic automation from Bauman University, Russian Federation in 2012. He is interested in dynamics and hydraulic control, dynamics and construction machine structures.*

*Chu Van Dat was born in Vietnam in March 1962. He received his B.S. degree in Mechanical Engineering from Kaliningrat University of Technology, Russia in 1986. He received M.S. degree in Automotive and Mechanical Engineering from Hanoi University of science and technology, Vietnam in 1991. And then he received PhD degree in Automotive and Mechanical Engineering from Le Quy Don technical University, Vietnam in 2001. He is interested in kinetic and dynamic simulation, hydraulic simulation, finite element simulation, machine structure optimization.*

*Le Van Sy was born in Vietnam in July 1979. He received his B.S. degree in Mechanical Engineering from Ho Chi Minh City University of Technology, Vietnam in 2003. He received M.S. degree in Automotive and Mechanical Engineering from Ulsan University, Korea in 2007. And then he received PhD degree in Industrial system and Manufacturing from University of Padua, Italy in 2010. He is interested in CAD/CAM/CNC, die-less sheet metal forming, finite element simulation, offshore engineering.*

# Classification and Automatic Feature-Based Extraction Approach for Cylindrical and Milling Parts

Sathish Kumar Adapa, Aditya Institute of Technology and Management, India

Dowluru Sreeramu, Aditya Institute of Technology and Management, India

Jagadish, National Institute of Technology, Raipur, India

## ABSTRACT

This paper reports classification and automatic extraction of various cylindrical and milling features in conventional machining process parts. In this work, various algorithms like hole recognition algorithm (HRA) and milling feature recognition algorithm (MFRA) have been used for identification of different cylindrical and milling features. A cylindrical feature is identified based on specific logical rules, and milling feature is identified based on the concept of concave decomposition of edges. In-house developed JAVA program is used to write algorithm, and then validation of the algorithm is done through two case studies. The HRA and MFRA algorithms extract the cylindrical features (through holes, blind holes, taper holes, and bosses) and milling features (slot, blind slot, step, blind step, pockets) precisely. The current work is well suitable to extract the features in conventional machining parts and thereby improve the downstream applications like process planning, CAPP, CAM, etc.

## KEYWORDS

CAD, CAM, Face, Feature Extraction, HRA, MFRA

## INTRODUCTION

The evolution of Computer aided design (CAD) and computer aided manufacturing (CAM) systems is being done by the several researchers over the recent past decades for the low cost and high production. The conventional design and manufacturing activities would be optimized for the rise of productivity through the “integration of CAD/CAM technologies”. Computer aided process planning (CAPP) is being the communication agent between CAD and CAM, to achieve the required product. CAD files mainly consist of geometrical information of the product. The CAPP is aimed to generate the sequence of instructions used to manufacture the required product by using specified CAD data (Yusof & Latif, 2014). However, CAPP also plays a major role in integrating CAD and CAM. A successful integration of CAD and CAM is done through the automatic extraction of manufacturing product information from the CAD systems. This automatic extraction can be treated as a basic step to automate the product development from the design stage, thereafter, manufacturing and shipping stages (Yusof & Latif, 2014; Hoffmann & Joan, 1998; Gindy, 1989). Automatic feature recognition (AFR) system is also an essential tool for successful integration of design and manufacturing stages during the product development. The automatic feature recognition techniques used to identify and extract the design and manufacturing features from part models.

DOI: 10.4018/IJMMME.2021070104

Copyright © 2021, IGI Global. Copying or distributing in print or electronic forms without written permission of IGI Global is prohibited.

The rest of the paper is organized as follows; section-2 reports previous related works in the area of feature identification and extraction. Section-3 explains the definition and classification of cylindrical and milling features. The methodology for extracting cylindrical and milling features is presented in section 4. Section 5 shows system integration and implementation of algorithms through case studies and analysis of results. Sections 6 present the conclusions drawn from the work.

## **Previous Work**

The word “feature” is actually a misnomer, because the term “feature” has different meaning with respect to the situation. The “concentration focused on a particular portion on the surface of a part” is treated as feature in this study (Hoffmann & Joan, 1998). Certainly, the idea is to represent the geometry of a portion on the surface of a part as a feature. Subsequently, the feature has also been classified based on the application viz., milling and cylindrical as well as the desired geometrical shape (Case & Wan, 2000; Ciurana et al., 2003; Kumar et al., 2003). The researchers have been consistently adding the different techniques and algorithms to the literature to extract the design and manufacturing features from solid part model. Features like protrusions and depression extracted from boundary representation in to its bi-connected components by using graph based theory (Gavankar & Henderson, 1990). The intersecting features and auxiliary features in perceptive to fillets are extracted from prismatic parts by using graph based technique (Senthil Kumar et al., 1996). The extraction of rough manufacturing features in 2.5D components (Xu & Hinduja, 1998) were done through physical states of equilibrium and concavity approaches. In a hybrid approach (combination of graph-based approach and volume – based approach) to extract orthogonal and non – orthogonal features from CAD part models (Wong & Lam, 2000). A simple theory of light rays travels in a straight line, and specific rules are used to extract manufacturing features of the solid models (Ranjan et al., 2005). The application of edge boundary classification (EBC) technique for recognizing simple and interacting cylindrical based features (Ismail et al., 2005). The hole recognition system (HRS) to extract form features by using Rule-based technique (Tan et al., 2007). Different characteristics of each feature such as total number of faces, edges and attributes of features are identified by using the rule based technique (Abu & Tap, 2007). Design and manufacturing features are recognized by using volume decomposition method, and also determine the removal volumes, access direction and raw material geometry of the features (Nagarajan & Reddy, 2010). A novel algorithm to extract turning features, further integrate with STEP-NC file, provides as a logical integration approach of CAD/CAPP/CAM (Sreeramulu & Rao, 2012). Cylindrical features are identified by using rule-based technique, and integrated CAD, CAM and CAI (Siva Kumar & Dhanalaxmi, 2013). The machining features viz., holes, blind holes are extracted by using rule based technique (Tan et al., 2013). The user defined assembly features viz., holes and slots are extracted by using an algorithm and taking STEP as an input file (Vemulapalli et al., 2014). Viswa & Manish (2014) proposed an intelligent system to extract prismatic part features by using feature based modeling system. The milling feature (i.e. through slot) is extracted by using an algorithm and taking STEP AP-224 as an input file (Ashok et al., 2016). Geometric and parametric features in prismatic parts are extracted by using hybrid approach (Hint based approach and volume decomposition approach (Sangolli & Pilli, 2017). Symmetrical and non-symmetrical features are extracted from cylindrical parts by using volume decomposition technique (Zubair & Abu Mansor, 2018). A novel approach to extract interacting and compound volumetric features of prismatic part and to automate material removal for the extracted volumetric features (Kataraki et al., 2019). In a novel and smart interactive feature recognition system, the square groove features are extracted from rotational parts by using AFR rule based technique (Al-wswasi & Ivanov, 2019). Spot welding features like number of spot welds, diameters and weld plane are identified by using rule-based technique (Muhammad & Hasan, 2019). Peizhishi et al., (2020) developed a novel algorithm to extract features and surfaces of 3D CAD models by using rule-based technique and integrated CAD and CAPP. Juan et al., (2020) developed novel algorithm to extract prismatic features and curved edges and faces of 3D CAD model STEP files.

After going through a comprehensive literature study, it is observed that the cylindrical features such as taper holes, blind holes, cylindrical bosses, taper protrusions, blind step, blind slot and blind pockets have not been much investigated. Therefore the current work aims to identify the different cylindrical and milling features using HRA and MFRA. A cylindrical feature is identified based on specific logical rules and milling feature is identified based on the concept of concave decomposition of edges. A JAVA plat form is used to write algorithm and then validation of the algorithm is done through two case studies.

## CLASSIFICATION OF FEATURES

A solid model part can be machining into a variety of shapes. A solid model part is a combination of various features and each feature is having number of faces which are related to other faces directly or indirectly. Conventional machining features are classified into the following two categories.

### Cylindrical Features

Cylindrical features as a result of removal of the material from the solid work piece/model. These features are obtaining drilling and boring operations. Some of the examples of cylindrical features are holes, taper holes, blind holes, cylindrical bosses, taper protrusions. Some of these cylindrical features are illustrated in Figure 1. The cylindrical features are classified and represented in terms of circles, cylinders, planes and adjacency relationship between them. Drilling or boring operation on a solid work piece/ model creates circles and cylindrical surfaces on a plane with respect to solid model part. The characteristic arrangement of these circles, cylindrical surfaces on the plane refer to basic cylindrical feature.

### Milling Features

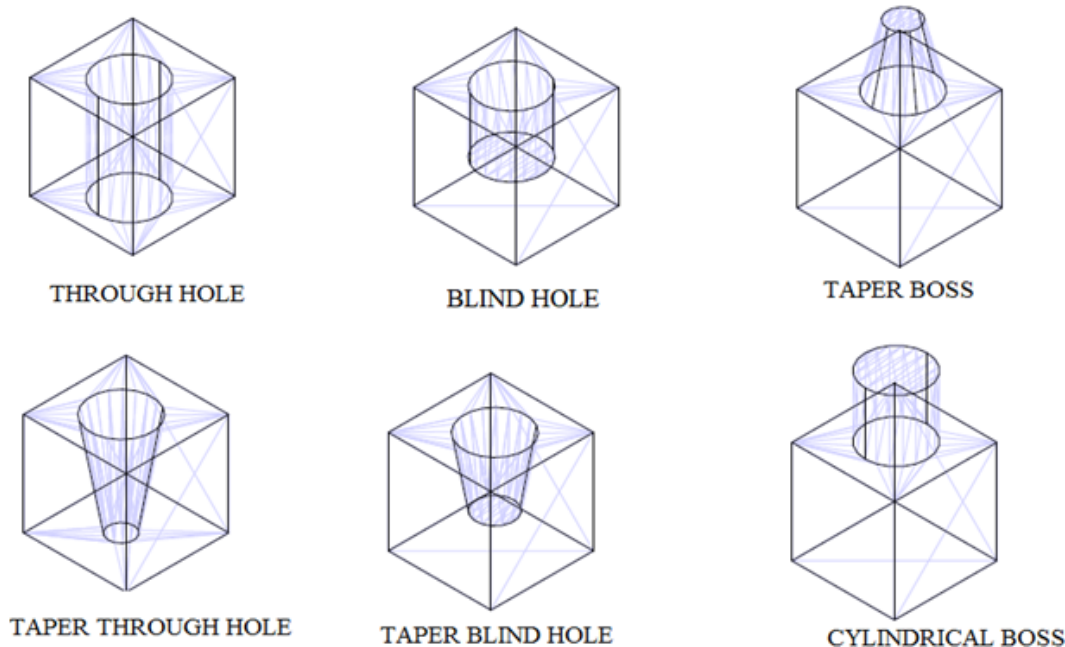
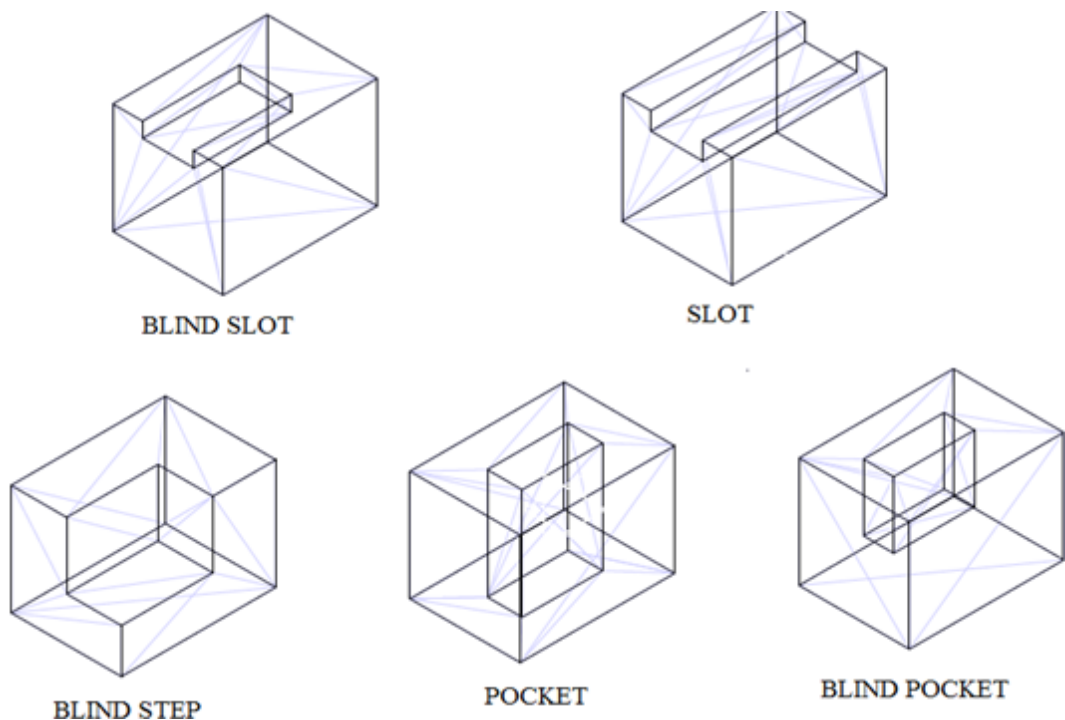
Milling features are present in a solid part model, as a result of cutting and removal of the material from the solid work piece/model. These milling features are obtaining planar and shaping operations. Some of the milling features are slot, through slot, pocket, step, blind step. The milling features are classified and represented in terms of faces, edges, planes and vertex points and adjacency relationship between them. Planar or shaping operation on a solid work piece/ model creates faces and edges on a plane with respect to solid model part. The characteristic arrangement of these faces, edges, and vertex points, normal on the plane refer to basic milling feature. Some of these milling features as illustrated in Figure 2.

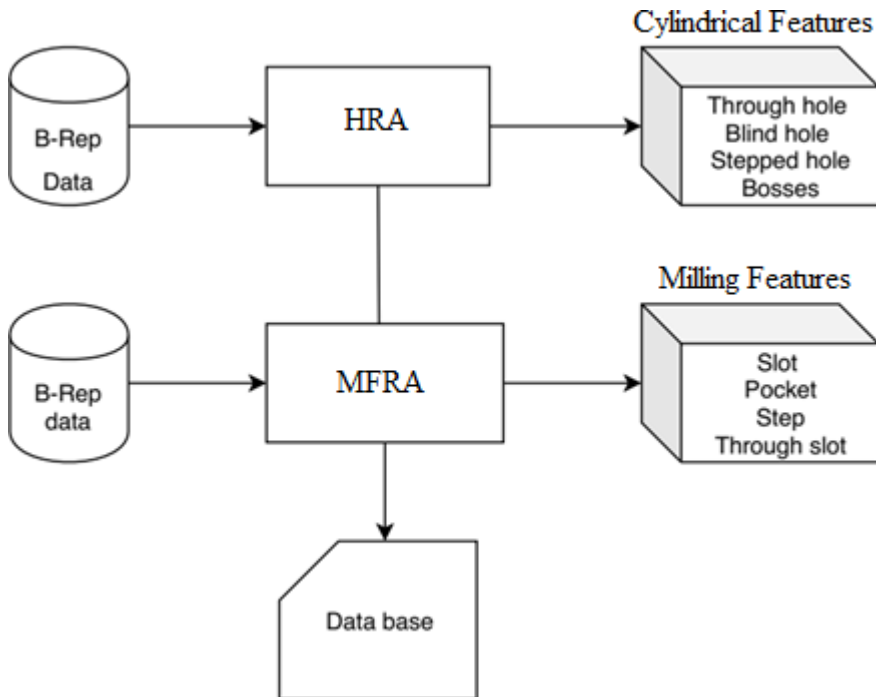
## METHODOLOGY

A solid part model is designed through CAD software. The solid part model is transformed in to a neutral format called STEP file, which interfaces the different CAD/CAM systems. The STEP file is converted in to B-Rep model which further used as an input to the algorithm. In this paper two algorithms HRA and MFRA have been used for classification and extraction of cylindrical features and milling features as shown in Figure 3. The cylindrical features like through holes, taper holes, blind holes, taper bosses, cylindrical protrusions and milling features like slot, blind slot, step, blind step, pockets have been extracted.

### Recognition of Cylindrical Features Through HRA Algorithm

The HRA (Hole recognition algorithm) used for recognizing cylindrical/taper features. The cylindrical features like through holes, taper holes, blind holes, cylindrical bosses extracted is primarily based on the rule-based approach. Where rules are specified with OR and IF Conditions. Condition is

**International Journal of Manufacturing, Materials, and Mechanical Engineering**  
Volume 11 • Issue 3 • July-September 2021**Figure 1. Cylindrical features****Figure 2. Milling features**

**Figure 3. Methodology for extracting cylindrical and milling features**

composed by a set of tests on object attributes linked by logic operator (AND, OR). The algorithm for identifying those features is shown in Figure 4.

The extraction of cylindrical features from a STEP-214 file of a part model is discussed in the following steps:

**Step 1:** STEP AP-214 file of the part is read to extract the B-rep data: After deep analysis of the STEP AP-214 file has been made and developed GDE algorithm (Sreeramulu & Rao, 2008) to extract the geometrical details of the part (B-rep data) from the STEP AP-214 file.

**Step 2:** Find cylinders and planes of the part model: The B-rep data obtained from GDE algorithm, to read the details of cylinders and planes of the part model.

**Step 3:** Extract circles from planes and cylinders: The details of cylinders and planes of the part model is obtained, the attributes of the circles from planes  $C(p)$  and cylinders  $C(cy)$  has been read and stored in the data base.

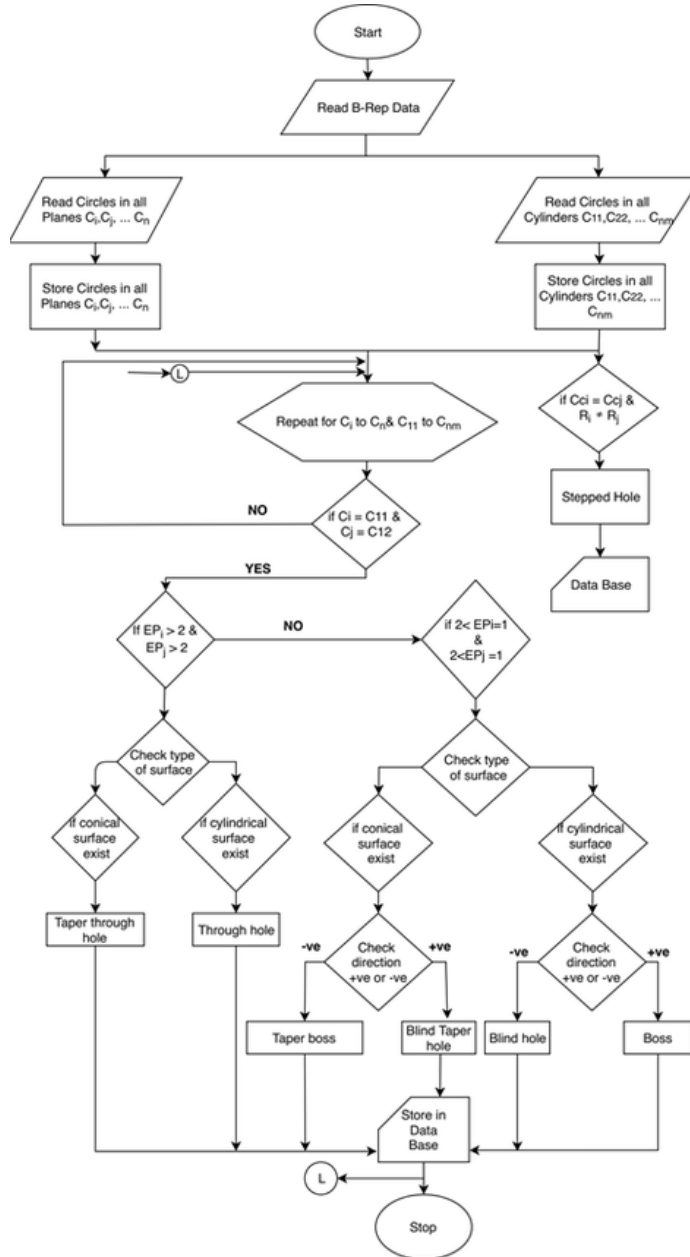
**Step 4:** Classify attributes of the cylindrical surfaces: The cylindrical surfaces are recognized and stored in the data base:

1. Upper circle of the cylinder is  $C_U(cy)$ ;
2. Lower circle of the cylinder is  $C_L(cy)$ .

**Step 5:** Matching of circles, cylinders and planes: The circle details of cylinders and planes are matching the following steps are to find the feature type of the part model:

1. Check if lower circle details of the cylinder are equal to circle details of plane;
2. Check if upper circle details of the cylinder is equal to circle details of the plane;
3. Find the number of edges in plane;
4. Check if the number of edges in plane and plane is greater than two i.e.  $E(P_i) > 2$ ,  $E(P_j) > 2$ ;
5. Check if the conical surface is exists the corresponding hole is assign, Taper hole (or) else if cylindrical surface is exists the corresponding hole is said to be Through hole;

Figure 4. Flow chart for extraction of hole features from B-Rep of a solid model part



6. Check if the number of edges in plane and plane greater than two and other plane equals to two i.e.  $E(P_i) > 2$  and  $E(P_j) = 2$  (OR)  $E(P_i) = 2$  and  $E(P_j) > 2$ ;
7. Check if the conical surface exists, and the direction is positive then the corresponding feature is assign to Blind taper hole, or else the direction is negative then the corresponding feature is assign to Taper boss;

8. Check if the cylindrical surface exists, and the direction is positive then the corresponding feature is assign to Blind hole, or else the direction is negative then the corresponding feature is assign to cylindrical boss;
9. Check if two cylindrical circles having same center point and different radius i.e.  $C_{ci} = C_{cj}$  and  $R_i \neq R_j$  then the corresponding feature is assigned to Stepped hole and store the data in data base.

## Recognition of Milling Features Through MFRA Algorithm

The MFRA (Milling feature recognition algorithm) has been developed for extraction of milling features. The milling features like slots, blind slots, steps, pockets, blind pockets extracted are primarily based on the convexity principle of concave decomposition of edges. The root faces of a form-feature are extracted by decomposing the object, at concave edges is the basic principle of the proposed heuristics. The present approach explored that a face whose all neighboring faces are at convex angle does not form part of a feature, and the boundary faces of the feature also recognized as well as root faces. Once the boundary and root faces associated with each feature on the object are identified. Algorithm has been developed to extract milling features are shown in Figure 5. The extraction of milling features from a STEP-214 file of a part model is discussed in the following steps:

**Step 1:** STEP AP-214 file of the part is read to extract the B-rep data: After deep analysis of the STEP AP-214 file has been made to develop GDE algorithm (Sreeramulu & Rao, 2018) to extract the geometrical information of the part (B-rep data) from the STEP AP-214 file.

**Step 2:** Find faces and planes of the part model: The B-rep data obtained from geometric data extraction algorithm to read the details of faces and planes of the part model.

**Step 3:** Extract edges, normal and vertex points from planes and faces: The details of face and planes of the part model is obtained, the attributes of the edges, normal and vertex points from the planes has been read and stored in the data base.

**Step 4:** Classify attributes of the root faces (R): The root faces are identified and stored in the data base:

1. Adjacent root face is  $R_{adj}$ ;
2. Parallel root face is  $R_{par}$ ;
3. Perpendicular root face is  $R_{per}$ .

**Step 5:** Matching of plane edges and calculate convexity index(C) value of faces and planes: The following steps are to find the feature type of the part model:

1. Check if face is equal to plane than go to next step otherwise go to step2;
2. Store vertex points of all edges and find the common edges and extract normal and direction of the plane;
3. Find the starting point ( $P_r$ ) and ending point ( $P_s$ ) of the plane edge;
4. If the  $i^{th}$  plane edge is equal to  $j^{th}$  plane edge then go to next step otherwise go to Step3;
5. Find  $C$  is equal to  $((P_s - P_r) \cdot (n_i \times n_j))$ ;
6. If the  $C$  value is greater than zero than the corresponding face is concave otherwise convex;
7. Read and store the concave faces  $f_1, f_2, f_3 \dots f_n$ ;
8. If  $((f_i \cup f_j) \cup (R_{per} \cup R_{adj}))$ ,  $R_{per}(f_i, f_j)$  &  $R_{adj}(f_i, f_j)$ . Then the corresponding feature is step otherwise go to next step;
9. If  $((f_i \cup f_j \cup f_k) \cup (R_{per} \cup R_{adj}))$ ,  $R_{per}(f_i, f_j), R_{per}(f_i, f_k), R_{per}(f_j, f_k), R_{adj}(f_i, f_j, f_k)$  then the Corresponding feature is Blind step;
10. If  $((f_i \cup f_j \cup f_k) \cup (R_{per} \cup R_{par} \cup R_{adj}))$ ,  $R_{per}(f_i, f_j), R_{per}(f_i, f_k), R_{par}(f_i, f_k), R_{adj}(f_i, f_j) (f_j, f_k)$  then the corresponding feature is Through slot. Otherwise go to next step;
11. If  $((f_i \cup f_j \cup f_k \cup f_l) \cup (R_{per} \cup R_{par} \cup R_{adj}))$ ,  $R_{per}(f_i, f_j), (f_i, f_l), (f_i, f_k), (f_k, f_l), R_{par}(f_i, f_k), R_{adj}(f_i, f_j, f_l), (f_k, f_j, f_l)$  then the corresponding feature is Blind slot. Otherwise go to next step;

12. If  $((f_i \cup f_j \cup f_k \cup f_l \cup f_m) \cup R_{per} \cup R_{par} \cup R_{adj}))$ ,  $R_{per}(f_i, f_j)$ ,  $(f_i, f_l)$ ,  $(f_i, f_k)$ ,  $(f_i, f_m)$ ,  $(f_j, f_k)$ ,  $(f_j, f_m)$ ,  $(f_k, f_l)$ ,  $(f_k, f_m)$ ,  $R_{par}(f_i, f_k)$ ,  $(f_j, f_l)$ ,  $R_{adj}(f_i, f_j, f_l)$ ,  $(f_k, f_j, f_l)$ , then the corresponding feature is pocket.

Recognition of features in prismatic parts is a tedious task when compared to rotational parts. The methodology proposed for recognizing features in prismatic parts has several advantages over other methods suggested in the literature using different data exchange standards. Most of the researchers who developed approaches are limited to identify blind and through holes. The proposed algorithms can recognize both cylindrical and milling features and these algorithms can be implemented together using a single java program for a model having arbitrary features.

## SYSTEM INTEGRATION AND IMPLEMENTATION OF ALGORITHM

In this paper used two algorithms to extract cylindrical and milling features (HRA and MFRA). For implement these two algorithms, which require input data in B-rep model. However B-rep model integrates the CAD STEP file model and algorithm. The B-rep model generally contains 31 regions. The details of B-rep regions of the STEP CAD model as tabulated in the Table 1.

### Case Study I

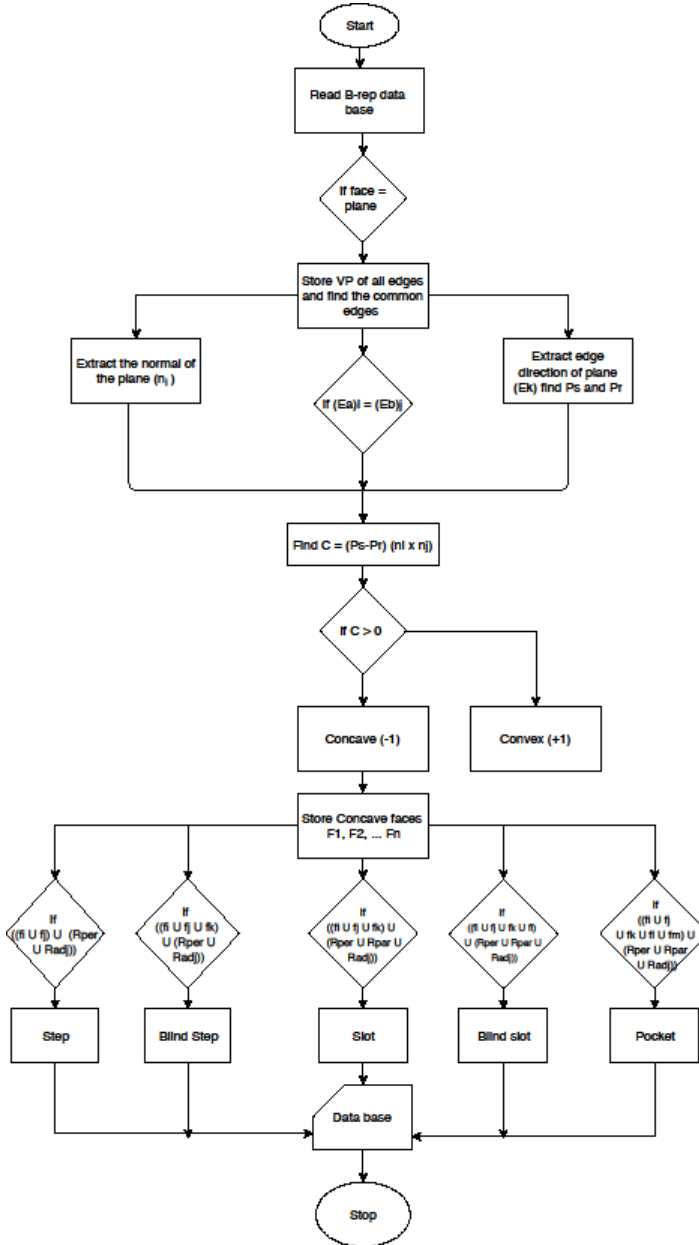
In order to implementation of HRA for cylindrical features, a solid part model is designed through CAD software as shown in Figure 6. The solid part model is transformed in to a neutral file called STEP file that interfaces the various CAD/CAM systems. The STEP file format is converted into B-rep model which is further used as a input to the HRA (Hole recognition algorithm) as shown in Figure 4 to extract the cylindrical features. The example No.1 consists of 7 number of cylindrical features like taper holes, through hole, blind hole, cylindrical boss, and taper boss. The output of HRA for cylindrical features as shown in Figure 7.

### Discussion of HRA Results

In B-rep data base cylindrical feature mainly consists of two cylindrical surfaces, center point and radius. In general hole feature contains two circles and connected by vertices. Further each circle having two circular edge segments and the circular edges of each hole is represented by their radius and center points. If the details of cylindrical, conical, toroid surfaces and plane surfaces are matching each other, then the corresponding cylindrical feature can be recognized. The required cylindrical features can be extracted based on the following conditions:

- Blind hole is formed between two cylindrical surfaces 21, 22 having same center point and radius. One circle of the cylinder subtracted from the adjacent plane and having more than two edges. Other side circle of the cylinder is adjacent and perpendicular to cylindrical surface, and having only two edges. The corresponding feature details tabulated in Table 1.
- Through hole is obtained based on the two cylindrical surfaces 10, 11 having same center point and radius. The top and bottom circles of the cylinder are subtracted from the adjacent plane and having more than two edges, and also adjacent to the cylindrical surface. The corresponding feature face numbers, radius and location as tabulated in Table 1.
- Taper through hole is identified between the two conical surfaces 16, 17 having same center point and different radius. The upper and bottom circles of the conical cylinder are subtracted from the adjacent plane and having more than two edges and also adjacent to the conical surface. The corresponding feature details are mentioned in Table 1.
- Cylindrical boss is obtained based on the two cylindrical surfaces 24, 25 having same center point and radius. One of the circles from the cylinder is adjacent to the cylindrical surface and having only two edges. Other end circle of the cylinder adjacent to the cylindrical surface and

Figure 5. Flow chart for extraction of milling features from B-Rep of a solid model part



having more than two edges. Based on the direction vector, can be identified either cylindrical boss or blind hole. The details of the cylindrical boss feature are tabulated in Table 2.

- Taper blind hole is recognized between two conical surfaces 30, 31 having same center point and radius is different. One of the circles from the conical cylinder is subtracted from the adjacent plane and having more than two edges. Other side circle of the conical cylinder adjacent to the conical surface and only having two edges. The corresponding feature details are represented in Table 2.

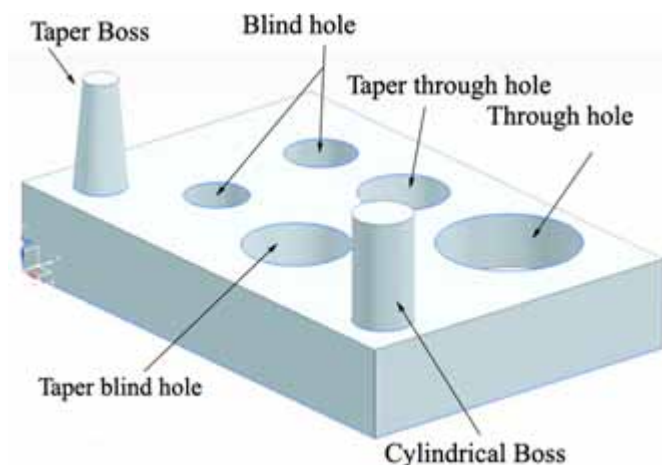
**International Journal of Manufacturing, Materials, and Mechanical Engineering**  
 Volume 11 • Issue 3 • July-September 2021

**Table 1. Details of B-Rep database**

S.No	Region	Entity
1	<b>1</b>	Face number
2	<b>2</b>	Edge number
3	<b>3,4,5</b>	Starting Cartesian point or Starting point of the edge curve.
4	<b>6,7,8</b>	Ending Cartesian point or Ending point of the edge curve.
5	<b>9</b>	Kind of edge namely line or circle.
6	<b>10</b>	Magnitude or radius of the corresponding edge.
7	<b>11,12,13</b>	Starting point of the corresponding edge or Center point
8	<b>14,15,16</b>	Corresponding edge direction-1.
9	<b>17,18,19</b>	Corresponding edge direction-2. (There is no second direction, if the type of edge is line.).
10	<b>20</b>	Nature of the face i.e. TOROIDAL_SURFACE Or CYLINDRICAL_SURFACE Or CONICAL_SURFACE.
11	<b>21</b>	Radius of the corresponding face.
12	<b>22</b>	Radius of the TOROUS or CONICAL_SURFACE Semi Cone angle. If the CYLINDRICAL_SURFACE is exists, it is ZERO.
13	<b>23,24,25</b>	Center point of corresponding face.
14	<b>26,27,28</b>	Direction-1 of corresponding face.
15	<b>29,30,31</b>	Direction-2 of corresponding face.

The proposed HRA can capable to identify some special features like through holes, blind holes, stepped holes and protrusions with their attributes like center of the hole, diameter of the hole which cannot be done in the other methodologies.

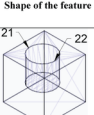
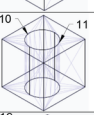
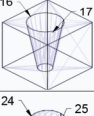
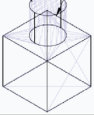
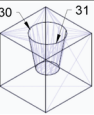
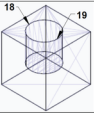
**Figure 6. Example 1(cylindrical features**



**Figure 7. Output of HRA for cylindrical features**

Mark Command Prompt					
Feature Name	Face Numbers	Radius	Location		
Blind Hole	21,22	5.0	<60.0,50.0,25.0>,<60.0,50.0,10.0>		
Through Hole	10,11	10.0	<30.0,80.0,25.0>,<30.0,80.0,0.0>		
Tapper Through Hole	16,17	10.0	<160.0,20.0,25.0>,<160.0,20.0,0.0>		
Cylindrical Boss	24,25	5.0	<140.0,50.0,25.0>,<140.0,50.0,10.0>		
Tapper Blind Hole	30,31	5.0	<20.0,50.0,25.0>,<20.0,50.0,10.0>		
Blind Hole	18,19	5.0	<180.0,50.0,25.0>,<180.0,50.0,10.0>		

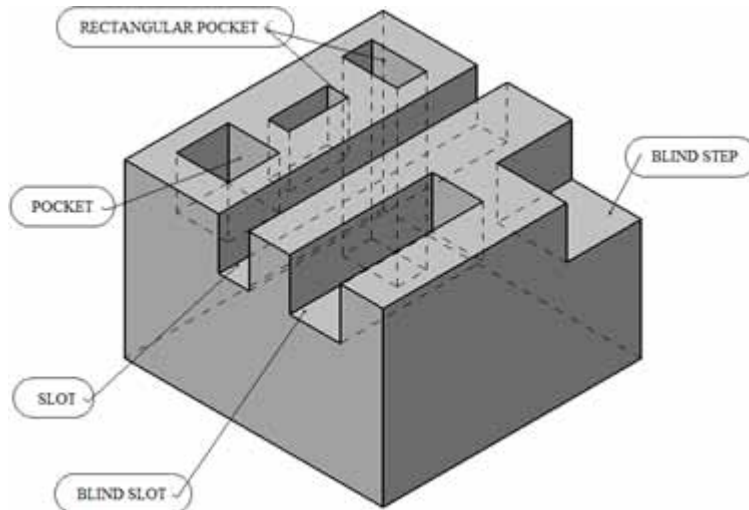
**Table 2. List of identified cylindrical features**

S.No	Feature Name	Face numbers	Radius	Location	Shape of the feature
1	Blind hole	21,22	5.0	(60.0,50.0,25.0),(60.0,50.0,10.0)	
2	Through hole	10,11	10.0	(30.0,80.0,25.0),(30.0,80.0,0.0)	
3	Tapper Through hole	16,17	10.0	(160.0,20.0,25.0),(160.0,20.0,0.0)	
4	Cylindrical Boss	24,25	5.0	(140.0,50.0,25.0),(140.0,50.0,10.0)	
5	Tapper Blind hole	30,31	5.0	(20.0,50.0,25.0),(20.0,50.0,10.0)	
6	Blind hole	18,19	5.0	(180.0,50.0,25.0),(180.0,50.0,10.0)	

## Case Study II

In order to implementation of MFRA (Milling feature recognition algorithm) for milling features, a solid part model is designed through CAD software as shown in Figure 8. The solid part model is transformed in to a neutral file called STEP file that interfaces the various CAD/CAM systems. The STEP file format is converted into B-rep model which is further used as an input to the MFRA as shown in Figure 5 to extract the milling features. The example No.2 consists of 6 number of milling features like slot, blind slot, blind step, through pocket, blind pockets. The output of MFRA for milling features as shown in Figure 9.

**Figure 8. Example 2 (Milling Feature Block)**



### Discussion of MFRA Results

In B-rep data base milling feature details consists of planes, lines and normal of the faces. Milling features are recognized based on the convexity and concavity relation among the faces. Convex faces which are represented by a concave edge ( $180^\circ < \Theta^0 < 360^\circ$ ) that joins two adjacent faces. Similarly convex faces which are represented by a convex edge ( $0^\circ < \Theta^0 < 180^\circ$ ) that joins two adjacent faces. The convex and concave edges are identifying based on the concavity test. Concave faces are formed features and convex faces are does not form a feature and the data base of concave faces of the example part model-2 as shown in Table 3. Whereas FN is represents face numbers and CC indicates concavity count. Table 4 shows that, the total number of faces and concavity count or relationship between the faces. The following steps to be adopted to identify the relationship among the faces and identify the corresponding milling features:

**Step-1:** Identify the highest CC values from the Table 4. Face 23 having highest CC value among the other faces i.e. 8 faces, so that the face 23 is having concavity relationship with eight faces and the next highest CC value (i.e.6) faces are 23,22,21,20,18 and 13 are tabulated in Table 5.

**Step-2:** Identify the concavity relationship between these faces (23, 13, 18, 20, 21, 22 and 24) w.r.t to the given data as shown in Figure 9. The concavity/convex relationship among the faces are represented in Table 6. The faces that are having concavity relation with their CC values are shown in Table 7. Based on the production catalog/ rules, the faces 23, 24, 22, 21 and 13 will form a five faced blind pocket.

**Step-3:** Repeat step-1 and step- 2 for the remaining faces and identification of features, exclude the faces 23,24,22,21 and 13 which are already formed a five faced rectangular blind pocket and the remaining faces are tabulated in Table 8. The concavity/convex relationship among the faces are tabulated in Table 9. The faces that are having concavity relation with their CC values are shown in Table 10. From the Table 11 the faces 18, 20, 17 and 19 will form a blind slot.

**Step-4:** Repeat the step-2 to identify the reaming faces and features, exclude the blind pocket and blind slot feature faces and remaining faces are tabulated in the Table 11. To check the concavity/convex relationship among the faces are tabulated in Table 12. The faces that are having concavity relation with their CC values are shown in Table 13. From the Table 14 the faces 8, 9 and 10 will form a blind step.

**Figure 9. Output of MFR algorithm for milling features**

```
C:\Documents and Settings\devs\Desktop\Main Programs\latestcylinder\src>java Den
oProject
total fields 132
total field ids 26
total faceNumbers 26
total lines 4
total planes 120
2
Face 0 matched with face 1
face 0 matched with face 2
face 0 matched with face 2
face 0 matched with face 12
face 0 matched with face 12
3--1->4--3          -1
3--2->5--3           1
3--3->6--1           -1
3--4->7--1           -1
4--1->8--3           -1
4--2->5--4           1
```

**Step-5:** Repeat step-1 and step-2 to recognize remaining feature faces, leave the blind pocket, blind slot and blind step feature faces and the reaming faces are tabulated in the Table 15. The concavity/convex relationship among the faces are tabulated in Table 16. The faces that are having concavity relation with their CC values are shown in Table 17. From Table 18 the faces 4, 5, 6 and 7 will form a through pocket.

**Step-6:** Repeat step-1 and step-2 to identify the left features in the example part model, exclude the feature faces which are already formed features and the reaming feature faces are tabulated in the Table 19. The concavity/convex relationship among the faces are tabulated in Table 3.5. The faces that are having concavity relation with their CC values are shown in Table 19 From the Table 19 the left feature through slot is formed between the faces 15, 14 and 16.

The developed MFRA in this work can be able to give better results as compared to other techniques which are developed in the earlier. In addition, the proposed MFRA can be capable to identify some special features like blind pocket, blind step, blind slot etc. Also, the Proposed MFRA can recognize most of the milling features with their dimensions along with direction material removal, which is useful for assigning proper tools and tool approach direction while machining.

## CONCLUSION

This work presents classification and automatic extraction of cylindrical and milling features in conventional machining process parts by using Hole Recognition Algorithm (HRA) and Milling Feature Recognition Algorithm (MFRA). The features are taper holes, through holes, cylindrical bosses, slots, and pockets are extracted. Two case studies are selected for implementation and validation of developed algorithm. This study put forth the following conclusions:

- Cylindrical and milling features are classified based on connectivity between the faces.
- Both HRA and MFRA algorithm are feasible to extract cylindrical features (through holes, blind holes, taper holes, and bosses) and milling features (slot, blind slot, step, blind step, and pockets).
- The implementation of methods finds well under cylindrical and milling features and extracted all the features for the case study-I and II.

**International Journal of Manufacturing, Materials, and Mechanical Engineering**  
 Volume 11 • Issue 3 • July-September 2021

**Table 3. Concavity relationship between the faces database of example part model-2**

S.NO	Face numbers (FN)		Relation	S.NO	Face Numbers (FN)		Relation
	Face 1	Face 2			Face 1	Face 2	
1	4	5	-1	23	17	20	-1
2	4	6	-1	24	18	17	-1
3	5	4	-1	25	18	19	-1
4	5	7	-1	26	18	20	-1
5	6	4	-1	27	19	18	-1
6	6	7	-1	28	19	20	-1
7	7	5	-1	29	20	17	-1
8	7	6	-1	30	20	18	-1
9	8	9	-1	31	20	19	-1
10	8	10	-1	32	21	13	-1
11	9	8	-1	33	21	23	-1
12	9	10	-1	34	21	24	-1
13	10	8	-1	35	22	13	-1
14	10	9	-1	36	22	23	-1
15	13	21	-1	37	22	24	-1
16	13	22	-1	38	23	13	-1
17	13	23	-1	39	23	21	-1
18	14	15	-1	40	23	22	-1
19	15	14	-1	41	23	24	-1
20	15	16	-1	42	24	21	-1
21	16	15	-1	43	24	22	-1
22	17	18	-1	44	24	23	-1

**Table 4. Faces with concavity count database of example part model-2**

FN	4	5	6	7	8	9	10	13	14	15	16	17	18	19	20	21	22	23	24
CC	4	4	4	4	4	4	4	6	2	4	2	4	6	4	6	6	6	8	6

**Table 5. Concavity relationship between the faces database of feature-1**

FN	23	13	18	20	21	22	24
CC	8	6	6	6	6	6	6

- An attempt is also made to develop a complete feature recognition system by integrating all the above feature recognition algorithms to recognize features of prismatic parts.

**Table 6. Concavity/convex relationship between the faces database of feature-1**

Faces	Relation (Yes/No)	Type of relation (concave / convex)
13-23	Yes	Concave (-1)
18-23	No	No relation
20-23	Yes	Concave (-1)
21-23	Yes	Concave (-1)
22-23	Yes	Concave (-1)
24-23	Yes	Concave (-1)

**Table 7. Feature-1 faces with concavity count database**

FN	23	24	22	21	13
CC	8	6	6	6	6

**Table 8. Faces with concavity count database of further features**

FN	18	20	4	5	6	7	8	9	10	15	17	19
CC	6	6	4	4	4	4	4	4	4	4	4	4

**Table 9. Concavity/convex relationship between the faces database of feature-2**

Faces	Relation (Yes/No)	Type of relation (concave / convex)
18-20	Yes	Concave (-1)
18-17	Yes	Concave (-1)
18-19	Yes	Concave (-1)
20-17	Yes	Concave (-1)
20-19	Yes	Concave (-1)

**Table 10. Feature-2 faces with concavity count database**

FN	18	20	17	19
CC	6	6	4	4

**Table 11. Faces with concavity count database of further features**

FN	4	5	6	7	8	9	10	15	14	16
CC	4	4	4	4	4	4	4	4	2	2

**International Journal of Manufacturing, Materials, and Mechanical Engineering**  
 Volume 11 • Issue 3 • July-September 2021

**Table 12. Concavity/convex relationship between the faces database of feature-3**

Faces	Relation (Yes/No)	Type of relation (concave / convex)
9-8	Yes	Concave (-1)
10-8	Yes	Concave (-1)
9-10	Yes	Concave (-1)

**Table 13. Feature-3 faces with concavity count database**

FN	8	9	10
CC	4	4	4

**Table 14. Faces with concavity count database of further features**

FN	4	5	6	7	15	14	16
CC	4	4	4	4	4	2	2

**Table 15. Concavity/convex relationship between the faces database of feature-4**

Faces	Relation (Yes/No)	Type of relation (concave / convex)
5-4	Yes	Concave (-1)
6-4	Yes	Concave (-1)
5-7	Yes	Concave (-1)
6-7	Yes	Concave (-1)

**Table 16. Feature-4 faces with concavity count database**

FN	4	5	6	7
CC	4	4	4	4

**Table 17. Faces with concavity count database of left feature in example part model-2**

FN	15	14	16
CC	4	2	2

**Table 18. Concavity/convex relationship between the faces database of feature-5**

Faces	Relation (Yes/No)	Type of relation (concave / convex)
9-8	Yes	Concave (-1)
10-8	Yes	Concave (-1)
9-10	Yes	Concave (-1)

**Table 19. Feature-5 faces with concavity count database**

FN	15	14	16
CC	4	2	2

**Table 20. Milling features with their nature, faces, radius, location and shape**

S.No.	Feature Name	Face numbers	Location	Shape of the feature
1	Through pocket	4,5,6,7	(6,36,0),(6,44,0),(14,44,0),(14,36,0),(14,36,40),(6,44,40),(14,44,40)	
2	Blind slot	17,18,19,20	(0,15,30),(0,15,40),(4,15,40),(40,15,30),(4,0,40),(40,0,30),(0,0,30),(0,0,40)	
3	Blind step	8,9,10	(47,0,30),(47,15,30),(60,15,30),(60,0,30),(47,0,40),(47,15,40),(60,15,40)	
4	Through slot	14,15,16	(0,30,30),(0,30,40),(6,30,40),(60,30,30),(6,0,40),(60,0,30),(0,25,30),(0,25,40)	
5	Blind Pocket	1,2,11,3,12	(24,43,30),(24,43,40),(36,43,30),(36,43,40),(36,37,30),(36,37,40),(24,37,40),(24,37,30)	
6	Blind Pocket	13,21,22,23,24	(50,35,30),(56,35,30),(56,47,30),(50,47,30),(50,47,40),(56,47,40),(56,35,40),(50,35,40)	

The proposed algorithms (HRA and MFRA) in this work can be able to give relevant output for a given input of STEP file generated from any CAD flat form like CATIA, ProE, solid works etc. Also, these algorithms are more flexible to the variations of STEP file format of different vendors that offer different CAD systems. Moreover, in addition with this, the developed algorithms can be able to generate the features with their attributes which are very essential for the downstream applications like process planning. Hence, proposed HRA and MFRA algorithms can be used as systematic approach for other manufacturing application for improving the downstream applications like computer aided process planning, process planning, CAM etc.

## REFERENCES

- Abu, R., & Tap, M. (2007). Attribute Based Feature Recognition For Machining Features. *Journal of Teknologi*, 46(A), 87–103.
- Al-wswasi, M., & Ivanov, A. (2019). A novel and smart interactive feature recognition system for rotational parts using a STEP file. *International Journal of Advanced Manufacturing Technology*, 104(1-4), 261–284. doi:10.1007/s00170-019-03849-1
- Ashok, G., Hebbal, S. S., & Sachidanand, R. (2016). Development of algorithm to recognize through slot feature from STEP AP-224 neutral file. *International Journal of Research in Engineering and Technology*, 5(8), 82–87. doi:10.15623/ijret.2016.0508015
- Case, K., & Wan Harun, W. A. (2000). Feature-based representation for manufacturing planning. *International Journal of Production Research*, 38(17), 4285–4300. doi:10.1080/00207540050205091
- Ciurana, J., Romeu, M. L. G., & Castro, R. (2003). Optimising process planning using groups of precedence between operations based on machined volumes. *Engineering Computations*, 20(1), 67–81. doi:10.1108/02644400310458847
- Gavankar, P., & Henderson, M. R. (1990). Graph-based extraction of protrusions and depressions from boundary representations. *Computer Aided Design*, 22(7), 442–450. doi:10.1016/0010-4485(90)90109-P
- Gindy, N. N. Z. (1989). A hierarchical structure for form features. *International Journal of Production Research*, 27(12), 2089–2103. doi:10.1080/00207548908942677
- Hoffmann, C. M., & Joan-Arinyo, R. (1998). On user-defined features. *Computer Aided Design*, 30(5), 321–332. doi:10.1016/S0010-4485(97)00048-1
- Ismail, N., Abu Bakar, N., & Juri, A. H. (2005). Recognition of cylindrical and conical features using edge boundary classification. *International Journal of Machine Tools & Manufacture*, 45(6), 649–655. doi:10.1016/j.ijmachtools.2004.10.008
- Juan, P. C., Oscar, B. A., Jorge, P., Antonio, T., Oscar, R. S., & Carlos, C. (2020). Reconfigurable 3D CAD features recognition confluent n-dimensional topologies and geometric filters for prismatic and curved models. *Journal of Mathematics*, 8(1356), 1–22.
- Kataraki, P. S., & Abu Mansor, M. S. (2019). Automatic designation of feature faces to recognize interacting and compound volumetric features for prismatic parts. *Engineering with Computers*, 1–17. doi:10.1007/s00366-019-00777-2
- Kiani & Saeed. (2019). Automatic spot welding feature recognition from STEP data. *International symposium on Recent Advances in Electrical Engineering (RAEE) Conference*, 1–6.
- Kumar, S., Shanker, K., & Lal, G. K. (2003). A generative process planning system for cold extrusion. *International Journal of Production Research*, 41(2), 269–295. doi:10.1080/0020754021000020953
- Nagarajan, S., & Reddy, N. V. (2010). STEP-based automatic system for recognising design and manufacturing features. *International Journal of Production Research*, 48(1), 117–144. doi:10.1080/00207540701855419
- Peizhi, S., Qunfen, Q., Yuchu, Q., Paul, J. S., & Xiangjian, J. (2020). A noval learning-based feature recognition method using multiple sectional view representation. *Journal of Intelligent Manufacturing*, 31(5), 1291–1309. doi:10.1007/s10845-020-01533-w
- Ranjan, R., Kumar, N., Pandey, R. K., & Tiwari, M. K. (2005). Automatic recognition of machining features from a solid model using the 2D feature pattern. *International Journal of Advanced Manufacturing Technology*, 26(7-8), 861–869. doi:10.1007/s00170-003-2059-2
- Sangolli, S. I., & Pilli, S. C. (2017). Algorithms for Recognition of Geometric and Parametric Features in prismatic parts using IGES. *International Journal of Engineering and Computer Science*, 6(4), 21018–21033. doi:10.18535/ijecs/v6i4.40
- Senthil Kumar, A., Salim, F. K., & Nee, A. Y. C. (1996). Automatic Recognition of Design and Machining Features from Prismatic parts. *International Journal of Advanced Manufacturing Technology*, 11, 136–145.

Sivakumar, S., & Dhanalakshmi, V. (2013). An approach towards the integration of CAD/CAM/CAI through STEP file using feature extraction for cylindrical parts. *International Journal of Computer Integrated Manufacturing*, 26(6), 561–570. doi:10.1080/0951192X.2012.749527

Sreeramulu, D., & Rao, C. S. P. (2008). A New Methodology for Recognition of Milling Features from STEP File. *Intenational Journal of Applied Management and Technology*, 6(3), 172–190.

Sreeramulu, D., & Rao, C. S. P. (2011). A new methodology for recognizing features in rotational parts using STEP data exchange standard. *International Journal of Engineering Science and Technology*, 3(6), 102–115.

Tan, C. F., Ismail, N., Wong, S., Sulaiman, S., & Osman, M. R. (2007). Development of Hole Recognition System from Step File. *ASEAN Journal on Science and Technology for Development*, 22(3), 285–295. doi:10.29037/ajstd.166

Tan, C. F., Kher, V. K., & Ismail, N. (2013). Design of a feature recognition system for CAD/CAM integration. *World Applied Sciences Journal*, 21(8), 1162–1166.

Vemulapalli, P., Mohan, P., Shah, J. J., & Davidson, J. K. (2014) User defined assembly features & pattern recognition from step AP203. *ASME Conference Proceedings*, 1–13. doi:10.1115/DETC2014-35295

Viswa Mohan, P., & Manish Kumar. (2014). An intelligent feature recognition methodology study for 2.5 D prismatic parts. *International Journal of Computer Engineering & Technology*, 5(4), 119–125.

Wong, T. N., & Lam, S. M. (2000). Automatic recognition of machining features from computer aided design part models. *Proceedings of the Institution of Mechanical Engineers. Part B, Journal of Engineering Manufacture*, 214(6), 515–520. doi:10.1243/0954405001517810

Xu, X., & Hinduja, S. (1998). Recognition of rough machining features in 2D/2D components. *Computer Aided Design*, 30(7), 503–516. doi:10.1016/S0010-4485(97)00090-0

Yusof, Y., & Latif, K. (2014). Survey on computer-aided process planning. *International Journal of Advanced Manufacturing Technology*, 75(1-4), 77–89. doi:10.1007/s00170-014-6073-3

Zubair, A. F., & Abu Mansor, M. S. (2018). Automatic feature recognition of regular features for symmetrical and non-symmetrical cylinder part using volume decomposition method. *Engineering with Computers*, 34(4), 843–863. doi:10.1007/s00366-018-0576-8

*Sathish Kumar Adapa is working as Assistant Professor in the Dept of Mech. Engg., AITAM college Andhra Pradesh, India. Sathish Kumar Adapa completed his M. Tech. in Design and Manufacturing from CUTM Odisha, India, in the year of 2013. Pursuing PhD at NIT Raipur, India. During his 5 years of experience published more than 6 nos. of International/National Journal/conference/book/books chapters. His research interests include advanced manufacturing process; cad/cam; 3d printing; composite material and machining characterization; etc.*

*Sreeramulu Dowluru is working as a Professor in the Dept of Mech. Engg., AITAM College Tekkali, Andhra Pradesh, India. Dr. Sreeramulu Dowluru completed his Ph.D. in CAD/CAM from NIT Warangal, India, in the year of 2010. During his 13 years of experience published more than 65 nos. of International/National Journal/conference/book/books chapters. His research interests include advanced manufacturing process; cad/cam; 3d printing; robotics; optimization techniques; renewable energy, finite elements analysis etc.*

*Jagadish, is an Assistant Professor in Department of Mechanical Engineering, National Institute of Technology Raipur, Chhattisgarh. He received his Diploma (Mechanical) from GPT Bidar (Karnataka); B.E. (Mechanical) from REC Bhalki (Karnataka); M.Tech (Product Design and Development) from NIT Warangal (Andhra Pradesh), Ph.D (Manufacturing Engineering) from NIT Silchar. He has over 3 years of industrial experience in the field of Design and Analysis and 5 years of teaching and research experience. He received Institutional Award (Gold Medal) by institution of engineers India and Best Innovative Award by springer for his outstanding research contribution and published more than 14 research papers. His areas of interests are Modeling of advanced manufacturing process, Green manufacturing, Applied soft computing techniques and optimization etc.*

# Turning SKD 11 Steel Using Silver Nanofluids With Minimum Quantity Lubrication

M. Naresh Babu, Easwari Engineering College, Chennai, India

V. Anandan, Saveetha Engineering College, Chennai, India

M. Dinesh Babu, Panimalar Engineering College, Chennai, India

N. Muthukrishnan, Sri Venkateswara College of Engineering, India

## ABSTRACT

The influence of lubrication has an effect on health, surroundings, and manufacturing regions. In the current analysis, the impact of turning parameters such as cutting speed, feed rate and cutting conditions on surface roughness ( $R_a$ ), cutting temperature, tool wear, and chip morphology are examined on SKD 11 steel. The experiments were performed with Taguchi's L18 orthogonal-array. The significance of the investigation involved in comparing the effect of dry, oil machining, and nano lubricants with minimum quantity lubrication (MQL) in turning process. Additionally, simple additive weighting method (SAW) has been utilized to enhance the turning parameters in SKD 11 steel for improved machining performance. Results indicate that the use of nanoparticles as cutting fluids serve in reducing the surface roughness, cutting temperature, and wear on the tool.

## KEYWORDS

Chip Morphology, Nanofluids, Silver, Simple Additive Weighting Method, Surface Roughness, Tool Wear

## INTRODUCTION

SKD 11 steel is widely preferred in blanking dies, thread rolling dies, shear daggers, food handling blades, screw heading molds and punches. Also the exceptional opposition property to wear makes it to be preferred in industrial sectors. However, it is necessary to identify a suitable lubrication to improve the machining performance in turning SKD 11 steel. But the high carbon and chromium content in SKD 11 steel makes it harder throughout machining, hence the determination of optimized machining parameters along with suitable lubrication becomes essential. Turning is a machining process in which heat is generated during the distortion of work piece and the movement of chip on the tool rake side which produces poor surface on work piece and creates excess tool wear (Lawal, Choudhury, & Nukman, 2013). The manufacturing of good value components demands innovative machining methods to produce components with high accuracy. The use of minimum quantity lubrication increases the output considerations as per the requirement (Nam & Lee, 2018). Singh, Dureja, & Dogra, (2019) demonstrated the use of canola oil and graphene nanoparticles with canola oil under MQL in turning AISI 4340 steel and concluded that flank wear, cutting forces and cutting temperature were minimized with graphene nanolubricants due to effective penetrating ability of nanoparticles in the machining areas in comparison with canola oil. Singh, Sharma, & Dogra, (2020)

DOI: 10.4018/IJMMME.2021070105

Copyright © 2021, IGI Global. Copying or distributing in print or electronic forms without written permission of IGI Global is prohibited.

performed experiments under dry condition, flood lubrication and graphene nanoplatelets with MQL in grinding of Ti-6Al-4V-ELI and observed that high thermal conductivity and adsorption capability of graphene in canola oil with MQL considerably reduced the surface roughness, grinding force, specific grinding energy and coefficient of friction compared to flood lubrication. Abbas et al. (2019) confirmed that the use of  $\text{Al}_2\text{O}_3$  nanofluids increase the value of sliding which results in reducing the surface roughness and power consumption compared to flood and dry condition in turning AISI 1045 steel. Kumar et al. (2019) reported that cutting temperature, flank wear and surface roughness minimise considerably due to excellent heat transfer with 0.01%wt of  $\text{TiO}_2$  nanofluids comparing  $\text{Al}_2\text{O}_3$  nanofluids in turning AISI D2 steel. Khandekar et al. (2012) determined that  $\text{Al}_2\text{O}_3$  nanofluids improves the conduction, convection and wettability by reducing the cutting force, surface roughness and tool wear in turning AISI 4340. Raju, Andhare, & Sahu, (2012) stated that use of multiwalled carbon tubes maintains maximum wettability and excellent thermal conductivity which improves the surface finish and decreases cutting force in turning EN 31 steel in comparison to conventional lubrication. Das et al. (2020) examined the performance of  $\text{Al}_2\text{O}_3$  nanofluids with MQL in turning AISI 4340 steel and confirmed that cutting force and tool wear are minimized compared to air lubrication and water soluble lubrication. It is also observed that cutting speed and depth of cut play a vital role in increasing the cutting force and feed force on the work material. Saravanakumar et al. (2014) performed turning experiments and noticed that cutting force, cutting temperature and surface roughness are minimized under silver nanofluids. Kumar Sharma et al. (2020) compared the performance of alumina nanofluids with hybrid nanofluids of alumina with carbon nanotubes under MQL in turning AISI 304 and revealed that hybrid nanofluids retains high specific heat and thermal conductivity which reduce the tool wear, surface roughness and cutting forces. Khan et al. (2009) performed experiments in turning 9310 steel under MQL and noticed that surface roughness and tool wear were reduced with MQL machining compared to wet machining conditions. Yildirim et al. (2019) examined the effects of MQL in milling waspaloy and observed that the tool wear were decreased by 29% and 37% in comparison with dry and wet lubrication and also a considerable reduction in surface roughness. Suneesh & Sivapragash (2019) used TOPSIS method to optimize process parameters in turning magnesium/alumina hybrid composites and noted that surface roughness, cutting force, power consumption and tool wear were minimized with MQL. Ajay Vardhaman et al. (2018) used coconut oil based MQL in turning AISI 1040 steel and concluded that outstanding adsorption capability of MQL with coconut oil to improve the surface quality and tool life in evaluation with dry and wet lubrication. Das et al. (2019) compared the impact of  $\text{Al}_2\text{O}_3$  nanofluids with compressed air and water soluble coolant in turning 4340 hardened alloy steel. The results confirmed that there was a reduction in surface roughness by 78%, tool wear by 49% and cutting force by 55% with  $\text{Al}_2\text{O}_3$  nanofluids under MQL in comparison with air and water lubrication. It was found that mechanical stress and temperature generated at tool-chip contact area were minimized due to good heat transfer ability of  $\text{TiO}_2$  nanofluids in turning AISI 4140 steel (Khajehzadeh, Moradpour, & Razfar, 2018). The influence of dry, conventional cooling and MQL in turning Haynes 25 superalloy was examined. The result indicates that tool wear and surface roughness were minimized with MQL condition (Sarikaya, Yilmaz, & Gullu, 2016). Yildirim et al. (2019) executed turning experiments with hexagonal boron nitride as nanofluids with MQL and confirmed that the tool wear, surface roughness and cutting temperature were decreased with 0.5% volume of hexagonal boron nitride as nanofluids in Inconel 625 in contrast with dry and pure MQL conditions. The performance evaluation of  $\text{Al}_2\text{O}_3$  nanoparticle with MQL in milling 60Si<sub>2</sub>Mn steel indicates that 0.5% of  $\text{Al}_2\text{O}_3$  nanoparticle improves the tool life by 177%. Further, surface roughness and cutting force were reduced with nanofluids by 35%-60% due to good tribological performance of nanoparticles (Minh, The, & Bao, 2017). The SiO<sub>2</sub> nanoparticles decreased the cutting force due to rolling action of nanoparticles at tool-chip area and also the specific energy and coefficient of friction were decreased in milling process (Sarhan, Sayuti, & Hamdi, 2012). Wang et al. (2016) observed that grinding force, wheel wear were decreased and surface quality was improved when the concentration of  $\text{Al}_2\text{O}_3$  nanoparticles was

increased by 1.5% with MQL in grinding nickel alloys. Sirin & Kivak (2019) noticed that 0.5% volume of hexagonal boron nitride minimised the machining temperature, surface roughness and tool wear in comparison with MoS<sub>2</sub> and graphite nanofluids during milling Inconel X-750 alloys. Sahu, Andhare, & Raju, (2018) determined that nanofluids provide effective cooling action in reduction of surface roughness by 7%, tool wear by 34% and cutting force by 28% in turning Ti-6Al-4V alloy with dry, conventional machining and multi walled carbon nanotubes as nanofluids. The performance of SAE 20W40, cashew nut shell oil and nano TiO<sub>2</sub> filled cashew nut shell oil as base fluid was analysed by Nandakumar, Rajmohan, & Vijayabhaskar (2019). The penetrating ability of TiO<sub>2</sub> nano fluids was effective in minimizing the temperature and tangential forces in grinding SiC reinforced Al matrix composites. Thakur, Manna, & Samir (2019) introduced a mechanism with better tribological performance of nanoparticles in which the silicon carbide nanofluids with MQL reduce the surface roughness, cutting force and temperature in turning EN24 steel compared to MQL. Amrita et al. (2013) performed an experimental study in turning AISI 1040 under nano graphite as cutting fluid and confirmed that tool wear, surface roughness, temperature and cutting force were reduced due to superior cooling and lubricating of nanofluids in soluble oil. Sharma et al. (2019) confirmed that an increase in 1.25% volumetric concentration of hybrid nanoparticles (multiwalled carbon nanotubes with alumina) significantly decrease the flank wear by 11% and temperature by 27% in turning AISI 304. Rahman et al. (2018) conducted a comparative study using Al<sub>2</sub>O<sub>3</sub>, MoS<sub>2</sub> and rutile-TiO<sub>2</sub> nanoparticles with vegetable oil such as canola and olive oils at varying concentrations. Excellent surface finish was obtained with Al<sub>2</sub>O<sub>3</sub> nanoparticles with canola oil at 0.5 vol%. Further, MoS<sub>2</sub> nanoparticles with canola oil at 0.5 vol% reduced the cutting temperature in turning Ti-6Al-4V ELI due to formation of defensive layer by nanoparticles. Rosnan et al. (2019) conducted drilling of NiTi alloys with Al<sub>2</sub>O<sub>3</sub> nanoparticles under MQL and observed that tool wear were reduced with cutting speed in the range 10-20 m/min. Further the thrust force were also minimised due to rolling action of nanoparticles over the machining area in comparison with flood cooling. Singh et al. (2019) performed experiments with graphene, graphite and MoS<sub>2</sub> nanoparticles in surface grinding of Ti-6Al-4V- ELI and confirmed that 1.5% of graphene nanoparticles reduced the surface roughness, coefficient of friction by 40% and specific grinding energy by 15%, which indicates that the graphene nanoparticles play a vital role in improving the tribological performance. Lv et al. (2018) recommended electrostatic MQL in milling process and found that coefficient of friction was reduced due to efficient penetrating ability of graphene nanoparticles with MQL. Li et al. (2018) observed that graphene nanoparticles improves the milling force by 18%, temperature by 13%, surface micro hardness by 8% and surface roughness by 24% in milling TC4 alloys due to superior cooling and lubricating ability of nanoparticles. Bai et al. (2019) used six nanofluids namely Al<sub>2</sub>O<sub>3</sub>, SiO<sub>2</sub>, MoS<sub>2</sub>, CNTs, SiC, and graphite with cottonseed oil as base fluids in milling titanium alloys and determined that Al<sub>2</sub>O<sub>3</sub> nanoparticles when mixed with the base oil provide an efficient lubrication which minimize the surface roughness and cutting force in contrast with other nanoparticles. Hegab et al. (2018) noticed that an increase in 4%wt of multi walled carbon nanotubes improves the heat dissipation proficiency which results in reducing the surface roughness by 38% in turning Ti-6Al-4V. Sharma et al. (2016) noted that an increase in concentration of Al<sub>2</sub>O<sub>3</sub> nanoparticles reduces the tool wear, surface roughness and cutting force in turning AISI 1040 steel. This is mainly due to increase in thermal conductivity, viscosity and density of nanofluids. Gupta et al. (2020) performed experiments in turning titanium alloy under Ranque hilsch vortex tube MQL (RHVT-MQL) with conventional MQL systems and noticed that RHVT-MQL serve as a suitable substitute in reducing the surface roughness, cutting force and power consumption. Gupta et al. (2018) studied the effects of dry cutting, nitrogen cooling, nitrogen with MQL and Ranque hilsch vortex tube (RHVT) N<sub>2</sub> MQL in turning Al 7075-T6 and concluded that RHVT assisted N<sub>2</sub> MQL play a prominent role in minimizing the surface roughness by 77% and tool wear by 118% compared with other cooling methods. Singh et al. (2019) noticed that surface roughness, cutting force and tool wear were reduced due to effective lubrication provided at the machining zone under Ranque hilsch vortex tube (RHVT) with MQL in turning titanium alloys.

The previous researches exhibits that exceptional lubrication has been developed with nanofluids based minimum quantity lubrication. But there was no record of any attempt using silver as nanofluids in turning SKD 11 steel and this area requires a comprehensive examination. The current research involves in observing the effect of surface roughness, temperature, tool wear and quality of the chips under dry, oil and silver nanofluids with MQL in turning SKD 11 steel. The results suggests that silver based nanofluids will serve as a replacement to other cutting fluids in reducing the production cost incurred and other technical issues in manufacturing industries.

## EXPERIMENTAL PROCEDURE

SKD 11 tool steel of dimensions 17 mm in diameter and 130 mm in length is considered as the work material. It has high carbon and chromium content which has tremendous resistance against wear. It is used to manufacture scissors, circular saw blades, making of hot work dressing dies, rolled knives, stamping dies and pressing dies, deep drawing dies, cold heading dies and cold extrusion. The chemical composition of SKD 11 tool steel is shown in Table 1.

**Table 1. Chemical composition of SKD 11steel**

Element	C	Si	Mn	P	S	Cr	Mo	V	Ni	Fe
Component (%)	1.47	0.32	0.54	0.025	0.027	12.2	0.9	0.4	0.32	Remaining

A digital surface roughness tester “Taylor hobson-surtronic S-128” was used to measure the roughness values ( $R_a$ ) of the work material. The cut-off length and traverse length considered for roughness was 0.8 mm and 4 mm respectively. A non-contact type infrared thermometer (make: Fluke 59 MAX) was used to measure the temperature, which allows temperature measurement in the range of -30 °C to 500 °C. The point of measurement of cutting temperature was targeted at tool-chip zone since maximum temperature was generated in that zone. During each experiment, maximum temperature at tool-chip zone was measured and the values obtained are considered for the study. A SEM (scanning electron microscope) of Model: Hitachi S-3400N was used to observe the wear on the tool (insert).

The steps involved in preparation of nanofluids are shown in Figure 1. Ethylene glycol was selected as the base fluid. It serves as a link for convective heat transfer. The nanoparticles of size 50 nm were used. About 1.5 grams of silver nanoparticles were dissolved in 200 ml of base fluid in ultrasonicator (Model: Maxsell- MX35SH, 35W, 50Hz) for 45 min at room temperature. A surfactant of sodium dodecylbenzenesulfonate (SDBS) to 1/10 weight of nanoparticle (Singh, Dureja, & Dogra, 2019) was utilized to improve the firmness of nanofluids. The prepared nanofluids were found to be steady through SEM as shown in Figure 2. Moreover, in order to avoid settlement of nanoparticles, the nanofluids were used instantly once prepared for machining.

MQL system considered in turning SKD 11 steel was shown in Figure 3. It consists of tank, pump, compressor, control valve, pressure gauge, mixing chamber and a nozzle. Dry compressed air enters the mixing chamber from one side and cutting fluid from the tank enters the mixing chamber through other end. The control valves are used to control the flow of cutting fluid and pressure gauge used to maintain the necessary pressure required. The air-lubricant mixture developed from the mixing chamber strike the machining zone through the nozzle like a forced gas.

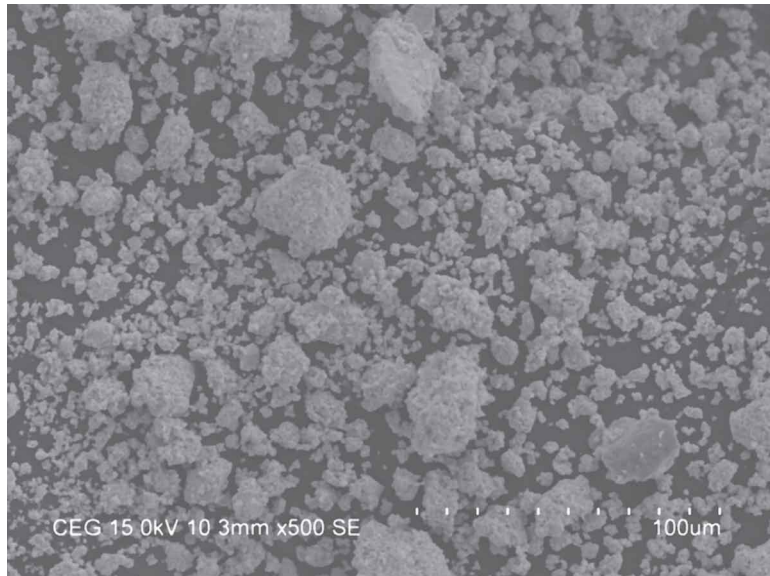
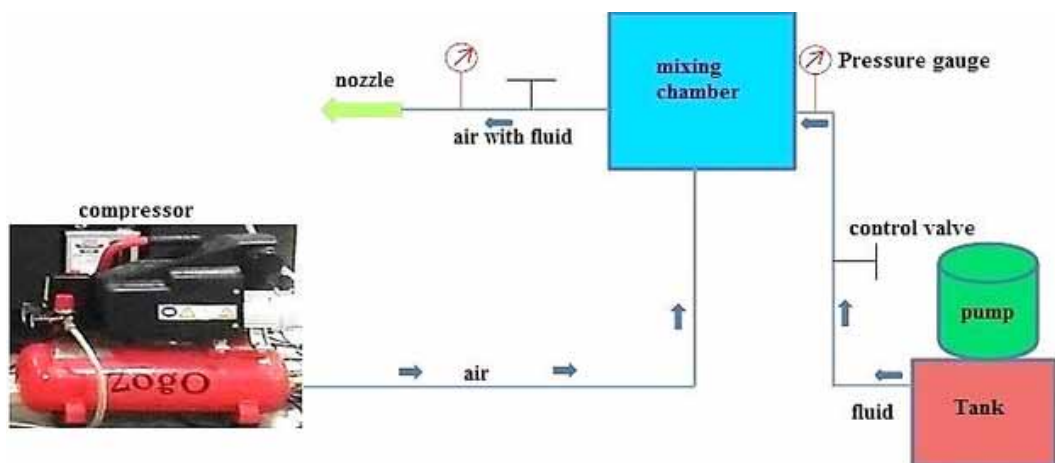
The factors with their levels (Table 2) were obtained based on the specifications of the machine. Turning experiments were executed on CNC turning centre of Super Jobber (Make: ACE designers LTD- INDIA) and the machining zone were shown in Figure 4. The machining details are shown in

**Figure 1. Nanofluid preparation**

Table 3. In the existing work, the interaction effects between the parameters were ignored. The degrees of freedom for array should be  $\geq$  the factors considered. L18 orthogonal array was considered for the experimentation has 17 degrees of freedom which is  $>$  degrees of freedom of the factors considered. Hence,  $L_{18}$  orthogonal array was selected for the experimental section. The experiments were executed in a random manner to minimize the impact of unwanted factors. The tool holder and inserts were shown in Table 4 and experimental results are shown in Table 5.

### SIMPLE ADDITIVE WEIGHTING METHOD

SAW (Simple Additive Weighting) method or scoring method was suggested by Churchman, Ackoff and Amoff in 1957 (Churchman, Ackoff, & Amoff, 1957). Later in 1981, Hwang and Yoon developed SAW method. It is one of the multi criteria decision-making techniques which were widely used in complex decision-making situations and it is created on weighted average. It calculates weighted sum of performance values of every factor with all substitutes in entire attributes (Unal & Maleki, 2018).

**Figure 2. SEM image of Nanoparticles****Figure 3. MQL system****Table 2. Parameters and levels for machining**

Symbol	Factors	Unit	1	2	3
f	Feed rate	(mm/rev)	0.3	0.4	-----
A	Cutting environment	-----	Dry	Oil	Nanofluid
V <sub>c</sub>	Cutting speed	(m/min)	70	85	100

**Figure 4. Machining centre****Table 3. Machining details**

Oil delivered with MQL	canola oil
Nanoparticles delivered with MQL	Silver
MQL flow rate	10 ml/min
Air pressure	2 bar
Depth of cut	0.3 mm

**Table 4. Details of tool holder and insert**

Tool holder	PCNL 2525M12
Insert	Carbide inserts CNMG 120408MT of make TaeguTec

It accepts additive combination of decision results which were measured by weights, conveying the significance of the method (Shakouri, Nabae, & Aliakbarisani, 2014). A maximum grade were selected as the best trial and it the widely used because of its lesser computation time. The step wise procedure is given below:

A decision matrix D is constructed using the responses from Table 5:

**Table 5. Experimental Results**

Test order	Feed (mm/rev)	Cutting Environment	Cutting speed (m/min)	Surface roughness-Ra ( $\mu\text{m}$ )	Temperature (°C)
1	0.3	Dry	70	3.2	115
2	0.3	Dry	85	3.7	120
3	0.3	Dry	100	4.4	146
4	0.3	Oil	70	1.6	37
5	0.3	Oil	85	1.87	34
6	0.3	Oil	100	1.45	32
7	0.3	Nanofluid	70	0.53	23
8	0.3	Nanofluid	85	0.6	22
9	0.3	Nanofluid	100	0.42	23
10	0.4	Dry	70	3.4	130
11	0.4	Dry	85	4.49	147
12	0.4	Dry	100	4.89	125
13	0.4	Oil	70	1.38	32
14	0.4	Oil	85	1.5	34
15	0.4	Oil	100	1.26	37
16	0.4	Nanofluid	70	0.53	24
17	0.4	Nanofluid	85	0.7	23
18	0.4	Nanofluid	100	0.24	26

$$D = \begin{pmatrix} x_{11} & x_{12} & \dots & x_{1n} \\ x_{21} & x_{22} & \dots & x_{2n} \\ \vdots & \vdots & \ddots & \vdots \\ x_{m1} & x_{m2} & \dots & x_{mn} \end{pmatrix} \quad i = 1, 2, \dots, m \text{ and } j = 1, 2, \dots, n$$

where 'm' and 'n' indicates the number of alternatives and criteria respectively.

2. Determine the weight of the criterion ' $w_j$ '.
3. Since every criteria has different meaning, the decision matrix is normalised using:

$$n_{ij} = \frac{x_{ij} - \min(x_{ij})}{\max(x_{ij}) - \min(x_{ij})} \quad (\text{for maximization}) \quad (1)$$

$$n_{ij} = \frac{\max(x_{ij}) - x_{ij}}{\max(x_{ij}) - \min(x_{ij})} \text{ (for minimisation)} \quad (2)$$

4. The weighted additive grade of each alternative is calculated using:

$$W = \sum_{j=1}^n n_{ij} \times w_j \quad (3)$$

5. The alternatives are ranked based on the highest values of  $W$ .  
 6. The analysis of variance is carried out to find the significant factors.

## RESULTS AND DISCUSSIONS

A decision matrix was developed from the responses in Table 5 and weights were assigned for all the trials selected. The decision matrix was normalized for maximum and minimum values using equations 1 and 2 and values obtained are listed in Table 6. The SAW grade for each test was calculated individually using equation 3 and the grade values are listed in Table 7. Based on the SAW grade value, ranks were allocated as shown in Table 7. The lowest rank indicates poor performance and highest rank indicates best performance (Unal & Maleki, 2018). Hence, the poor (initial) trial in turning SKD 11 steel was test order 11 (Table 7) with SAW grade value of 0.2608 and best (optimal) trial in turning SKD 11 steel was test order 18 (Table 7) with 0.9231 as SAW grade value.

The initial trial obtained through grade values possess high feed rate, dry cutting condition with medium cutting speed. The optimal trial possess high feed rate, nanofluids cutting condition with high cutting speed. ANOVA (Table 8) is used to determine the dominating factors influencing the responses in turning SKD 11 steel. The results suggests that environment is the significant factor in deciding the responses contributing to 93% and other factors were not so significant as their contribution was cutting speed with 1% and feed as 0% respectively. Hence from the grade values (Table 7), test order 11 which has least grade values were considered as initial trial (Unal & Maleki, 2018) indicating f2A1V<sub>c</sub>2 as high feed rate, dry cutting condition with medium cutting speed. Similarly, from the grade values (Table 7) test order 18 which has high grade values were considered as optimal trial (Unal & Maleki, 2018) indicating high feed rate, nanofluids cutting condition with high cutting speed. Hence, from the SAW grade values it confirms that environment (nanofluids) play a major role in reducing the surface roughness, cutting temperature and tool wear in turning process.

## SURFACE ROUGHNESS

The various practical characteristics like abrasion, wear, lubrication and reflection of light mainly depends on the surface roughness. Further, the qualities of the machined component were mostly influenced by the roughness values of the machined work part. Hence analyzing the surface roughness becomes a vital part in the current study. The arithmetic mean surface roughness ( $R_a$ ) was considered for the study which is the widely preferred (Chetan et al. 2016). Low surface roughness leads to high quality of the surfaces produced. The initial trial was identified with low grade value for test order 11 (Unal & Maleki, 2018) as f2A1V<sub>c</sub>2 with high feed rate, dry cutting condition with medium cutting speed. ANOVA (Table 8) reveals that environment is the important factor in determining the surface roughness on the work material. Machining under dry environment yields high surface roughness values on the machined component (Huang et al. 2017). Due to the absence of lubrication, excess

**Table 6. Normalized and weighted normalized values of responses**

Test order	Ra (normalized)	Temperature (normalized)	Ra (weighted normalized)	Temperature (weight normalized)
1	0.0750	0.4889	0.0375	0.2444
2	0.0649	0.5500	0.0324	0.2750
3	0.0545	0.4783	0.0273	0.2391
4	0.1500	0.5946	0.0750	0.2973
5	0.1283	0.6471	0.0642	0.3235
6	0.1655	0.6875	0.0828	0.3438
7	0.4528	0.9565	0.2264	0.4783
8	0.4000	1.0000	0.2000	0.5000
9	0.5714	0.9565	0.2857	0.4783
10	0.0706	0.4889	0.0353	0.2444
11	0.0535	0.4681	0.0267	0.2340
12	0.0491	0.4889	0.0245	0.2444
13	0.1739	0.6875	0.0870	0.3438
14	0.1600	0.6471	0.0800	0.3235
15	0.1905	0.5946	0.0952	0.2973
16	0.4528	0.9167	0.2264	0.4583
17	0.3429	0.9565	0.1714	0.4783
18	1.0000	0.8462	0.5000	0.4231

plastic deformation, undulations and uneven abrasion path leads to an increase in surface roughness value on the work material (Rahman et al. 2018). The roughness profile obtained (Figure 5) with initial trials f2A1V<sub>c</sub>2 (high feed rate, cutting condition as dry with medium cutting speed) shows the Ra value of 4.49  $\mu\text{m}$ . Hence with initial trial, an increase in roughness value of 66% compared with oil machining of 1.50  $\mu\text{m}$  and 94% with nanofluids with optimal trials were obtained with surface roughness value of 0.243  $\mu\text{m}$ .

Machining with initial trials (f2A1V<sub>c</sub>2) with oil under MQL environment reveals that the formation of built up edges were eliminated at tool-chip region resulting in lowering the cutting force due to smooth flow of chips. Hence, a decrease in surface roughness was identified on the work material (Gajrani et al. 2019). The roughness profile obtained (Figure 6) with initial trials f2A1V<sub>c</sub>2 (high feed rate, cutting environment as MQL with oil and medium cutting speed) shows the Ra value of 1.5  $\mu\text{m}$ .

Machining with optimal trials f2A3V<sub>c</sub>3 (high feed rate, cutting condition as nanofluids with high cutting speed) indicates that nanofluids generally provide smooth surface finish on the machined part (Rahman et al. 2018). The circular nature of nanoparticles perform a rolling effect on the work material, hence a reduction in sliding friction were obtained (Bai et al. 2019). Thus, the surface roughness values were decreased with silver nanoparticles (Chetan et al. 2016). The surface roughness value obtained with optimal trial was 0.24  $\mu\text{m}$  (Figure 7) which has less twist and turn profile. Hence, with optimal trials the roughness value has been minimized by 94% with initial trials under dry machining and 84% with initial trial under oil machining with MQL.

**International Journal of Manufacturing, Materials, and Mechanical Engineering**  
 Volume 11 • Issue 3 • July-September 2021

**Table 7. SAW grades and ranks allotted**

Test order	SAW grade	Rank
1	0.2819	14
2	0.3074	13
3	0.2664	17
4	0.3723	12
5	0.3877	11
6	0.4265	8
7	0.7047	3
8	0.7000	4
9	0.7640	2
10	0.2797	15
11	0.2608	18
12	0.2690	16
13	0.4307	7
14	0.4035	9
15	0.3925	10
16	0.6847	5
17	0.6497	6
18	0.9231	1

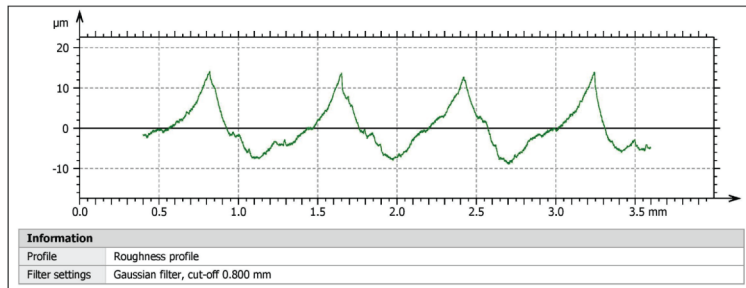
**Table 8. Effects of ANOVA**

Symbol	Factors	Sum of Squares	Degrees of freedom	Mean Sum of squares	F-ratio	% Contribution
f	Feed	0.0004	1	0.0004	0.1119	0%
A	Cutting environment	0.6797	2	0.3398	99.7111	93%
Vc	Cutting speed	0.0108	2	0.0054	1.5899	1%
	Error	0.0409	12	0.0034		6%
	Total	0.7318	17			100%

## MACHINING TEMPERATURE

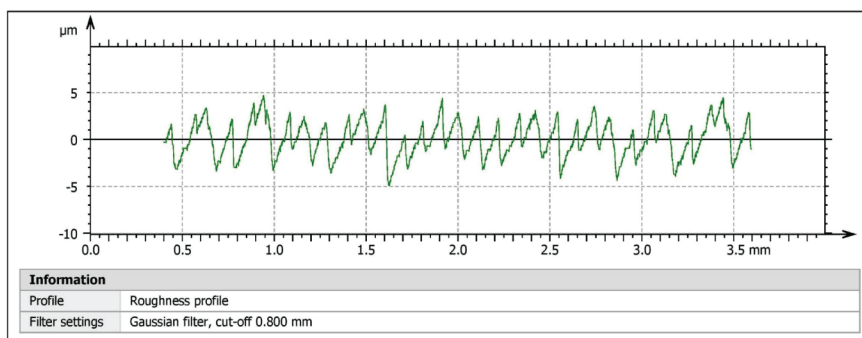
High friction attained at tool-work and tool-chip zone play a dominant role in generation of heat, hence an increase in temperature were observed. Further, temperature generated during machining has to be minimized as it plays a major part in increasing the life of the tool. Thus it is mandatory to reduce the temperature generated in turning process. Table 8 suggests environment is the major parameter in deciding the temperature generated during machining. Hence, machining with initial trials ( $f2A1V_c2$ ) with high feed rate, dry cutting condition with medium cutting speed indicates in the event of dry machining, due to nonexistence of lubrication causing an increase in abrasion and lack of heat transfer which gives raise to increase in temperature at tool-work region. The temperature generated

Figure 5. Roughness graph for initial trial under dry lubrication



ISO 4287		
Amplitude parameters - Roughness profile		
R <sub>a</sub>	4.49	μm Gaussian filter, 0.8 mm
R <sub>p</sub>	13.4	μm Gaussian filter, 0.8 mm
R <sub>v</sub>	8.21	μm Gaussian filter, 0.8 mm
R <sub>t</sub>	22.9	μm Gaussian filter, 0.8 mm
R <sub>z</sub>	21.6	μm Gaussian filter, 0.8 mm

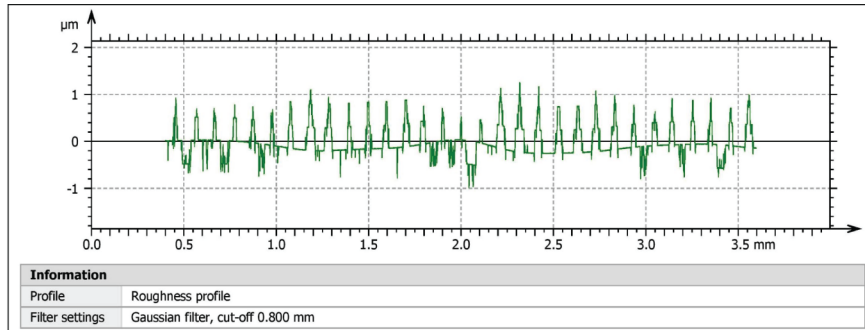
Figure 6. Roughness graph for initial trial under oil lubrication



ISO 4287		
Amplitude parameters - Roughness profile		
R <sub>a</sub>	1.50	μm Gaussian filter, 0.8 mm
R <sub>p</sub>	4.16	μm Gaussian filter, 0.8 mm
R <sub>v</sub>	4.18	μm Gaussian filter, 0.8 mm
R <sub>t</sub>	9.61	μm Gaussian filter, 0.8 mm
R <sub>z</sub>	8.35	μm Gaussian filter, 0.8 mm

was 147 °C which is 76% higher than initial trials under oil machining with MQL and 82% higher than optimal trials with nanofluids. With initial trials as f2V<sub>c</sub> 2 and environment as oil machining, indicates that oil with MQL makes the oil droplets to penetrate efficiently at tool-work material zone, hence an excellent heat transfer was attained which simultaneously improves the lubrication paving a way in reducing the temperature (Khan & Maity, 2018). It was noticed that a temperature of 34 °C obtained in initial trial with oil machining which is 76% lesser compared to dry machining with initial trial. Machining with optimal trial f2A3V<sub>c</sub> 3 (high feed rate, nanofluids cutting condition with high cutting speed) indicates that silver nanofluids has high thermal conductivity (Chetan et al. 2016; Fang et al. 2013). High thermal conductivity reduces the machining temperature (Padmini,

**Figure 7. Roughness graph for optimal trial under nanofluids**



ISO 4287		
Amplitude parameters - Roughness profile		
R <sub>a</sub>	0.243	μm Gaussian filter, 0.8 mm
R <sub>p</sub>	1.09	μm Gaussian filter, 0.8 mm
R <sub>v</sub>	0.824	μm Gaussian filter, 0.8 mm
R <sub>t</sub>	2.22	μm Gaussian filter, 0.8 mm
R <sub>z</sub>	1.92	μm Gaussian filter, 0.8 mm

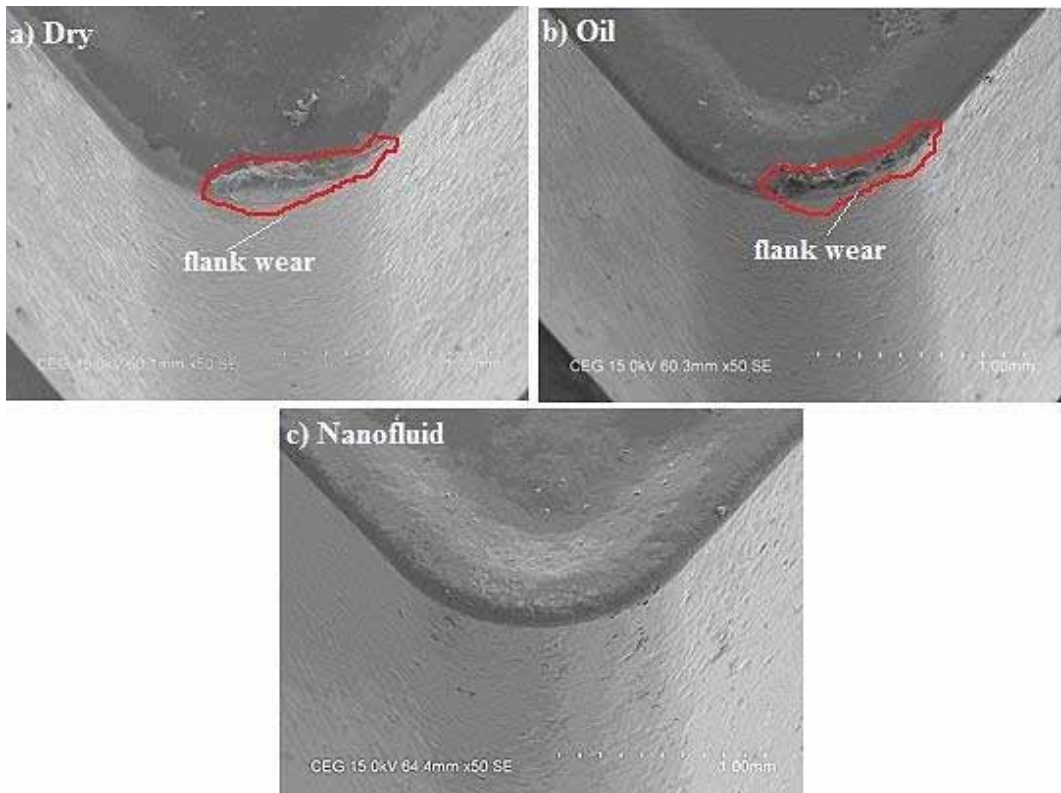
Vamsi Krishna, & Krishna Mohana Rao, 2016), hence the heat generated at the tool-work material interface was eliminated. Therefore, temperature produced were 26 °C which is 82%  $\downarrow$  the initial trial under dry machining and 23%  $\downarrow$  than initial trial under oil machining with MQL.

## TOOL WEAR

Tool wear is the most important criteria which determine the machinability of the material. The tool wear considered for the examination was flank wear ( $V_B$ ) because it plays a dominant role in determining the tool life and superiority of the machined surface (Amini, Khakbaz, & Barani, 2015). Machining with initial trial under dry machining indicates excess rubbing between tool- work material interface which results in formation of built-up edges (BUE) due to nonexistence of lubrication. Also, high abrasion leads to increase in wear on the tool (Amini, Khakbaz, & Barani, 2015) as shown in Figure 8a. Further, the formation of flank wear is quite common in dry machining (Chetan et al, 2016). The tool wear under oil machining was slightly minimized compared to dry machining. MQL with oil provide tremendous chilling effect at the machining zone, hence a decrease in friction was obtained (Khan & Maity, 2018; Amini, Khakbaz, & Barani, 2015). Also, canola oil contains high specific heat capacity around 21%, hence it improves the heat removal at the machining zone (Singh, Dureja, & Dogra, 2019) which results in reduction of flank wear as shown in Figure 8b. Nanofluids form a slim coating with abundant atoms when mixed with base fluids and these slim coatings enhances the heat transfer rate (Jia et al, 2017). Machining with nanofluids under MQL result in separation of nanoparticles due to enormous velocity of air. Thus, the nanoparticles concentrate at tool-work material zone, hence the interaction within chip-tool decreases which favors in minimizing the heat obtained. Thus a decrease in wear was noticed (Babu et al, 2018) as shown in Figure 8c.

## CHIP MORPHOLOGY

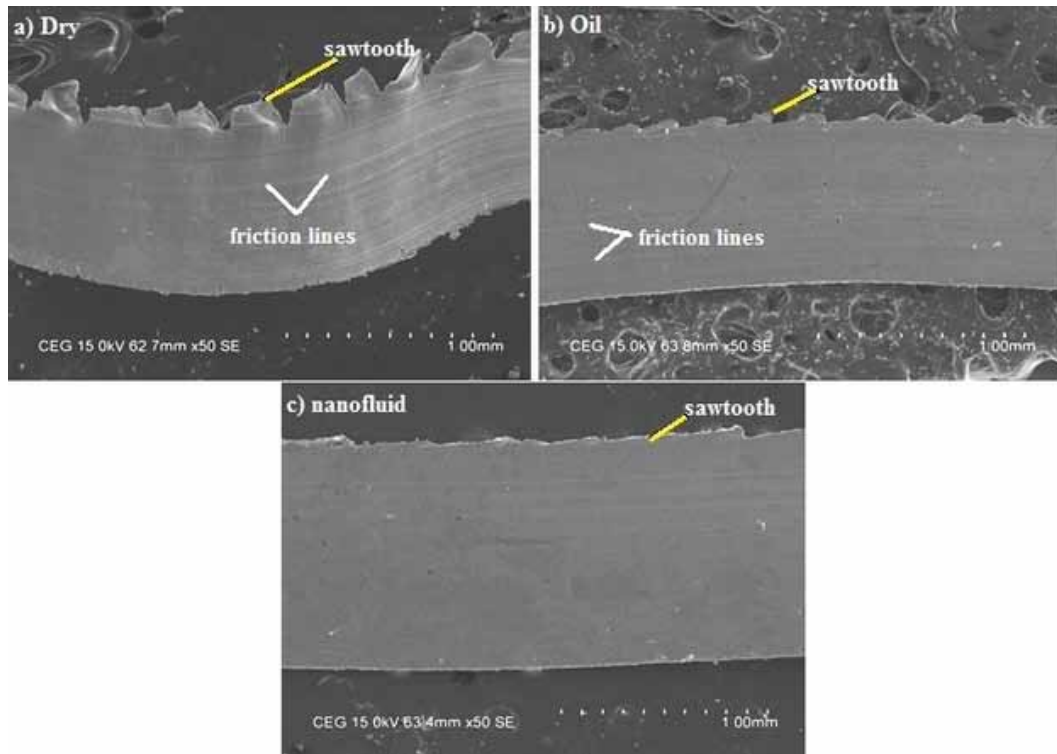
The important factors responsible for creation of saw-tooth during machining are shear localization and plastic deformation. With dry environment for initial trial ( $f2V_c^2$ ), due to nonexistence of lubrication, massive raise in temperature occurs at the machining region (Khan&Maity, 2018). Also,

**Figure 8. Tool wear (a) Dry (b) oil (c) nanofluid**

high compressive stresses were induced resulting in formation of large saw-tooth (Naresh Babu et al. 2019) as shown in Figure 9a. Further, high abrasion lines were formed (Figure 9a) signifying high friction in dry condition (Rahman et al. 2018; Chetan et al. 2016). Turning with oil environment for initial trial ( $f2V_2$ ) disclose that oil with MQL deliver lubrication at huge pressure with huge velocity, hence it enters successfully which forms a base in minimizing the abrasion induced, therefore a decrease in machining temperature was noticed (Sahu et al. 2015). Further, oil with MQL develops a thin boundary at the chip-tool interface (Ganesan et al. 2018). All these factors results in reducing the saw-tooth formed and less friction lines (Chetan et al. 2016) compared to dry environment as indicated in Figure 9b. Turning with optimal trials ( $f2A3V_3$ ) under nanofluids, reveals high thermal conductivity of silver (Chetan et al. 2016; Fang et al. 2013) which removes the heat generated, hence formation of chips developed were decreased resulting in small saw-tooth (Kumar et al. 2019) as shown in Figure 9c. Also, silver nanoparticles acts as ball bearings converting sliding motion to rolling motion, hence the formation of friction lines were reduced (Chetan et al. 2016) as shown in Figure 9c.

## RESULTS OF FACTORS ON SURFACE ROUGHNESS AND TEMPERATURE

The results of surface roughness and temperature on environmental conditions like surface roughness and temperature were shown in Figure 10. With dry machining, high friction was induced at tool-work material interface which pave way with high surface roughness (Ganesan et al. 2018). Thus a surface roughness value of  $4.01\mu m$  was obtained as shown in Figure 10. With oil under MQL, the abrasion at the machining region was decreased as oil affords better lubrication eliminating the heat developed

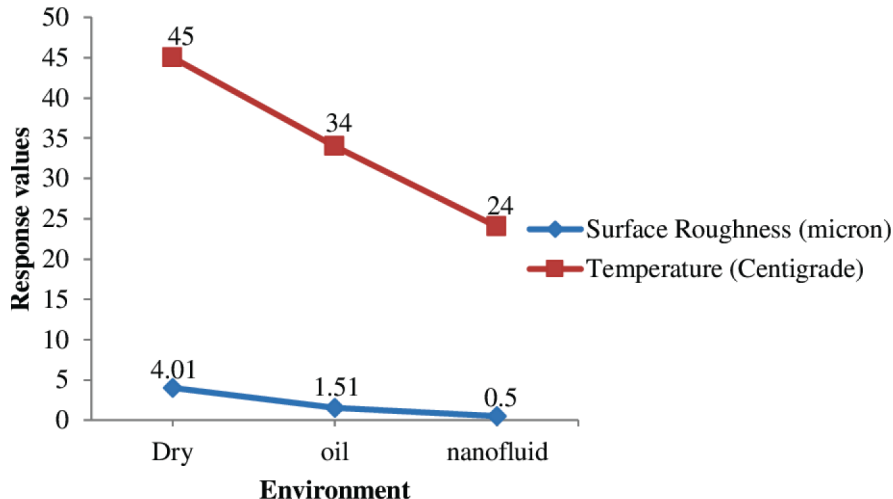
**Figure 9. Chip morphology (a) Dry (b) oil (c) nanofluid**

(Rahim & Sasahara, 2011). The surface roughness obtained was  $1.51\mu\text{m}$  as shown in Figure 10. Machining with nanofluids improves the rate of heat transfer (Huang, Wu, & Chen, 2016). Further, silver as nanoparticles exhibit high thermal conductivity (Chetan et al 2016; Fang et al 2013) hence, a reduction in surface roughness of  $0.5\mu\text{m}$  was achieved as shown in Figure 10.

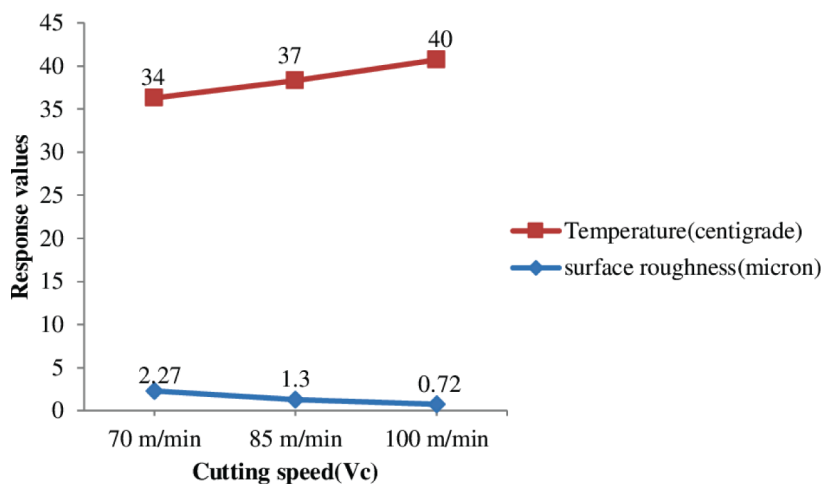
ANOVA (Table 8) indicates the contribution of factors like feed rate (0%) and cutting speed (1%) has negligible contribution. Hence, feed rate was not discussed in this section and the influence of cutting speed was reflected. Surface roughness decreases with increase in cutting speed (Sartori, Ghiotti, & Bruschi 2017; Khettabi et al. 2017) as shown in Figure 11. While machining, built-up edges (BUE) were formed and when cutting speed increases a raise in temperature were detected, hence the BUE developed were eradicated resulting in minimizing the surface roughness on the machined part ( $0.72\mu\text{m}$ ) as shown in Figure 11. Also, increase in temperature was witnessed with increase in cutting speed as shown in Figure 11. With an increase in cutting speed, friction was enhanced between tool-work material boundaries; hence an increase in temperature was noted (Sohrabpoor, Khanghah, & Teimouri, 2014).

## VALIDATION CHECK

Table 9 shows the initial factor settings ( $f2A1V_2$ ) in test order 11 which retains low SAW grade value of 0.2608 was provided with rank 18 as shown in Table 7, which produce  $4.49\mu\text{m}$  as surface roughness and  $147^\circ\text{C}$  as cutting temperature. Optimal trial was recognized as  $f2A3V_3$  in test order 18 (Table 7), hence turning with this trial generates  $0.24\mu\text{m}$  as surface roughness and  $26^\circ\text{C}$  as cutting temperature. Thus, surface roughness was decreased by 95% and temperature by 82% with optimal trial as indicated in Table 9.

**Figure 10. Effect of environment on responses**

## CONCLUSION

**Figure 11. Effect of cutting speed on responses****Table 9. Comparison on initial with optimal settings**

Factor settings	Combination Trials	Responses	
		Surface Roughness ( $\mu\text{m}$ )	Temperature ( $^{\circ}\text{C}$ )
Initial trial	f2A1V <sub>c</sub> 2	4.49	147
Optimal trial	f2A3V <sub>c</sub> 3	0.24	26
(%) of improvement with optimal trial	f2A3V <sub>c</sub> 3	95	82

The following were the conclusions attained experimentally and statistically in turning SKD 11 steel under dry, oil with MQL and silver nanofluids with MQL on surface roughness, machining temperature, tool wear and chip morphology summarized were given below.

The following were the conclusions attained experimentally and statistically in turning SKD 11 steel under dry, oil with MQL and silver nanofluids with MQL on surface roughness, machining temperature, tool wear and chip morphology summarized were given below:

- ANOVA indicates that the environment under silver nanofluids play a significant part in reducing the surface roughness, machining temperature, tool wear and formation of saw-tooth in chips.
- Comparing dry and oil environment with MQL, silver nanofluids with MQL exhibit good performance in terms of surface roughness, machining temperature, tool wear and chip morphology.
- Simple additive weighting method ensures optimal trial for minimizing surface roughness, tool wear, chip morphology and cutting temperature. The optimal combination includes cutting condition nanofluids; feed rate 0.4 mm/rev and cutting speed 100 m/min.
- The surface roughness obtained with initial trials under dry environment and with oil environment was found to be 4.49  $\mu\text{m}$  and 1.50  $\mu\text{m}$ . With optimal trials under silver nanofluid was found to be 0.24  $\mu\text{m}$ . Thus, the surface roughness was decreased by 95% with optimal trial under nanofluids compared to dry environment with initial trial.
- Machining temperature was found to be 147 °C and 34 °C under initial trials with dry and oil environment respectively, while with optimal trials under nanofluids it was observed as 26 °C. Nearly 76% and 82% reduction in temperature was attained with nanofluids compared to oil and dry environment.
- With absence of lubrication, high friction was developed resulting in producing poor quality on the machined component. With silver as nanofluids, the sliding friction was converted to rolling friction; hence a smooth profile was obtained causing a decrease in surface roughness on the work material.
- It was noticed that dry environment generates excess abrasion at the machining zone which eventually give rise to temperature. High heat transfer ability of nanoparticles minimize the heat at the machining zone, hence the temperature is decreased.
- Excess friction lines and large saw-tooth were noticed in dry environment due to high friction at the machining areas. With nanofluids, the development of frictions lines and saw-tooth formed were reduced due to efficient lubrication at chip-tool interface.
- Silver as nanofluids comprehensively reduce the tool wear on the flank face as nanoparticles, forms a small defensive layer at the machining zone which cannot be achieved in dry environment as initial trial.

Thus it shows that silver as nanofluids can be effectively used in turning SKD 11 steel due to outstanding machining performance and assists to be a lubricant in the areas of cutting fluids.

## **ACKNOWLEDGMENT**

The authors like to thank Anna University, Chennai – India, for providing testing facilities to carry out the research work. This research received no specific grant from any funding agency in the public, commercial, or not-for-profit sectors.

## REFERENCES

- Abbas, A. T., Gupta, M. K., Soliman, M. S., Mia, M., Hegab, H., Luqman, M., & Pimenov, D. Y. (2019). Sustainability assessment associated with surface roughness and power consumption characteristics in nanofluid MQL-assisted turning of AISI 1045 steel. *International Journal of Advanced Manufacturing Technology*, 105(1-4), 1311–1327. doi:10.1007/s00170-019-04325-6
- Ajay Vardhaman, B. S., Amarnath, M., Jhodkar, D., Ramkumar, J., Chelladurai, H., & Roy, M. K. (2018). Influence of coconut oil on tribological behavior of carbide cutting tool insert during turning operation. *Journal of the Brazilian Society of Mechanical Sciences and Engineering*, 40(9), 450. Advance online publication. doi:10.1007/s40430-018-1379-y
- Amini, S., Khakbaz, H., & Barani, A. (2015). Improvement of Near-Dry Machining and Its Effect on Tool Wear in Turning of AISI 4142. *Materials and Manufacturing Processes*, 30(2), 241–247. doi:10.1080/10426914.2014.952029
- Amrita, M., Srikanth, R. R., Sitaramaraju, A. V., Prasad, M. M. S., & Krishna, P. V. (2013). Experimental investigations on influence of mist cooling using nanofluids on machining parameters in turning AISI 1040 steel. *Proceedings of the Institution of Mechanical Engineers. Part J, Journal of Engineering Tribology*, 227(12), 1334–1346. doi:10.1177/1350650113491934
- Babu, M. N., Anandan, V., Muthukrishnan, N., & Gajendiran, M. (2018). Experimental process to evaluate the minimum quantity lubrication technique using copper nanofluids in turning process. *International Journal of Machining and Machinability of Materials*, 20(6), 497–512. doi:10.1504/IJMMM.2018.096377
- Bai, X., Li, C., Dong, L., & Yin, Q. (2019). Experimental evaluation of the lubrication performances of different nanofluids for minimum quantity lubrication (MQL) in milling Ti-6Al-4V. *International Journal of Advanced Manufacturing Technology*, 101(9-12), 2621–2632. doi:10.1007/s00170-018-3100-9
- Behera, B. C., Ghosh, S., & Rao, P. V. (2016). Application of nanofluids during minimum quantity lubrication: A case study in turning process. *Tribology International*, 101, 234–246.
- Churchman, C. W., Ackoff, R. J., & Amoff, E. L. (1957). *Introduction to Operation Research*. Wiley.
- Das, A., Das, S. R., Patel, S. K., & Biswal, B. B. (2019). Effect of MQL and nanofluid on the machinability aspects of hardened alloy steel. *Machining Science and Technology*, 1–30. doi:10.1080/10910344.2019.1669167
- Das, A., Patel, S. K., Biswal, B. B., Sahoo, N., & Pradhan, A. (2020). Performance Evaluation of Various Cutting Fluids Using MQL Technique in Hard Turning of AISI 4340 Alloy Steel. *Measurement*, 150, 107079. Advance online publication. doi:10.1016/j.measurement.2019.107079
- Fang, X., Ding, Q., Fan, L. W., Yu, Z. T., Xu, X., Cheng, G. H., & Cen, K. F. (2013). Thermal Conductivity Enhancement of Ethylene Glycol-Based Suspensions in the Presence of Silver Nanoparticles of Various Shapes. *Journal of Heat Transfer*, 136(3), 034501. doi:10.1115/1.4025663
- Gajrani, K. K., Suvin, P. S., Kailas, S. V., & Sankar, M. R. (2019). Hard machining performance of indigenously developed green cutting fluid using flood cooling and minimum quantity cutting fluid. *Journal of Cleaner Production*, 206(1), 108–123. doi:10.1016/j.jclepro.2018.09.178
- Ganesan, K., Naresh Babu, M., Santhanakumar, M., & Muthukrishnan, N. (2018). Experimental investigation of copper nanofluid based minimum quantity lubrication in turning of H 11 steel. *Journal of the Brazilian Society of Mechanical Sciences and Engineering*, 40(160), 160. doi:10.1007/s40430-018-1093-9
- Hegab, H., Kishawy, H. A., Gadallah, M. H., Umer, U., & Deiab, I. (2018). On machining of Ti-6Al-4V using multi-walled carbon nanotubes-based nano-fluid under minimum quantity lubrication. *International Journal of Advanced Manufacturing Technology*, 97(5-8), 1593–1603. doi:10.1007/s00170-018-2028-4
- Huang, S., Lv, T., Wang, M., & Xu, X. (2017). Enhanced machining performance and lubrication mechanism of electrostatic minimum quantity lubrication-EMQL milling process. *International Journal of Advanced Manufacturing Technology*, 94(1-4), 655–666. doi:10.1007/s00170-017-0935-4
- Huang, W. T., Wu, D. H., & Chen, J. T. (2016). Robust design of using nanofluid/MQL in micro-drilling. *International Journal of Advanced Manufacturing Technology*, 85(9-12), 2155–2161. doi:10.1007/s00170-015-7382-x

**International Journal of Manufacturing, Materials, and Mechanical Engineering**

Volume 11 • Issue 3 • July-September 2021

- Jia, D., Li, C., Zhang, Y., Yang, M., Wang, Y., Guo, S., & Cao, H. (2017). Specific energy and surface roughness of minimum quantity lubrication grinding Ni-based alloy with mixed vegetable oil-based nanofluids. *Precision Engineering*, 50, 248–262. doi:10.1016/j.precisioneng.2017.05.012
- Khajehzadeh, M., Moradpour, J., & Razfar, M. R. (2018). Influence of nanofluids application on contact length during hard turning. *Materials and Manufacturing Processes*, 34(1), 30–38. doi:10.1080/10426914.2018.1532091
- Khan, A., & Maity, K. (2018). Influence of cutting speed and cooling method on the machinability of commercially pure titanium (CP-Ti) grade II. *Journal of Manufacturing Processes*, 31, 650–661. doi:10.1016/j.jmapro.2017.12.021
- Khan, M. M. A., Mithu, M. A. H., & Dhar, N. R. (2009). Effects of minimum quantity lubrication on turning AISI 9310 alloy steel using vegetable oil-based cutting fluid. *Journal of Materials Processing Technology*, 209(15–16), 5573–5583. doi:10.1016/j.jmatprotec.2009.05.014
- Khandekar, S., Ravi Sankar, M., Agnihotri, V., & Ramkumar, J. (2012). Nano-cutting fluid for enhancement of metal cutting performance. *Materials and Manufacturing Processes*, 27(9), 963–967. doi:10.1080/10426914.2011.610078
- Khettabi, R., Nouioua, M., Djebara, A., & Songmene, V. (2017). Effect of MQL and dry processes on the particle emission and part quality during milling of aluminum alloys. *International Journal of Advanced Manufacturing Technology*, 92(5–8), 2593–2598. doi:10.1007/s00170-017-0339-5
- Krishnaiah, K., & Shahabudeen, P. (2012). *Applied design of experiments and taguchi methods* (1st ed.). PHI Learning Pvt Ltd.
- Kumar, R., Sahoo, A. K., Mishra, P. C., & Das, R. K. (2019). Influence of  $\text{Al}_2\text{O}_3$  and  $\text{TiO}_2$  nanofluid on hard turning performance. *International Journal of Advanced Manufacturing Technology*. Advance online publication. doi:10.1007/s00170-019-04754-3
- Kumar Sharma, A., Kumar Tiwari, A., Rai Dixit, A., & Kumar Singh, R. (2020). Measurement of Machining Forces and Surface Roughness in Turning of AISI 304 steel using Alumina-MWCNT Hybrid Nanoparticles Enriched Cutting Fluid. *Measurement*, 150, 107078. Advance online publication. doi:10.1016/j.measurement.2019.107078
- Lawal, S. A., Choudhury, I. A., & Nukman, Y. (2013). A case for minimum quantity lubrication using vegetable oil-based lubricant. *Journal of Cleaner Production*, 41, 210–221. doi:10.1016/j.jclepro.2012.10.016
- Li, M., Yu, T., Yang, L., Li, H., Zhang, R., & Wang, W. (2018). Parameter optimization during minimum quantity lubrication milling of  $\text{TC}_4$  alloy with graphene-dispersed vegetable-oil-based cutting fluid. *Journal of Cleaner Production*. Advance online publication. doi:10.1016/j.jclepro.2018.11.147
- Lv, T., Huang, S., Liu, E., Ma, Y., & Xu, X. (2018). Tribological and machining characteristics of an electrostatic minimum quantity lubrication (EMQL) technology using graphene nano-lubricants as cutting fluids. *Journal of Manufacturing Processes*, 34, 225–237. doi:10.1016/j.jmapro.2018.06.016
- Minh, D. T., The, L. T., & Bao, N. T. (2017). Performance of  $\text{Al}_2\text{O}_3$  nanofluids in minimum quantity lubrication in hard milling of  $60\text{Si}_2\text{Mn}$  steel using cemented carbide tools. *Advances in Mechanical Engineering*, 9(7). Advance online publication. doi:10.1177/1687814017710618
- Nam, J., & Lee, S. W. (2018). Machinability of titanium alloy (Ti-6Al-4V) in environmentally-friendly micro-drilling process with nanofluid minimum quantity lubrication using nanodiamond particles. *International Journal of Precision Engineering and Manufacturing-Green Technology*, 5(1), 29–35. doi:10.1007/s40684-018-0003-z
- Nandakumar, A., Rajmohan, T., & Vijayabhaskar, S. (2019). *Experimental Evaluation of the Lubrication Performance in MQL Grinding of Nano SiC Reinforced Al Matrix Composites*. Silicon. doi:10.1007/s12633-019-0088-1
- Naresh Babu, M., Anandan, V., Muthukrishnan, N., Arivalagar, A. A., & Dinesh Babu, M. (2019). Evaluation of Graphene based nanofluids with minimum quantity lubrication in turning of AISI D3 steel. *SN Applied Sciences*, 1(10), 1202. doi:10.1007/s42452-019-1182-0
- Padmini, R., Vamsi Krishna, P., & Krishna Mohana Rao, G. (2016). Effectiveness of vegetable oil based nanofluids as potential cutting fluids in turning AISI 1040 steel. *Tribology International*, 94, 490–501. doi:10.1016/j.triboint.2015.10.006

- Rahim, E. A., & Sasahara, H. (2011). Investigation of Tool Wear and Surface Integrity on MQL Machining of Ti-6AL-4 V Using Biodegradable Oil. *Proceedings of the Institution of Mechanical Engineers. Part B, Journal of Engineering Manufacture*, 225(9), 1505–1511. doi:10.1177/0954405411402554
- Rahman, S. S., Ashraf, M. Z. I., Amin, A. N., Bashar, M. S., Ashik, M. F. K., & Kamruzzaman, M. (2018). Tuning nanofluids for improved lubrication performance in turning biomedical grade titanium alloy. *Journal of Cleaner Production*. Advance online publication. doi:10.1016/j.jclepro.2018.09.150
- Raju, R. K., Andhare, A., & Sahu, N. K. (2017). Performance of multiwalled carbon nanotube-based nanofluid in turning operation. *Materials and Manufacturing Processes*, 32(13), 1490–1496. doi:10.1080/10426914.2017.1279291
- Rosnan, R., Murad, M. N., Azmi, A. I., & Shyha, I. (2019). Effects of minimal quantity lubricants reinforced with nano-particles on the performance of carbide drills for drilling nickel-titanium alloys. *Tribology International*, 136, 58–66. Advance online publication. doi:10.1016/j.triboint.2019.03.029
- Sahu, N., Andhare, A. B., & Raju, R. A. (2018). Evaluation of performance of nanofluid using multiwalled carbon nanotubes for machining of Ti-6AL-4V. *Machining Science and Technology*, 22(3), 476–492. doi:10.1080/10910344.2017.1365898
- Sahu, S. K., Mishra, P. C., Orra, K., & Sahoo, A. K. (2015). Performance assessment in hard turning of AISI 1015 steel under spray impingement cooling and dry environment. *Proceedings of the Institution of Mechanical Engineers. Part B, Journal of Engineering Manufacture*, 229(2), 251–265. doi:10.1177/0954405414528165
- Saravanakumar, N., Prabu, L., Karthik, M., & Rajamanickam, A. (2014). Experimental analysis on cutting fluid dispersed with silver nano particles. *Journal of Mechanical Science and Technology*, 28(2), 645–651. doi:10.1007/s12206-013-1192-6
- Sarhan, A. A. D., Sayuti, M., & Hamdi, M. (2012). Reduction of power and lubricant oil consumption in milling process using a new SiO<sub>2</sub> nano lubrication system. *International Journal of Advanced Manufacturing Technology*, 63(5-8), 505–512. doi:10.1007/s00170-012-3940-7
- Sarikaya, M., Yilmaz, V., & Gullu, A. (2016). Analysis of cutting parameters and cooling/lubrication methods for sustainable machining in turning of Haynes 25 superalloy. *Journal of Cleaner Production*, 133, 172–181. doi:10.1016/j.jclepro.2016.05.122
- Sartori, S., Ghiotti, A., & Bruschi, S. (2017). Hybrid lubricating/cooling strategies to reduce the tool wear in finishing turning of difficult to- cut alloys. *Wear*, 376–377, 107–114. doi:10.1016/j.wear.2016.12.047
- Shakouri, G. H., Nabae, M., & Aliakbarisani, S. (2014). A quantitative discussion on the assessment of power supply technologies: DEA (data envelopment analysis) and SAW (simple additive weighting) as complementary methods for the “Grammar.”. *Energy*, 64, 640–647. doi:10.1016/j.energy.2013.10.022
- Sharma, A. K., Katiyar, J. K., Bhaumik, S., & Roy, S. (2019). Influence of alumina/MWCNT hybrid nanoparticle additives on tribological properties of lubricants in turning operations. *Friction*, 7(2), 153–168. doi:10.1007/s40544-018-0199-5
- Sharma, A. K., Singh, R. K., Dixit, A. R., & Tiwari, A. K. (2016). Characterization and experimental investigation of Al<sub>2</sub>O<sub>3</sub> nanoparticle based cutting fluid in turning of AISI 1040 steel under minimum quantity lubrication (MQL). *Materials Today: Proceedings*, 3(6), 1899–1906. doi:10.1016/j.matpr.2016.04.090
- Singh, H., Sharma, V. S., & Dogra, M. (2020). Exploration of graphene assisted vegetables oil based minimum quantity lubrication for surface grinding of TI-6AL-4V-ELI. *Tribology International*, 144, 106113. Advance online publication. doi:10.1016/j.triboint.2019.106113
- Singh, H., Sharma, V. S., Singh, S., & Dogra, M. (2019a). Nanofluids assisted environmental friendly lubricating strategies for the surface grinding of titanium alloy: Ti6Al4V-ELI. *Journal of Manufacturing Processes*, 39, 241–249. doi:10.1016/j.jmapro.2019.02.004
- Singh, R., Dureja, J. S., & Dogra, M. (2019b). Performance evaluation of textured carbide tools under environment-friendly minimum quantity lubrication turning strategies. *Journal of the Brazilian Society of Mechanical Sciences and Engineering*, 41(2), 87. doi:10.1007/s40430-019-1586-1

**International Journal of Manufacturing, Materials, and Mechanical Engineering**  
Volume 11 • Issue 3 • July-September 2021

Sirin, S., & Kivak, T. (2019). Performances of different eco-friendly nanofluid lubricants in the milling of Inconel X-750 superalloy. *Tribology International*, 137, 180–192. Advance online publication. doi:10.1016/j.triboint.2019.04.042

Sohrabpoor, H., Khanghah, S. P., & Teimouri, R. (2014). Investigation of lubricant condition and machining parameters while turning of AISI 4340. *International Journal of Advanced Manufacturing Technology*, 76(9-12), 2099–2116. doi:10.1007/s00170-014-6395-1

Suneesh, E., & Sivapragash, M. (2019). Parameter optimisation to combine low energy consumption with high surface integrity in turning Mg/Al<sub>2</sub>O<sub>3</sub> hybrid composites under dry and MQL conditions. *Journal of the Brazilian Society of Mechanical Sciences and Engineering*, 41(2), 89. doi:10.1007/s40430-019-1587-0

Thakur, A., Manna, A., & Samir, S. (2019). *Multi-Response Optimization of Turning Parameters during Machining of EN-24 Steel with SiC Nanofluids Based Minimum Quantity Lubrication*. *Silicon*. doi:10.1007/s12633-019-00102-y

Unal, O., & Maleki, E. (2018). Shot peening optimization with complex decision-making tool: Multi criteria decision-making. *Measurement*, 125, 133–142. doi:10.1016/j.measurement.2018.04.077

Wang, Y., Li, C., Zhang, Y., Yang, M., Zhang, X., Zhang, N., & Dai, J. (2016). Experimental evaluation on tribological performance of the wheel/workpiece interface in minimum quantity lubrication grinding with different concentrations of Al<sub>2</sub>O<sub>3</sub> nanofluids. *Journal of Cleaner Production*. Advance online publication. doi:10.1016/j.jclepro.2016.10.110

Yildirim, C. V., Kivak, T., & Erzincanli, F. (2019a). Influence of Different Cooling Methods on Tool Life, Wear Mechanisms and Surface Roughness in the Milling of Nickel-Based Waspaloy with WC Tools. *Arabian Journal for Science and Engineering*, 44(9), 7979–7995. Advance online publication. doi:10.1007/s13369-019-03963-y

Yildirim, C. V., Sarikaya, M., Kivak, T., & Sirin, S. (2019b). The effect of addition of hBN nanoparticles to nanofluid-MQL on tool wear patterns, tool life, roughness and temperature in turning of Ni-based Inconel 625. *Tribology International*, 134, 443–456. Advance online publication. doi:10.1016/j.triboint.2019.02.027

## APPENDIX: NOMENCLATURE

SAW: Simple additive weighting method

AISI: American Iron and Steel Institute

MQL: Minimum Quantity Lubrication

f: Feed rate (mm/rev)

V<sub>c</sub>: Cutting speed (m/min)

SEM: Scanning Electron Microscope

R<sub>a</sub>: Average surface roughness (micron)

Nm: nanometer

µm: Microns

SDBS: Sodium dodecylbenzenesulfonate

CNC: Computer numerical control

ANOVA: Analysis of variance

BUE: Built up edges

W/mK: Watt per metre kelvin

MoS<sub>2</sub>: Molybdenum disulfide

SiO<sub>2</sub>: Silicon Dioxide

Al<sub>2</sub>O<sub>3</sub>: Aluminium oxide

TiO<sub>2</sub>: Titanium dioxide

CNT: Carbon nanotubes

SiC: Silicon carbide

*M. Naresh Babu obtained B.E. in Mechanical Engineering and received his MTech in Production Engineering from the MS University, Tirunelveli in 2002. He received his PhD in Mechanical Engineering from the Anna University Chennai, India in 2015. He has 16 years of experience in teaching. His research interests include unconventional machining process, optimisation and minimum quantity lubrication using nanofluids.*

*V. Anandan is working with Saveetha Engineering College in the Department of Mathematics since 2009. He received his MSc in Mathematics from the University of Madras, MPhil in Mathematics from the Alagappa University PhD at the Bharathiar University. He has 12 years of experience in teaching. His research interests include multi-criteria decision making, optimisation and fuzzy set theory.*

*M. Dinesh Babu is working with Panimalar Engineering College, Chennai. He received his PhD from the Anna University in 2017. He is doing research in the fields of nanofluid heat transfer and energy storage. His research interests include nanofluid lubrication, machining, and fuel additives. He has 15 years of teaching experience.*

*N. Muthukrishnan is currently working as a Professor in the Department of Mechanical Engineering, Sri Venkateswara College of Engineering, Irungattukottai. In 1986, he received his BE in Production Engineering, Anna University, Chennai. In 1993, he completed his MS in Technological Operations from the BITS, Pilani, Rajasthan. He received his PhD in Mechanical Engineering from the JNT University, Hyderabad in 2009. He is acting as a reviewer for Elsevier, Springer, InderScience, Taylor and Francis publications journals, etc.*

# International Journal of Manufacturing, Materials, and Mechanical Engineering

Volume 11 • Issue 3 • July-September 2021 • ISSN: 2156-1680 • eISSN: 2156-1672

## MISSION

The mission of the **International Journal of Manufacturing, Materials, and Mechanical Engineering (IJMMME)** is to provide a channel of communication to disseminate knowledge between academics/researchers and industry practitioners. This journal can serve as a useful reference for academics, manufacturing, materials, mechanical, industrial, systems, environmental and physics engineers, materials and manufacturing researches, professionals in mechanical engineering and related industries.

## SUBSCRIPTION INFORMATION

The International Journal of Manufacturing, Materials, and Mechanical Engineering (IJMMME) is available in print and electronic formats and offers individual or institution-level pricing. Full subscription information can be found at [www.igi-global.com/IJMMME](http://www.igi-global.com/IJMMME).

IJMMME is also included in IGI Global's InfoSci-Journals Database which contains all of IGI Global's peer-reviewed journals and offers unlimited simultaneous access, full-text PDF and XML viewing, with no DRM. Subscriptions to the InfoSci-Journals Database are available for institutions. For more information, please visit [www.igi-global.com/infosci-journals](http://www.igi-global.com/infosci-journals) or contact E-Resources at [eresources@igi-global.com](mailto:eresources@igi-global.com).

## CORRESPONDENCE AND QUESTIONS

### EDITORIAL

J. Paulo Davim, Editor-in-Chief • [IJMMME@igi-global.com](mailto:IJMMME@igi-global.com)

### SUBSCRIBER INFO

#### IGI Global • Customer Service

701 East Chocolate Avenue • Hershey PA 17033-1240, USA

**Telephone:** 717/533-8845 x100 • **E-Mail:** [cust@igi-global.com](mailto:cust@igi-global.com)

The *International Journal of Manufacturing, Materials, and Mechanical Engineering* is indexed or listed in the following. ACM Digital Library; Bacon's Media Directory; Cabell's Directories; DBLP; Google Scholar; INSPEC; JournalTOCs; MediaFinder; ProQuest Engineering Journals; ProQuest Illustrata: Technology; ProQuest Materials Science Journals; ProQuest SciTech Journals; ProQuest Technology Journals; SCOPUS; The Standard Periodical Directory; UGC-CARE List (India); Ulrich's Periodicals Directory; Web of Science; Web of Science Emerging Sources Citation Index (ESCI)